National University of Science and Technology POLITEHNICA Bucharest

Doctoral School of Mechanical Engineering and Mechatronics

PhD THESIS

Extended Abstract

EXPERIMENTAL AND NUMERICAL STUDY ON THE BALLISTIC BEHAVIOR OF HYBRID PANELS FOR INDIVIDUAL PROTECTION

PhD Candidate

Eng. Christian POPESCU

PhD Supervisor

Prof. habil. eng. Petre Lucian SEICIU, PhD

Bucharest

2026

Blank page

Acknowledgement

I express my gratitude to all the individuals who supported and guided me throughout the preparation of this doctoral thesis.

I would like to thank professor habil. PhD eng. Petre Lucian Seiciu, the scientific supervisor of this thesis, for his professional guidance and for the encouragement he provided throughout the doctoral training period and the development of this work.

I am deeply grateful to professor PhD eng. Lorena Deleanu for her support, in her capacity as a member of the supervisory committee, for her pertinent critical remarks and for the solutions identified during the preparation of the reports and the thesis, as well as for the rigorous and professional guidance she provided.

I would also like to thank the members of the supervisory committee — PhD physicist Simona Maria Sandu, associate professor PhD eng. Alexandru Nicolae Stoica, and associate professor PhD eng. Georgiana Ionela Păduraru — for their constant support and involvement in the thesis preparation process.

The experimental trials were carried out together with PhD physicist Simona Sandu, with the support of the staff of CBRN Defense and Ecology Research and Innovation Center, Bucharest, within the Individual Ballistic Protection Equipment Laboratory.

I would like to express my thanks to PhD eng. Cătălin Pîrvu, from the National Institute for Aerospace Research and Development "Elie Carafoli" – INCAS, for the recommendations provided in the development of the model, as well as to PhD eng. George Ghiocel Ojoc, Autonomous Flight Technologies, for his usage recommendations and for the technical assistance provided in the use of ANSYS Explicit Dynamics software.

For the SEM images obtained using the electron microscope at "Dunărea de Jos" University of Galați, carefully selected, analyzed, and utilized in support of the investigations into failure mechanisms, I would like to express my gratitude to associate professor PhD physicist Alina Cantaragiu Cioromila..

With heartfelt gratitude, I thank my wife and parents for their unwavering support and for standing by me throughout this period..

Eng. Christian Popescu

Summary

CHAPTER 1

THE FIELD OF BALLISTIC PROTECTION

1.1. Overview of personal ballistic protection

The main objective of research in the field of individual ballistic protection equipment is the development of an efficient protective clothing system that is easy to wear, lightweight, and affordable, while providing effective resistance to ballistic impacts. The performance of these textile-based protective systems is influenced by a number of essential factors, such as yarn type and composition, fabric density and structure, angle of impact, projectile shape, and impact velocity. All these parameters affect the material's ability to absorb and dissipate the energy generated during a ballistic impact [31].

The development of body protection systems seeks to achieve a balance between ballistic protection, low weight, flexibility, and comfort through the optimization of materials, panel design, and finishing processes [4], [6], [7], [26], [56], [67], [86], [89]. Two-dimensional (2D) fabrics and unidirectional laminates are frequently used due to their low weight and good impact resistance [2], [40], while hybrid solutions, interlayer bonding, and surface modifications can enhance impact energy absorption [25], [61], [65]. In parallel, three-dimensional (3D) fabrics are emerging as a promising direction due to their improved ballistic performance [5], [17], [30].

Among the high-performance fibers widely used in individual ballistic protection systems are:

- aramid fibers, represented by the commercial brands Twaron® (registered trademark of Teijin Aramid) [99], [100] and Kevlar® (registered trademark of DuPont) [108];
- ultra-high-molecular-weight polyethylene (UHMWPE) fibers, represented by the brands Dyneema® (registered trademark of DSM Protective Materials, currently part of Avient Corporation) [103] and Spectra® (registered trademark of Honeywell) [104].

These fibers have been extensively used due to their favorable protective properties and the requirements of operational personnel, including high strength and toughness, low weight, and good chemical resistance [4].

1.2. Categories of individual ballistic protection systems

1.2.1. Introduction

The increasing demands of end users for individual protection systems have led to significant improvements in both materials and design. A wide range of ballistic vest options is now available on the market, offering different levels of protection against various threats.

Regardless of their design (Fig. 1.1b and c), all protection systems typically consist of three components (Fig. 1.1a): the outer carrier, flexible ballistic panels, and hard ballistic plates.

- The outer carrier of a ballistic vest is generally made from high-strength synthetic materials such as Cordura® [115], nylon, or polyester, specifically selected for durability, abrasion resistance, and moisture protection;
- Ballistic panels are composed of multiple superimposed layers of materials specially engineered to withstand projectile impacts and other ballistic threats;

The protective cover of the ballistic panels serves to shield the ballistic materials from environmental factors such as moisture, dust, and abrasion (friction in wet conditions).

a) b) c)

Fig. 1.1. (a) Composition of the individual protection system, (b) concealable vest, (c) tactical vest [2], [122]

1.2.2. Hard body armor system

The hard armor protection system, developed in response to the limitations of flexible textile-based protection against military ammunition, has become the standard in military and security applications where bullet velocities exceed 500 m/s. It integrates soft textile-based armor with rigid materials such as metal plates (steel or titanium alloys), ceramic plates made of alumina, silicon carbide, or boron carbide, ultra-high-molecular-weight polyethylene plates, or laminated composites. This type of protection system is worn in high-risk situations. Individual plates may weigh between 1 kg and 4 kg [31].

Ballistic plates stop projectiles by dissipating kinetic energy, primarily through the controlled fracture of the hard ceramic layer, a mechanism distinct from the plastic deformation typical of metallic or flexible armor. Ceramic alone is insufficient; therefore, modern plates combine monolithic ceramics (or ceramic composites) with high-performance textile backings, achieving high hardness, compressive strength, and low weight. This combination promotes projectile fragmentation and distributes the impact load over a larger surface area, reducing backface deformation (BFD) [31], [32], [96].

According to Medvedovski [54], ceramics absorb energy through micro- and macro-cracking, whereas metallic or textile armors dissipate energy through plastic deformation and fiber stretching [82]; the differences between these mechanisms are fundamental to the design of hybrid systems [31], [53].

While conventional systems employed ceramic plates supported by aramid fiber or UHMWPE panels, recent trends promote fully polymeric or composite plates with thermoplastic matrices reinforced with UHMWPE or aramid fibers. These solutions provide lower weight, improved multi-hit performance, and greater durability under mechanical and environmental loading [72].

1.2.3. Soft body armor system

The soft armor protection system is a type of flexible and lightweight protection made from adaptable fibrous materials [66]. It is distinguished by its low weight, enhanced wearer mobility, and improved resistance to bullets [46], [74]. It can be used independently or in combination with a hard armor protection system, depending on the level of threat. Due to the flexibility and comfort it provides, it is ideal for ballistic equipment intended for the military, law enforcement, and security personnel [96], particularly in low-risk situations [54], [96].

Soft armor systems are typically constructed from 20–50 layers of lightweight ballistic textiles, providing effective protection against low- and medium-intensity threats, especially handgun ammunition, while maintaining a high level of comfort. Unidirectional or multidirectional textile structures are commonly used, including 2D and, more recently, 3D configurations. Fabric type and multilayer architecture directly influence impact performance and penetration behavior [2].

Soft armor systems limit transverse deformation and distribute impact energy over an extended area, thereby increasing protection efficiency. Upon impact, the projectile's kinetic energy is transformed into the kinetic energy of the fabric, yarn deformation energy, and energy dissipated through sliding friction, along with other absorption mechanisms [48]. Ballistic performance depends on the material's ability to rapidly absorb, transfer, and dissipate energy to prevent early localized failure, and is influenced by fiber properties, fabric structure, number of layers, friction, and projectile shape and trajectory [97].

Once the stopping capacity is exceeded, particularly in the front layers, localized failure mechanisms predominate, similar to shear and tensile rupture observed in metallic armors. These include fiber breakage around the impact point and the pull-out of a material plug that advances together with the projectile [34].

1.3. High-performance materials for personal protective systems

1.3.1. High-performance fibers for ballistic protection

Para-aramid fibers and their properties

Among high-strength, high-modulus fibers, para-aramids are distinguished by their exceptional thermal stability, exhibiting no melting at elevated temperatures, while showing sensitivity to UV radiation and low moisture absorption. Aramid fibers, first introduced by DuPont in the 1960s, are aromatic polyamides obtained from aromatic acids and amines, whose chemical structure promotes strong intermolecular bonding. These fibers are characterized by high tensile and compressive strength, abrasion resistance, resistance to chemical degradation, and thermal stability. In addition, they exhibit excellent dimensional stability and a very low coefficient of thermal expansion, and they regain their ballistic performance after drying [3], [31].

Another major advantage is their behavior under extreme temperatures: aramid fibers retain their mechanical properties even after prolonged exposure to thermal variations. No strength losses are observed at temperatures as low as −196 °C, and the material does not melt but begins to carbonize only at approximately 427 °C [2].

Kevlar® [108] and Twaron® [99], [100] are two of the most widely used para-aramid materials in the manufacture of individual ballistic protection systems. Both are distinguished by a strength up to five times greater than that of steel, while maintaining the flexibility and durability required to successfully withstand high-energy ballistic impacts [90], [92].

Kevlar® is the trade name of a para-aramid fiber developed in 1965 by chemist Stephanie Kwolek at DuPont. Initially used as a steel substitute in racing tires, the fiber quickly became an essential material in modern body armor [1], [39], [87]. Owing to its very high tensile strength, high modulus, and excellent toughness, Kevlar® fabrics can absorb significant amounts of impact energy and are widely used in bulletproof vests, ballistic helmets, and other protective systems [31], [50], [58], [59], [60].

Ultra-high-molecular-weight polyethylene fibers for ballistic protection

UHMWPE, known as ultra-high-molecular-weight polyethylene, is another type of high-strength, high-modulus fiber used in ballistic panels. This type of fiber is employed in a variety of body armor products. UHMWPE was first introduced in the mid-1980s by Allied-Signal—now Honeywell Advanced Fibers and Composites (Colonial Heights, VA, USA)—and DSM High Performance Fibers (Heerlen, Netherlands) [23]. UHMWPE fibers have properties comparable to those of para-aramids but belong to the polyolefin family, being composed of extremely long polyethylene chains.

By laminating unidirectional layers sealed between polyethylene films, both flexible panels and rigid plates for ballistic protection systems can be produced. UHMWPE fibers combine high modulus with good flexibility, enabling them to efficiently absorb energy under high-velocity dynamic loading. Their main limitations are a relatively low melting temperature and their non-hygroscopic nature [4], [88].

UHMWPE fibers have a relatively low melting point, approximately 144–152 °C, and their mechanical properties (toughness and modulus) tend to decrease at elevated temperatures and increase at subzero temperatures. According to manufacturer data, the strength-to-weight ratio can be up to 40% higher than that of para-aramid fibers, providing a significant advantage in the development of lightweight yet energy-efficient ballistic armor.

Among commercially available UHMWPE fibers with very high elastic modulus, Dyneema® (DSM) [103] and Spectra® (Honeywell) [104] are widely used in ballistic applications. Spectra™ fibers are reported to have a strength approximately ten times greater than steel and about 40% higher than that of aramid fibers at the same specific weight [4], [33].

1.3.2. Ballistic textile fabrics

In ballistic protection, 2D fabrics, unidirectional (UD) laminates, multiaxial structures, and 3D fabrics are frequently used [81]. Biaxial, triaxial, and even quadraxial fabrics, as well as UD laminates, are widely employed in bulletproof vests and composite applications [64];

however, woven fabrics may exhibit reduced impact performance due to yarn crimp, low delamination resistance, and poor in-plane shear behavior.

Two-dimensional (2D) fabrics are the simplest and most commonly used textile structures in ballistic applications, produced by interlacing warp and weft yarns according to a predetermined pattern. Multiple layers can be stacked or stitched in different orientations to enhance resistance to ballistic penetration and stabbing threats [13], [14]. Coating with elastomers or impregnation with shear-thickening fluids or silica nanoparticles can further improve impact performance [45]. A key parameter is the fabric cover factor; values between 0.6 and 0.95 are considered optimal for ballistic protection, while values outside this range may lead to reduced performance [23].

Three-dimensional (3D) fabrics have become a major focus in ballistic protection due to their superior impact behavior, as demonstrated through modern analysis and manufacturing methods [29]. The literature describes structures such as 3D angle-interlock (through-thickness binder yarns following an angled path), 3D orthogonal composites, 3D braids, fully or partially interlaced fabrics, and multiaxial warp-knitted composites, all showing superior performance compared to 2D structures. The distinctive feature of these materials is the presence of through-thickness (Z-direction) binder yarns that connect warp and weft layers, increasing areal density and delamination resistance. These transverse fibers significantly contribute to damage tolerance and energy absorption capacity under ballistic impact conditions [12], [29], [31].

1.4. Architecture of individual ballistic protection systems

1.4.1. Hybridization of ballistic materials in multilayer panels

Hybrid panels for ballistic protection use high-strength, low-density fibers (aramids, UHMWPE) to achieve an optimal balance between mass and impact performance. The performance of these structures depends strongly on the combination of materials and the stacking sequence of the layers. Numerical studies have shown that, for the same total thickness, the order and proportion of high-stiffness laminates and more ductile layers significantly influence the projectile stopping capability [36].

Textile architecture also plays a decisive role. Analytical and numerical models indicate that woven layers placed at the front provide better shear resistance, while unidirectional (UD) layers positioned at the rear efficiently carry tensile loads, leading to superior energy dissipation and better correlation with experimental results [81].

Research on the hybridization of nonwoven and woven UHMWPE fabrics has demonstrated that hybrid structures can outperform each individual architecture used separately, achieving higher ballistic limits and improved fragment retention [52]. Numerical simulations have confirmed the deformation mechanisms observed experimentally.

Finite element analyses have shown that front layers are dominated by shear failure, whereas rear layers fail primarily in tension; therefore, materials with high shear resistance are optimal for the front, while those with high tensile strength are better suited for the back. Hybrid configurations with UHMWPE woven fabrics on the impact face and aramid UD layers arranged at the rear have demonstrated superior ballistic performance, with an optimal fabric-to-UD ratio of approximately 1:3, enabling a reduction in the total system mass [21].

1.4.2. Layer arrangement and stacking sequence in hybrid ballistic panels

The most important parameters for improving the ballistic performance of protective panels are [38], [55], [70]: the nature and architecture of the layers, the stacking sequence, and the layer orientations.

In the design of hybrid ballistic panels, the arrangement of protective materials within the front and rear layers is essential. In a study conducted by Park et al., the lamination sequence was identified as a critical parameter in optimizing the ballistic performance of multilayer hybrid panels made of impregnated fabrics [65].

1.4.3. Hybrid body armor systems

Hybridization based on transverse deformation

Cunniff demonstrated that changing the stacking order in a hybrid panel can produce significantly different responses, although certain combinations may exhibit limited sensitivity to layer sequence in textile ballistic panels [27]. To illustrate the effect of constraining transverse deformation in fabrics, several heterogeneous systems—also classifiable as hybrid woven textile materials—were tested.

The first system, consisting of a 1000 denier Kevlar® 29 fabric layer backed by a 375 denier Spectra® fabric layer, exhibited a ballistic limit of 269 m/s. Reversing the order of the fabrics resulted in a ballistic limit of only 114 m/s. In another test conducted under the same impact parameters, a 1000 denier Kevlar® 29 layer backed by a 1040 denier Kevlar® 49 layer provided ballistic performance similar to that of the same configuration in reverse order.

In both the Kevlar® 29/Spectra® and Kevlar® 29/Kevlar® 49 experiments, the mismatch in material properties should have produced a mismatch in transverse deformation signatures: the material with the higher modulus would be expected to exhibit lower transverse deformation. Therefore, the simple two-layer experiments reported by Cunniff [27] are inconclusive, but they opened a research direction for hybrid panels, emphasizing that experimental testing is necessary to determine ballistic performance, even when the mechanical properties of each layer are known and ranked.

In hybrid Spectra®/Kevlar® systems, differences in transverse deformation lead to stress concentration in the impact zone, reducing ballistic performance [73]. The influence of layer sequence has been experimentally confirmed through testing of reversed configurations [84].

Hybridization based on shear and tensile failure mechanisms

Chen et al. showed that UHMWPE unidirectional (UD) fabrics are more prone to shear failure when impacted by sharp-edged projectiles, as the filaments are constrained by the matrix and cannot easily move to redistribute stresses. In contrast, conventional woven fabrics can dissipate loads through yarn decrimping, yarn pull-out, and the formation of “windows,” making them more suitable for front layers. Tests demonstrated that hybrid panels outperform monomaterial UD systems, with an optimal fabric-to-UD mass ratio of approximately 1:3 [22].

This ratio was also confirmed in studies involving aramid fabrics, where a configuration of ~70% UD and ~30% Twaron fabric provided the best trauma protection. However, after water immersion, 100% UD panels exhibited superior performance compared to hybrid and woven panels, suggesting greater stability of UD structures in harsh environments [42].

UHMWPE fibers are susceptible to thermal damage caused by projectile sliding within the target. This leads to premature failure and limited propagation of transverse waves. Replacing the first few front layers with flame-resistant aramid materials improves energy absorption by 27.09% [10], [94]. It has also been demonstrated that fabrics and felts reduce backface deformation during the impact process [93], [95].

1.5. State of the art in flexible panel testing

Table 1.1 presents several recent, representative studies on flexible panels for ballistic protection. The diversity of projectiles used can be observed, as well as the tendency to combine aramid fiber fabrics and UHMWPE, some of the most high-performing materials even in single-material panels. However, the results are difficult to compare due to variations in panel dimensions, ammunition types, and the parameters selected to evaluate impact behavior. Nevertheless, backface deformation (BFD) is frequently used as a key parameter for assessing the quality of protective panels.

Table 1.1. Scientific research on flexible ballistic panels

Author / year	Specimen / Material	Dimensions (mm)	Ammunition	Projectile Velocity (m/s)	Key Findings
Chang 2021 [20]	- Kevlar + STF - Kevlar + polyurea - Kevlar + polyurea + STF	130 × 130	9 mm FMJ .44 Magnum	according to NIJ 0101.06	BFD within NIJ allowable limits
Shih 2022 [83]	- Kevlar + STF - Kevlar + Epoxy resin - Kevlar + polyurea	130 × 130	9 mm FMJ .44 Magnum	412 ± 6 442 ± 18	BFD values: 34–66 mm
Ribeiro 2022 [76]	analyzes flexible ballistic panels composed of Kevlar/Twaron and UHMWPE	not reported	9 mm FMJ .357 Magnum .44 Magnum	350–450 up to 700	high effectiveness of the combinations
Mudzi 2022 [57]	Spectra 900 UHMWPE fabric with multilayer film lamination	130 × 130	.357 Magnum	435.9 ± 9	BFD values: 13.5–19 mm
Zhu 2023 [98]	UHMWPE + aramid fabric (PPTA)	not reported	9 mm FMJ	not reported	BFD values: 21–38 mm
Kukle 2024 [44]	14 different hybrid ballistic packages (Kevlar®, UHMWPE, graphene coatings, aerogel layers)	225 × 225	9 mm FMJ	425 – 440	BFD values: 17–39 mm

Table 1.1. Scientific research on flexible ballistic panels, continuation

Author / year	Specimen / Material	Dimensions (mm)	Ammunition	Projectile Velocity (m/s)	Key Findings
Leiva Palomera 2025 [47]	Kevlar® 29 + polyurethane	300 × 250	9 mm FMJ .22	not reported	the 9 mm bullet perforated all specimens
Kondor 2025 [43]	-Kevlar CT709 -Kevlar CT709 + Epoxy resin -Kevlar CT709 + polyurea	300 × 300	9 mm Parabellum	not reported	numerical simulation–based validation
Alexe 2025 [8]	Reviews and compares different hybrid ballistic packages from the literature	not reported	9 mm FMJ .44 Magnum 5.56 × 45 mm	not reported	-

1.6. Conclusions and future work

The thesis aimed to investigate hybrid ballistic panels, starting from a monomaterial architecture tested against 9×19 mm FMJ and .357 SIG FMJ calibers, which was subsequently optimized through hybridization to improve energy dissipation and overall resistance. The structures were manufactured from advanced semi-finished materials supplied by Teijin Aramid (Twaron® T730 [99], [100]), DuPont (Kevlar® XDS002 [112], Kevlar® EXO™ CoreMatrix™ [109]), and Avient Corporation (Dyneema® SB21 [113]).

The objectives included a current review of flexible hybrid panels, the design and fabrication of new configurations (including recent materials not previously reported in the open-source literature), experimental testing, the development of a mesoscale FEM model for optimization, and the analysis of panel failure mechanisms using high-speed imaging, high-resolution photography, and scanning electron microscopy (SEM).

CHAPTER 2

STRUCTURE OF THE THESIS

Figure 2.1 provides a schematic representation of the thesis structure.

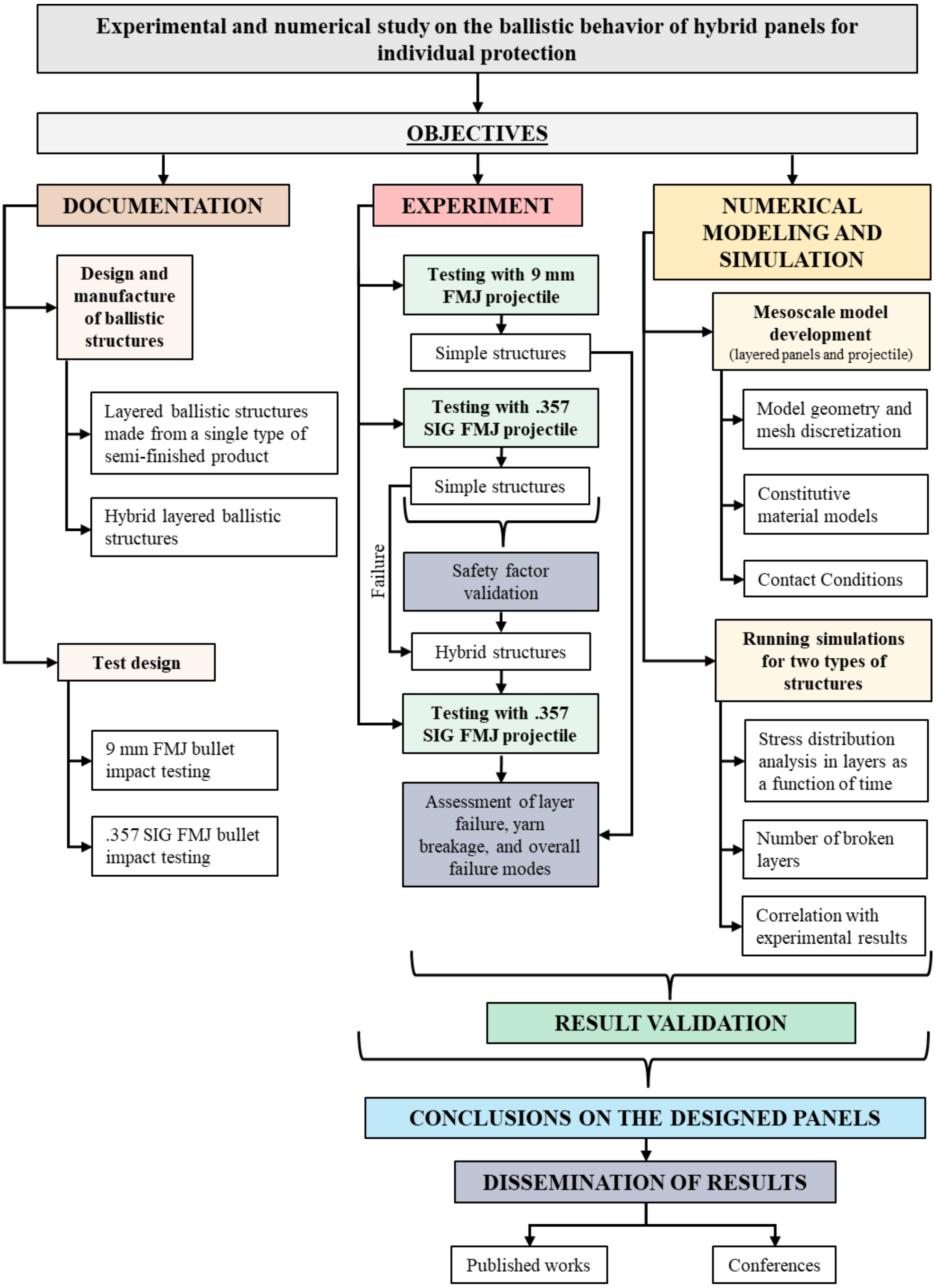

Fig. 2.1. Diagram of the thesis structure

CHAPTER 3

FINITE ELEMENT SIMULATION OF PROJECTILE–TARGET IMPACT

3.1. Finite element meshes for impact modeling

There are two fundamental approaches for formulating the physical equations that describe phenomena: the Eulerian method and the Lagrangian method. The Eulerian method, considered a "spatial" approach, is typically associated with the finite difference method (FDM). The Lagrangian method, known as a "material" approach, is generally represented by the finite element method (FEM) [37], [78], [79], [85].

3.2. Constitutive modeling and failure criteria

3.2.1. Constitutive models for materials

In the analysis of projectile impact on protective panels, the use of temperature-independent material properties is justified by thermographic observations and models reported in the literature. Studies indicate that materials such as aramid- or glass-fiber-reinforced composites maintain their mechanical properties over a wide temperature range. For the impact of a 9 mm bullet at velocities of 250–400 m/s, the process is treated as isothermal, since thermal effects are minor compared to the dominant failure mechanisms: fracture, deformation, delamination, and friction [9], [37], [51].

The bilinear hardening model is frequently used in analyses involving large deformations. This model defines the stress–strain curve based on the yield strength and the tangent modulus of the material under consideration. The slope of the first segment corresponds to the modulus of elasticity, E, while the slope of the second segment represents the tangent modulus [63], [75], [101]. Strain-rate-dependent models may also be adopted [41], [80], but fewer experimental data are available due to the complexity of testing procedures and measurement devices.

3.2.2. Maximum equivalent plastic strain (EPS) failure criterion

In finite element impact modeling using ANSYS Explicit Dynamics, material failure criteria are essential for describing material behavior under extreme loading conditions. The correct selection of a failure criterion significantly influences the accuracy of results, particularly in simulations involving plastic deformation, cracking, fracture, or other forms of material damage.

The criterion assumes that fracture initiation occurs when the accumulated equivalent plastic strain reaches a critical value specific to the material. In simulations performed with ANSYS Explicit Dynamics, reaching the critical equivalent plastic strain value leads to the loss of kinematic continuity through the separation of nodes shared by adjacent elements, without deleting elements from the model. This approach preserves mass and internal energy while providing a numerically stable description of crack propagation under impact conditions. The

EPS criterion defines the condition for fracture initiation without explicitly modeling the micromechanical mechanisms of ductile fracture. Nevertheless, due to its numerical robustness and reduced parameter requirements, it is widely used in impact simulations [11], [18], [91], [101].

In this thesis, material failure is modeled in impact simulations performed with ANSYS Explicit Dynamics (2023) using the maximum equivalent plastic strain (EPS) failure criterion. This approach is phenomenological and is frequently employed in explicit dynamic analyses due to its numerical robustness and the limited number of calibration parameters required.

3.3. Modeling projectile impact on multilayer ballistic panels

3.3.1. Model overview

This subsection analyzes the impact of a projectile on two distinct configurations of ballistic panels, differentiated by their layered construction. The first model investigated consists of 15 layers of Twaron® T730, while the second model comprises 1 layer of Kevlar® EXO followed by 15 layers of Twaron® T730, with the objective of evaluating the influence of introducing an additional layer with different mechanical properties on the ballistic behavior of the assembly. It should be emphasized that the material models were based on data from the literature, while for EXO only a model with enhanced parameters was proposed, derived from observations of the experimental results.

The models developed by the author are presented below: a projectile–layered ballistic panel impact model made from a single material type, and a projectile–layered ballistic panel impact model composed of two material types. The details of the two models are summarized in Table 3.1 and Table 3.2.

Table 3.1. Parameters of the 15-layer Twaron T730 ballistic panel impact model

	Constitutive models for materials
Bullet jacket (brass)	Bilinear isotropic hardening model
Core (lead or lead alloy)	
Layers of Twaron T730 fabric	
	Model geometry
Panel (15 Twaron T730 layers)	15 layers, layer thickness: 0.4 mm 120 mm × 120 mm
.357 SIG bullet	jacket thickness: 0.6 mm
	Constraints and boundary conditions
Panel	Fully constrained along two opposite edges
	Contact conditions
Bullet (jacket + core)	Friction Coefficient of friction: 0.5; dynamic coefficient of friction: 0.5
15-layer Twaron panel	Friction Coefficient of friction: 0.2; dynamic coefficient of friction: 0.5

Table 3.2. Details of the projectile–panel impact model with one Kevlar EXO layer and 15 Twaron T730 layers

	Constitutive models for materials
Bullet jacket (brass)	Bilinear isotropic hardening model
Core (lead or lead alloy)	
Layers of Twaron T730 fabric	
Kevlar EXO layer	
	Model geometry
Panel (1 Kevlar EXO + 15 Twaron T730 layers)	1 EXO layer, thickness: 0.6 mm 15 Twaron layers, layer thickness: 0.4 mm 120 mm x 120 mm
.357 SIG bullet	jacket thickness: 0.6 mm
	Constraints and boundary conditions
Panel	Fully constrained along two opposite edges
	Contact conditions
Bullet (jacket + core)	Friction Coefficient of friction: 0.5; dynamic coefficient of friction: 0.5
Panel (1 Kevlar EXO + 15 Twaron T730 layers)	Friction Coefficient of friction: 0.2; dynamic coefficient of friction: 0.5

3.3.2. Projectile impact model for a single-material layered ballistic panel

The developed model consists of multiple bodies: the projectile, which includes two components (jacket and core) connected via a frictional contact, and the 15-layer panel, for which the interaction condition is also defined as frictional contact. By introducing friction, the simulation becomes more realistic. When friction is taken into account, the projectile undergoes less deformation [62].

The panel has an area of 120 mm × 120 mm and consists of 15 layers, with rigid clamping on two opposite sides, and a total thickness equal to the sum of the constituent layer thicknesses. A single impact is simulated at the center of the panel.

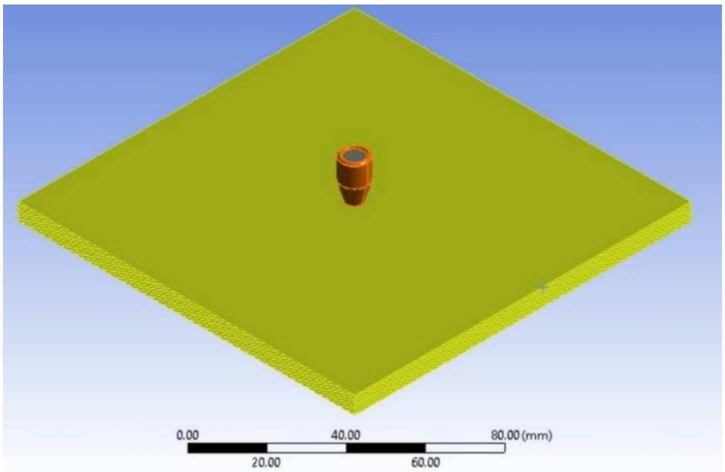

Fig. 3.1. 15-layer Twaron T730 model

The .357 SIG bullet was modeled by the author, and the geometric parameter values are highlighted in Figure 3.2, with the jacket thickness being 0.6 mm.

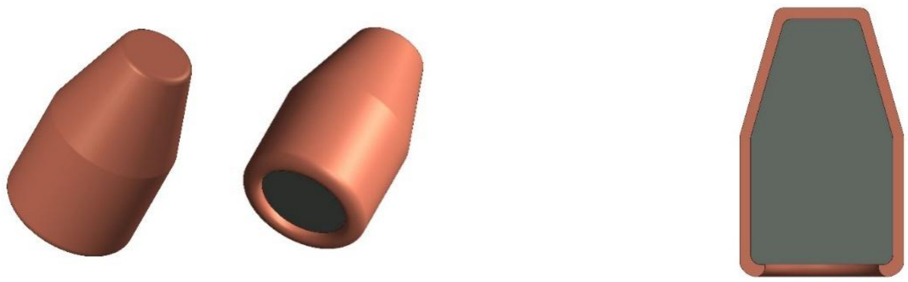

a) .357 SIG bullet model b) section view of the .357 SIG bullet model

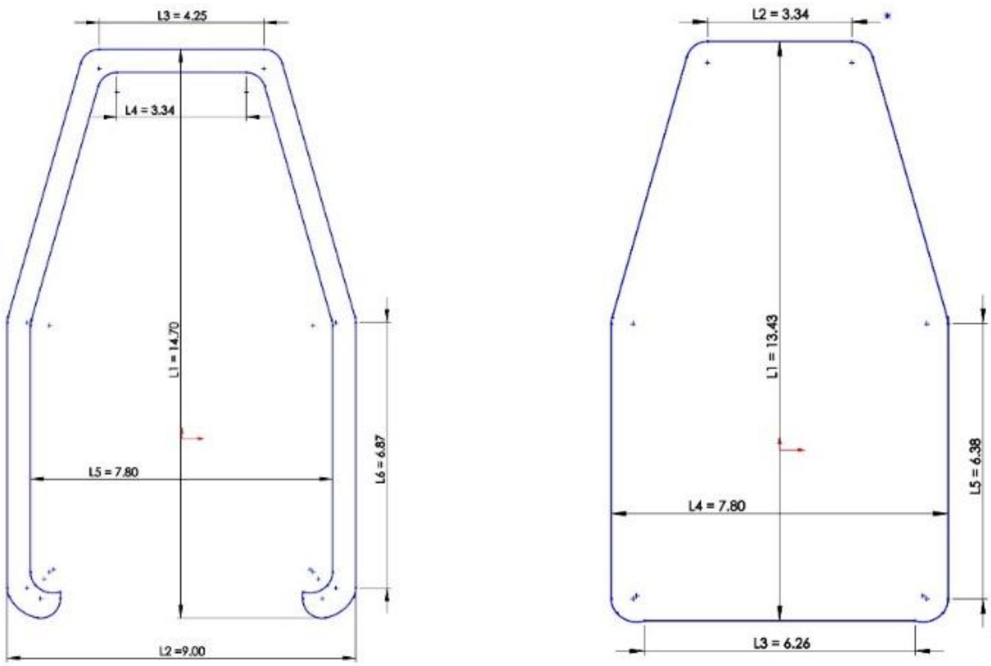

c) geometric dimensions of the jacket d) geometric dimensions of the core

Fig. 3.2. .357 SIG bullet modeled by the author

Figure 3.3 shows the elements used for each body and the discretization mesh associated with the numerical model. The projectile is represented by two distinct bodies, discretized with an automatically generated mesh composed predominantly of tetrahedral elements. The front part, with its conical geometry, features mesh refinement in the contact zone in order to better capture local impact phenomena. The 15-layer structure is discretized using regular hexahedral elements, uniformly arranged, ensuring numerical stability and an accurate representation of stress and strain fields during impact. The element size is selected to provide a coherent transition between the projectile and target discretizations, enabling a correct simulation of the interaction between the two bodies.

The numerical model is discretized into a total of 219,674 finite elements and 441,036 nodes, providing an adequate level of resolution to capture the transient phenomena associated with ballistic impact.

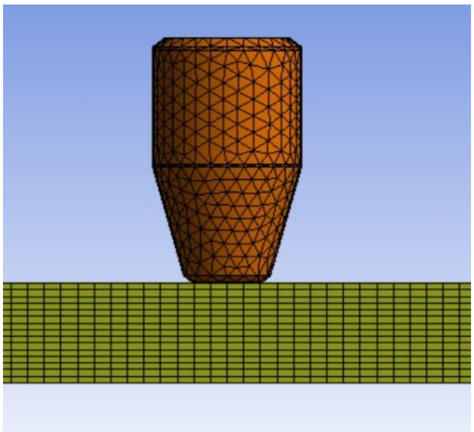

Fig. 3.3. discretization mesh for the bullet and the Twaron T730 layers

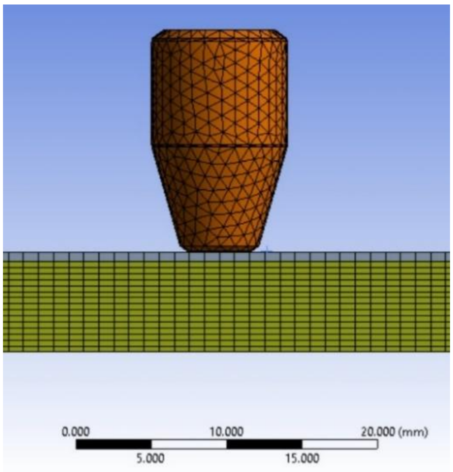

Fig. 3.4. discretization mesh for the bullet and the hybrid panel with one Kevlar® EXO layer and 15 Twaron T730 layers

3.3.3. Numerical model of projectile impact on a Kevlar EXO/ Twaron layered panel

The developed model consists of multiple bodies: the projectile, which includes two components (jacket and core) connected via a frictional contact, and the panel composed of one Kevlar EXO layer and 15 Twaron T730 layers, with frictional interaction conditions.

The model dimensions are as follows: the panel has an area of 120 mm × 120 mm and is rigidly clamped on two opposite sides. A single impact is simulated at the center of the panel.

The discretization mesh is the same as in the previous case (Fig. 3.4). This numerical model includes a total of 234,049 finite elements and 470,313 nodes, indicating a denser discretization compared to the model consisting exclusively of Twaron T730 layers, due to the introduction of the additional layer with different mechanical properties. This approach ensures an accurate representation of interlayer interactions and an adequate capture of the stress and strain gradients generated during impact.

3.3.4. Constitutive material models in the developed model

In these simulations, the following constitutive material models were used:

- bullet jacket (brass): bilinear hardening model, homogeneous and isotropic;
- core (lead or lead alloy): bilinear hardening model, homogeneous and isotropic.

The panel layers have the mechanical properties listed in Tables 3.4; however, the constitutive model for each layer was assumed to be homogeneous and isotropic with bilinear hardening. This simplification is acceptable provided that the model exhibits realistic behavior and, for certain cases (e.g., number of panel layers), is validated through experimental testing.

The failure criterion for each layer and for the projectile jacket was the equivalent plastic strain at failure (EPS).

Table 3.3. Mechanical properties of the bullet jacket and core

Mechanical properties of the jacket			Mechanical properties of the core	
Property	**Value**		**Property**	**Valoare**
Density *[kg mm^{-3}]*	8,30e-006		Density *[kg mm^{-3}]*	1,134e-005
Young's Modulus *[MPa]*	1,2e+05		Young's Modulus *[MPa]*	11000
Poisson's Ratio	0,34		Poisson's Ratio	0,44
Bulk Modulus *[Pa]*	1,25e+11		Bulk Modulus *[Pa]*	3,055e+10
Shear Modulus *[Pa]*	4,4477e+10		Shear Modulus *[Pa]*	3,819e+09
Temperature *[˚C]*	22		Temperature *[˚C]*	22
Bilinear isotropic hardening model			**Bilinear isotropic hardening model**	
Initial yield stress *[MPa]*	70		Initial yield stress *[MPa]*	15
Tangent modulus *[MPa]*	2000		Tangent modulus *[MPa]*	40
Temperature *[˚C]*	22		Temperature *[˚C]*	22
			Equivalent plastic strain at failure	2

Table 3.4. Mechanical properties of the Twaron T730 and EXO layers

Mechanical properties of the Twaron T730 layers			Mechanical properties of the EXO layers	
Property	**Value**		**Property**	**Value**
Density *[kg mm^{-3}]*	1,444e-006		Density *[kg mm^{-3}]*	1,444e-006
Young's Modulus *[MPa]*	90000		Young's Modulus *[MPa]*	90000
Poisson's Ratio	0,35		Poisson's Ratio	0,35
Bulk Modulus *[Pa]*	1e+11		Bulk Modulus *[Pa]*	1e+11
Shear Modulus *[Pa]*	3,3333e+10		Shear Modulus *[Pa]*	3,3333e+10
Temperature *[˚C]*	22		Temperature *[˚C]*	22
Bilinear isotropic hardening model			**Bilinear isotropic hardening model**	
Initial yield stress *[MPa]*	400		Initial yield stress *[MPa]*	800
Tangent modulus *[MPa]*	18000		Tangent modulus *[MPa]*	18000
Temperature *[˚C]*	22		Temperature *[˚C]*	22
Equivalent plastic strain at failure	0,095		**Equivalent plastic strain at failure**	0,15

The model used is isothermal, and this simplification is supported by two main arguments: on the one hand, Explicit Dynamics does not support adiabatic models, and on the other hand, studies reported in the literature indicate that within the impact velocity range of 250 m/s to 450 m/s, thermal effects can be considered negligible in the analysis of projectile and target failure.

3.3.5. Impact case on the panel consisting of 15 Twaron T730 layers at an impact velocity of 450 m/s

Friction between the bullet and the layers influences how loads are distributed and transferred, hindering the projectile's rapid motion and contributing to increased stresses in the material, as well as to the conversion of part of the projectile's kinetic energy into frictional energy.

In this simulation, at 7.5×10^{-6} s, the first layer is observed to fail, according to the graph in Figure 3.5c, at an equivalent stress of approximately 2464.1 MPa. Layers 2 and 3 also exhibit high equivalent stresses.

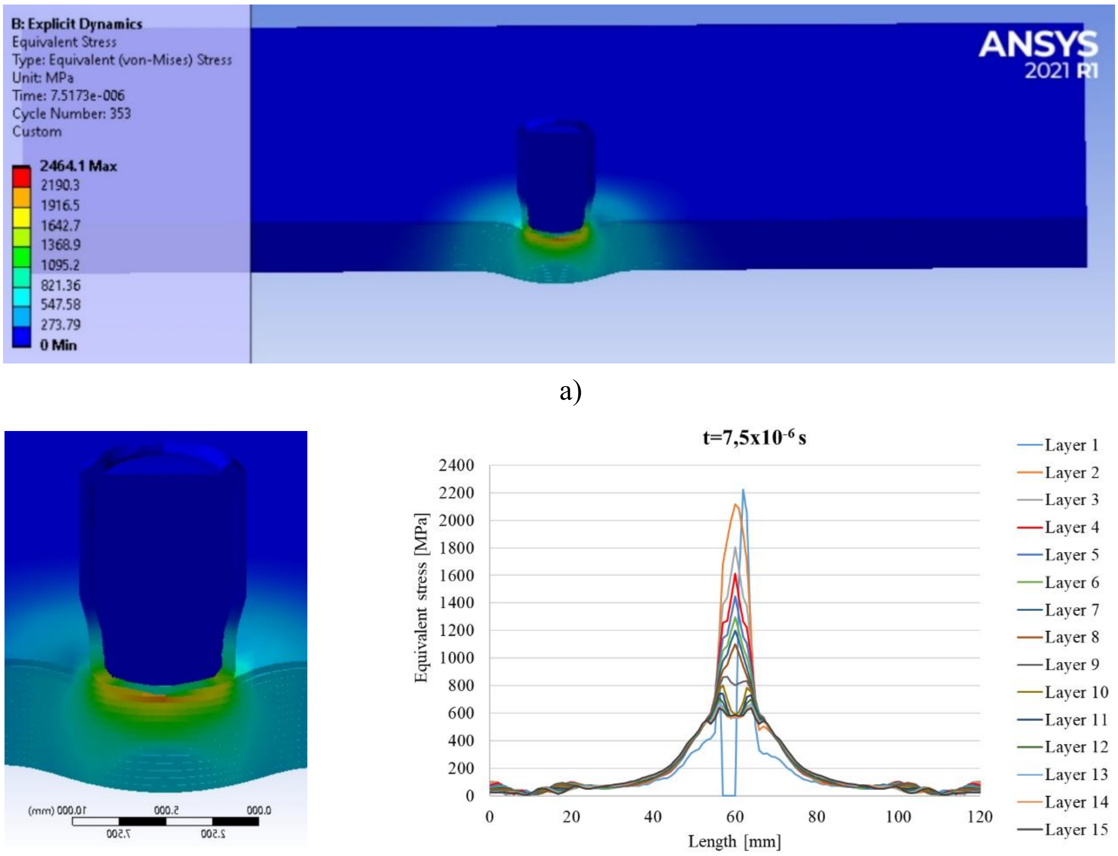

a)

b) c)

Fig. 3.5. Distribution of equivalent stresses during the impact of a .357 SIG projectile on the 15-layer Twaron T730 panel at time $t = 7.5 \times 10^{-6}$ s: (a) view of the central section through the system (along the projectile axis); (b) detail of the direct contact zone (same color scale as in (a)); equivalent stress graph for each layer in the central section.

At $t = 3.75 \times 10^{-5}$ s (Fig. 3.6), the phase in which the shock wave has already penetrated several layers becomes evident. Failure of layers 2 and 3 is observed, and the maximum stress is no longer confined to the front layer. The pronounced central peak indicates the contact zone and the intense transmission of compressive loads through the thickness, with layer 4 reaching the highest values—an indication of damage concentration in the region where energy begins to be dissipated through fiber stretching and surface waviness.

The significant difference between layers 1–5 and the rear layers shows that the absorption process remains localized in the front half of the package. The elevated lateral zones (at 30–40 mm and 80–90 mm) reflect the onset of flexural wave propagation in the plane of the panel, although they do not yet dominate the global structural response.

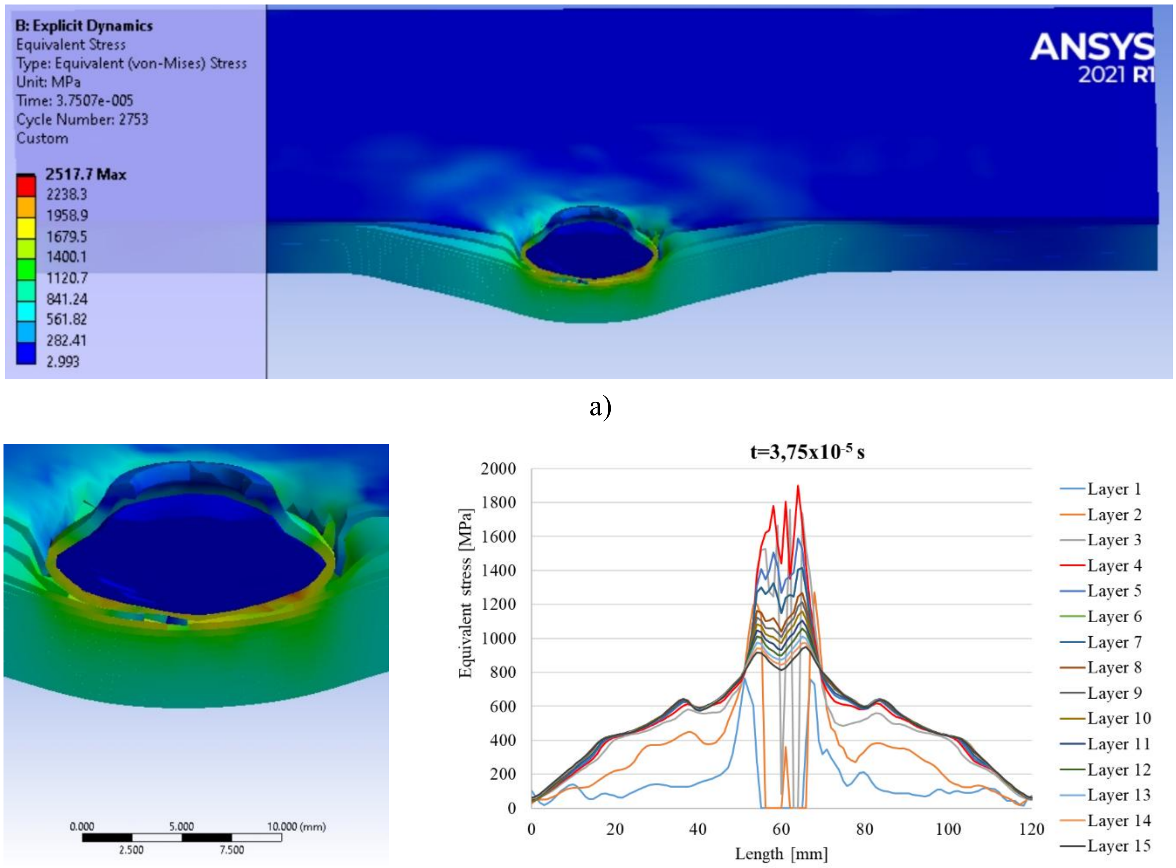

a) b) c)

Fig. 3.6. Distribution of equivalent stresses during the impact of a .357 SIG projectile on the 15-layer Twaron T730 panel at time t = 3.75 × 10^{-5} s: (a) view of the central section through the system (along the projectile axis); (b) detail of the direct contact zone (same color scale as in (a)); equivalent stress graph for each layer in the central section.

At t = 1.5 × 10^{-4} s (Fig. 3.7), the stress distributions indicate a clear post-impact regime (values below the yield limit of the material model), dominated by the global vibration of the panel. The central zone (45 – 80 mm) exhibits low and oscillatory stress levels for most layers, indicating that the local impact energy has already been dissipated and that the region is in a phase of dynamic relaxation.

The pronounced maxima in the lateral regions (15 – 30 mm and 95 – 110 mm) are associated with the bending modes of the layers and wave reflections at the panel boundaries, rather than with local penetration. The differences between layers are moderate, showing that the structure is now acting as an integrated system, with loads distributed through the thickness and without persistent critical stress concentrations in the impact zone.

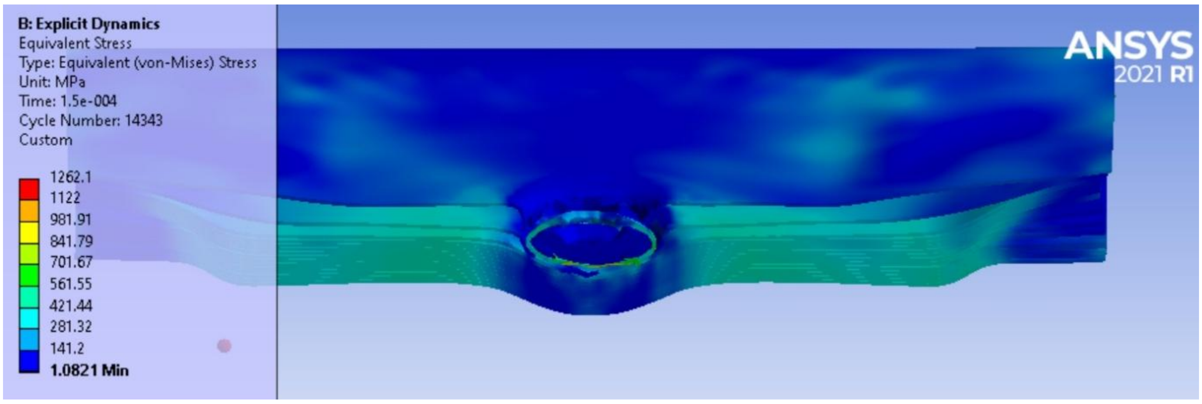

a)

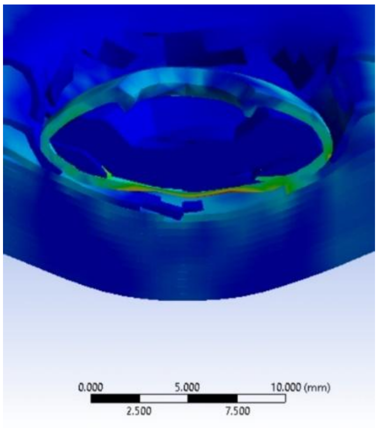

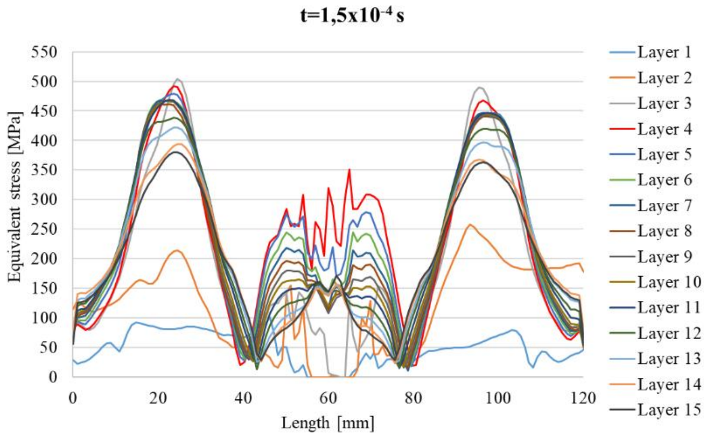

b) c)

Fig. 3.7. Distribution of equivalent stresses during the impact of a .357 SIG projectile on the 15-layer Twaron T730 panel at time t = 1.5 × 10^{-4} s: (a) view of the central section through the system (along the projectile axis); (b) detail of the direct contact zone (same color scale as in (a)); equivalent stress graph for each layer in the central section.

Following ballistic tests performed on the panel consisting of 15 Twaron T730 layers, tested with .357 SIG ammunition, it was experimentally observed that the projectiles corresponding to shots 1 and 2 were stopped at the level of layer 4. Correlating these observations with the results obtained from the numerical model confirms the tendency of the layered structure to absorb most of the impact energy within the front layers. The simulation shows a concentration of damage and maximum stresses in the region of layers 1–4, supporting the experimental conclusion that, under certain impact conditions, a 15-layer Twaron T730 package can stop a .357 SIG bullet within the first 3–4 layers of the configuration.

Figure 3.8a presents the projectile resulting from the simulation, while Figure 3.8b shows a photograph of the .357 SIG bullet stopped at layer 4. The deformed shape of the real projectile is similar to that obtained in the simulation, indicating that the simulation can be considered realistic and that the model is suitable for studying impact behavior and for optimizing the panel by modifying the number of layers.

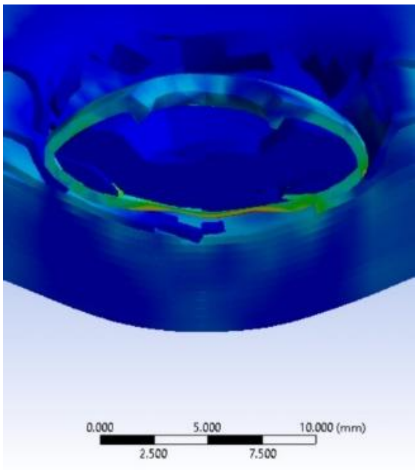

a) projectile arrested in layers 3–4 of the numerical model

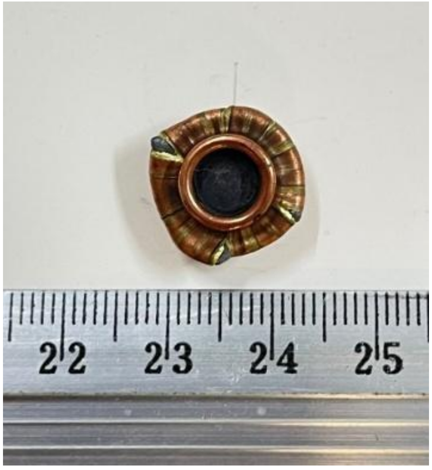

b) projectile from shot 2, arrested in layer 4

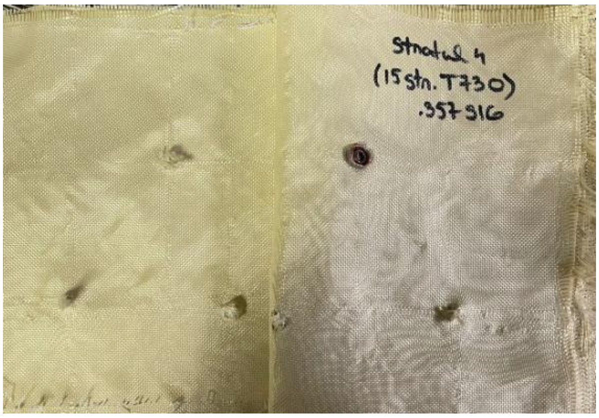

c) identification of bullet 1 at layer 4 during experimental testing

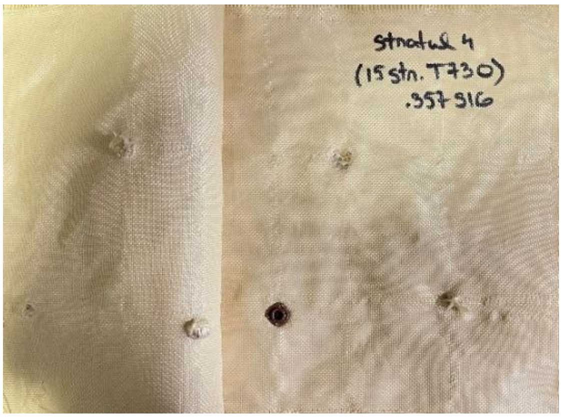

d) identification of bullet 2 in layer 4 from experimental tests

Fig. 3.8. Numerical–Experimental Comparison for the 15-Layer Twaron T730 Panel under .357 SIG Impact

3.3.6. Impact case on the hybrid panel consisting of one Kevlar EXO layer and 15 Twaron T730 layers at an impact velocity of 450 m/s

At $t = 7.5 \times 10^{-6}$ s (Fig. 3.9), no failure of the EXO layer is observed; however, the equivalent stresses reach significant values, approaching the failure limit (2354.3 MPa for layer 1, according to Fig. 3.9a). The concentrated von Mises stress field in the front layer indicates that the first layer (the EXO layer) absorbs most of the local loading, dissipating energy through deformation and the initiation of damage. The rear layers are still weakly stressed, indicating that the shock wave has not yet significantly penetrated the layered package, confirming the critical role of the first layer in attenuating the stress peak.

The graph in Figure 3.9c presents the distribution of equivalent stress in each layer, along the main section (containing the projectile axis), at $t = 7.5 \times 10^{-6}$ s, capturing the initial propagation of the shock wave through the layered package. A pronounced peak is observed in the central impact region, where layer 1 (EXO) reaches the maximum values, significantly higher than those in the other layers and greater than those obtained at the same moment for the single-material panel. The progressive decrease in stress amplitude from layer 1 toward the deeper layers indicates effective attenuation of the shock wave through the thickness, due to fiber deformation mechanisms. The rear layers exhibit a much more diffuse and lower-level response, showing that, in this early stage of impact, the energy has not yet been fully transmitted to the back of the panel.

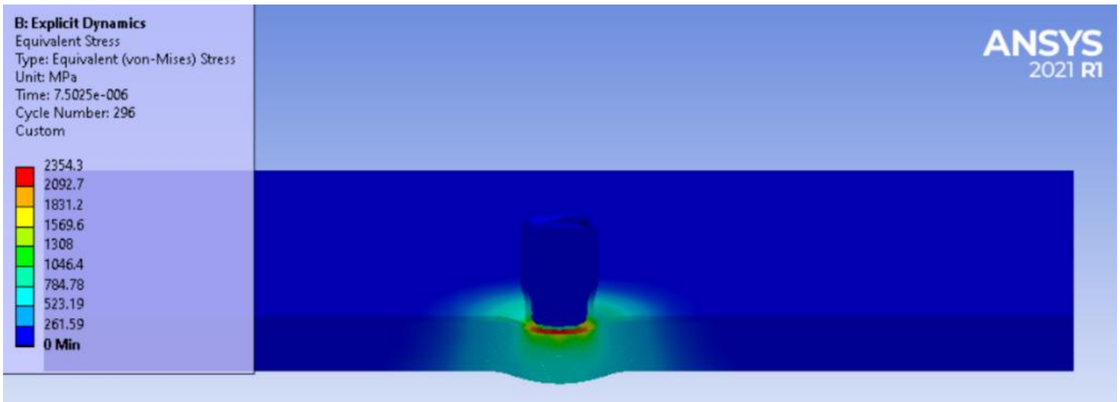

a)

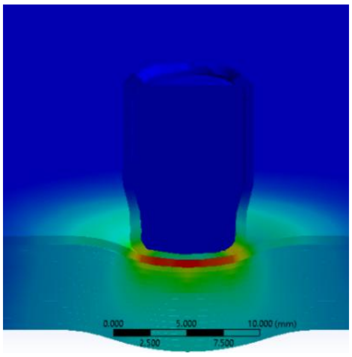

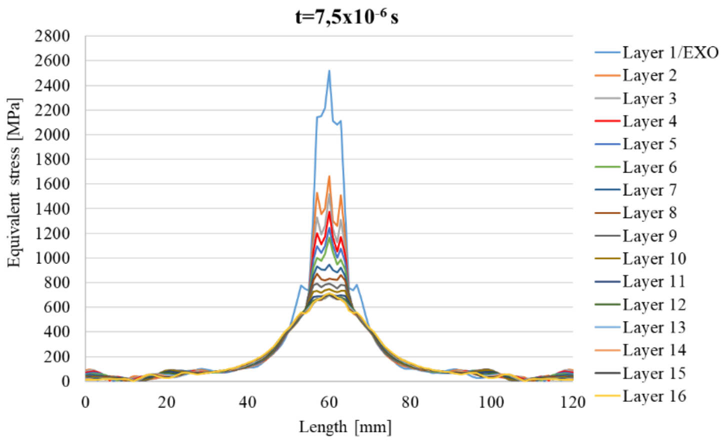

b) c)

Fig. 3.9. Distribution of equivalent stresses during the impact of a .357 SIG projectile on the hybrid panel (1 EXO layer + 15 Twaron T730 layers) at time $t = 7.5 \times 10^{-6}$ s: (a) view of the central section through the system (along the projectile axis); (b) detail of the direct contact zone (same color scale as in (a)); equivalent stress graph for each layer in the central section.

At $t = 3.75 \times 10^{-5}$ s, the graph in Figure 3.10c shows a more advanced stage of shock wave propagation, in which the load is no longer concentrated strictly at the impact point but has been distributed spatially and through the thickness of the package. The peak in layer 1 remains the highest, but the differences compared to layers 2–6 have decreased, indicating a progressive transfer of load to the inner layers. The shape with two lateral maxima and a local decrease at the center suggests the onset of a regime dominated by flexural deformation and membrane stretching, rather than purely local compression. The rear layers begin to actively participate in load bearing, confirming that the impact energy is being redistributed over a larger area, reducing the risk of local perforation while increasing the global loading of the panel.

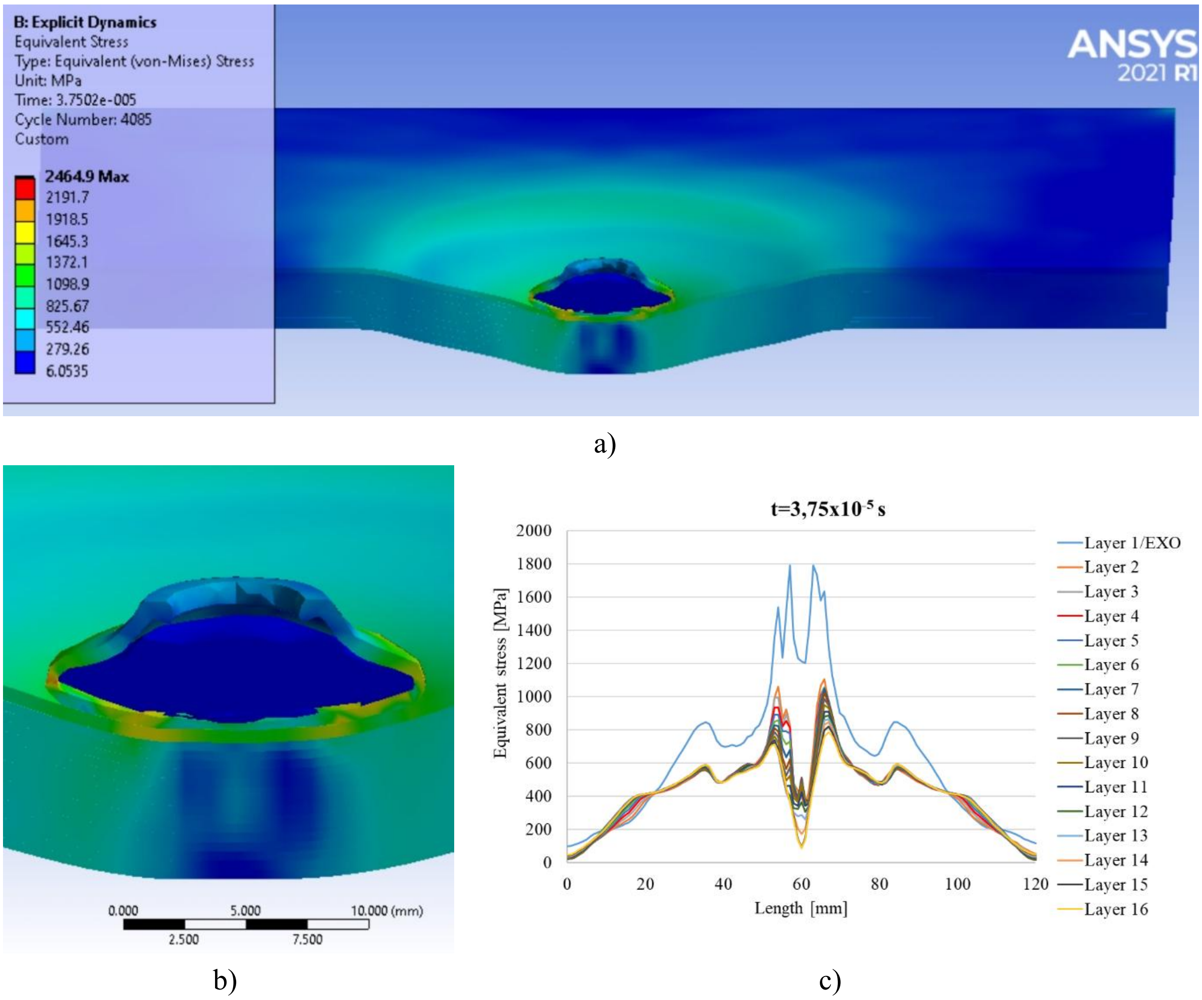

Fig. 3.10. Distribution of equivalent stresses during the impact of a .357 SIG projectile on the hybrid panel (1 EXO layer + 15 Twaron T730 layers) at time $t = 3.75 \times 10^{-5}$ s: (a) view of the central section through the system (along the projectile axis); (b) detail of the direct contact zone (same color scale as in (a)); (c) equivalent stress graph for each layer in the central section.

The graph at $t = 1.5 \times 10^{-4}$ s (Fig. 3.11) shows an advanced stage of the structural response, in which the behavior is dominated by the global flexural vibration of the panel. The stress distributions become more uniform across the layers, and the differences between them are significantly smaller than in the initial phases, indicating that the impact energy has already been redistributed throughout the entire laminated package.

Alternating maxima and minima can be observed along the length, characteristic of the plate's natural vibration modes (flexural waves reflected at the boundaries). Layer 1 no longer concentrates the maximum local stress, indicating that the critical phase of primary energy absorption has ended and that the structure is in a global dynamic response regime, with moderate stresses distributed over a large surface area.

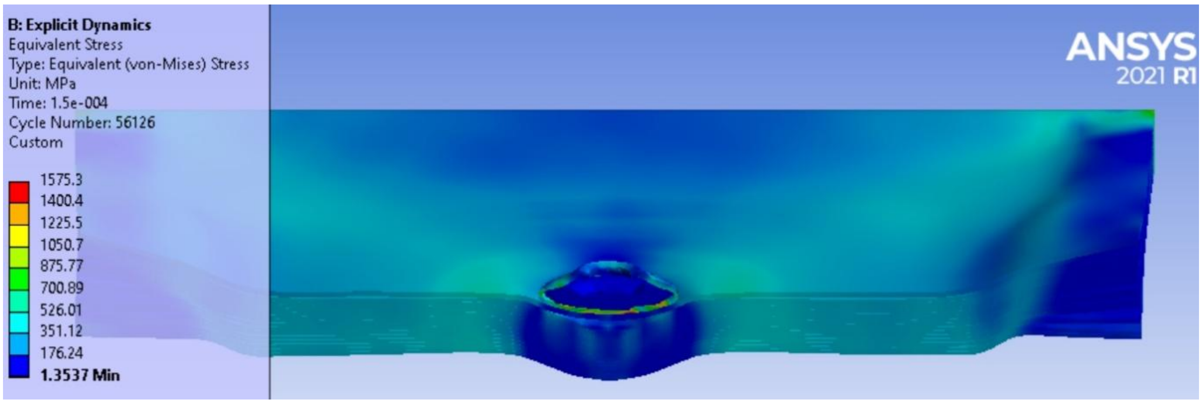

a)

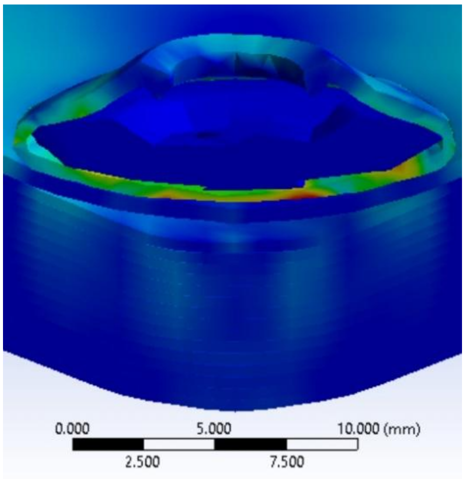

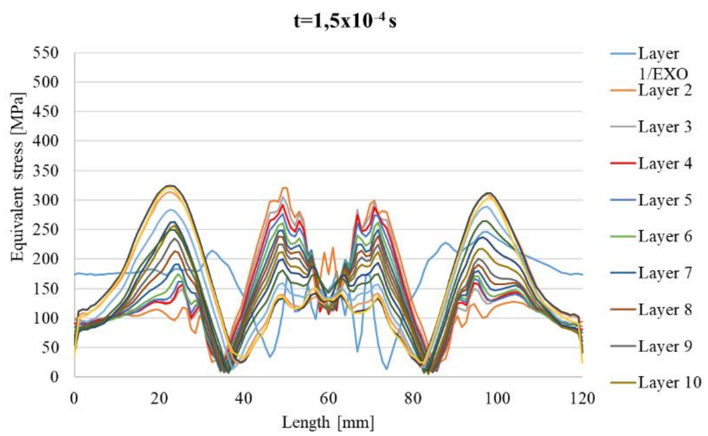

b) c)

Fig. 3.11. Distribution of equivalent stresses during the impact of a .357 SIG projectile on the hybrid panel (1 EXO layer + 15 Twaron T730 layers) at time t = 1.5 × 10^{-4} s: (a) view of the central section through the system (along the projectile axis); (b) detail of the direct contact zone (same color scale as in (a)); (c) equivalent stress graph for each layer in the central section.

Following ballistic tests performed on the panel composed of one Kevlar® EXO layer and 15 Twaron T730 layers, using .357 SIG ammunition, it was experimentally observed that, in all four tested specimens, each of the three shots was stopped by the Kevlar® EXO layer (Fig. 3.12). Correlating these experimental observations with the results obtained from numerical modeling confirms the essential role of the Kevlar® EXO layer in absorbing the majority of the impact energy. This layer carries most of the local load, dissipating energy through significant deformation and the initiation of damage mechanisms.

The simulation results highlight a concentration of maximum stresses and damage in the Kevlar® EXO layer, supporting the experimental conclusion that a package consisting of one Kevlar® EXO layer and 15 Twaron T730 layers is capable of stopping a .357 SIG projectile within the very first layer.

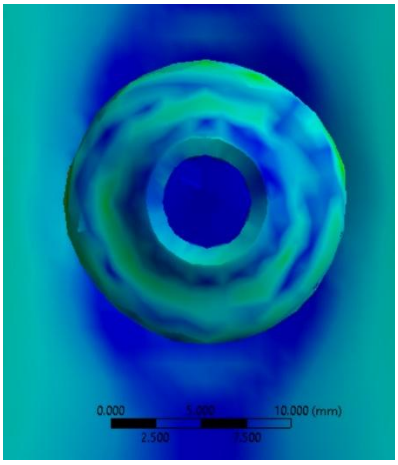

a) projectile arrested in the Kevlar® EXO layer in the numerical model

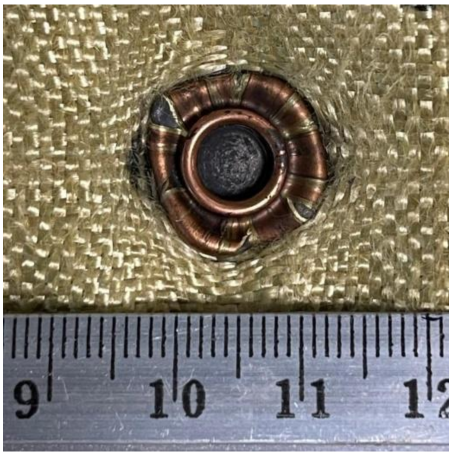

b) projectile from shot 2, arrested in the Kevlar® EXO layer

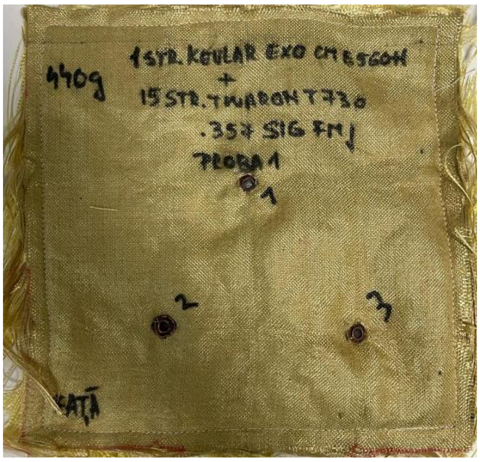

c) experimental identification of bullet 2 in the Kevlar® EXO layer

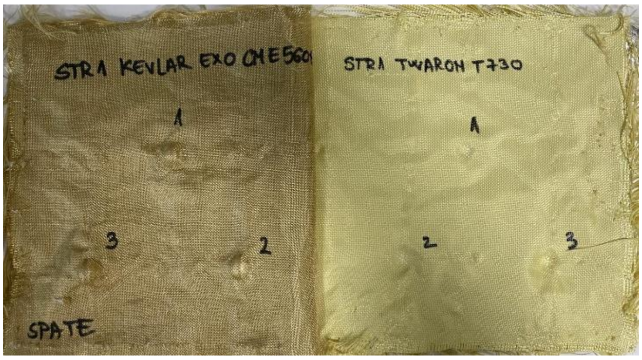

d) back-face view of the EXO layer, no complete penetration

Fig. 3.12. Numerical–experimental comparison for the Kevlar® EXO/Twaron T730 hybrid panel under .357 SIG Impact

3.3.7. Equivalent von Mises stress distribution through the layers for both panels

This subsection presents the distribution of equivalent (von Mises) stresses at the level of each constituent layer for the two structural configurations analyzed. The objective is to identify critical stress regions and to highlight how the layered architecture influences load transfer and energy dissipation mechanisms.

The graphs in Figure 3.13a show that, immediately after impact ($t = 7 \times 10^{-6}$ s), the structure with Kevlar® EXO develops a significantly higher and more concentrated equivalent stress peak in the impact zone (~60 mm), indicating rapid load uptake and initial energy dissipation in the first layer. As time progresses ($t = 3.75 \times 10^{-5}$ s $\rightarrow$ 1.5×10^{-4} s), the stresses in the Kevlar® EXO configuration redistribute over a greater length while maintaining higher levels than the panel without EXO, suggesting that wave propagation and load transfer are more effectively managed by the front layer.

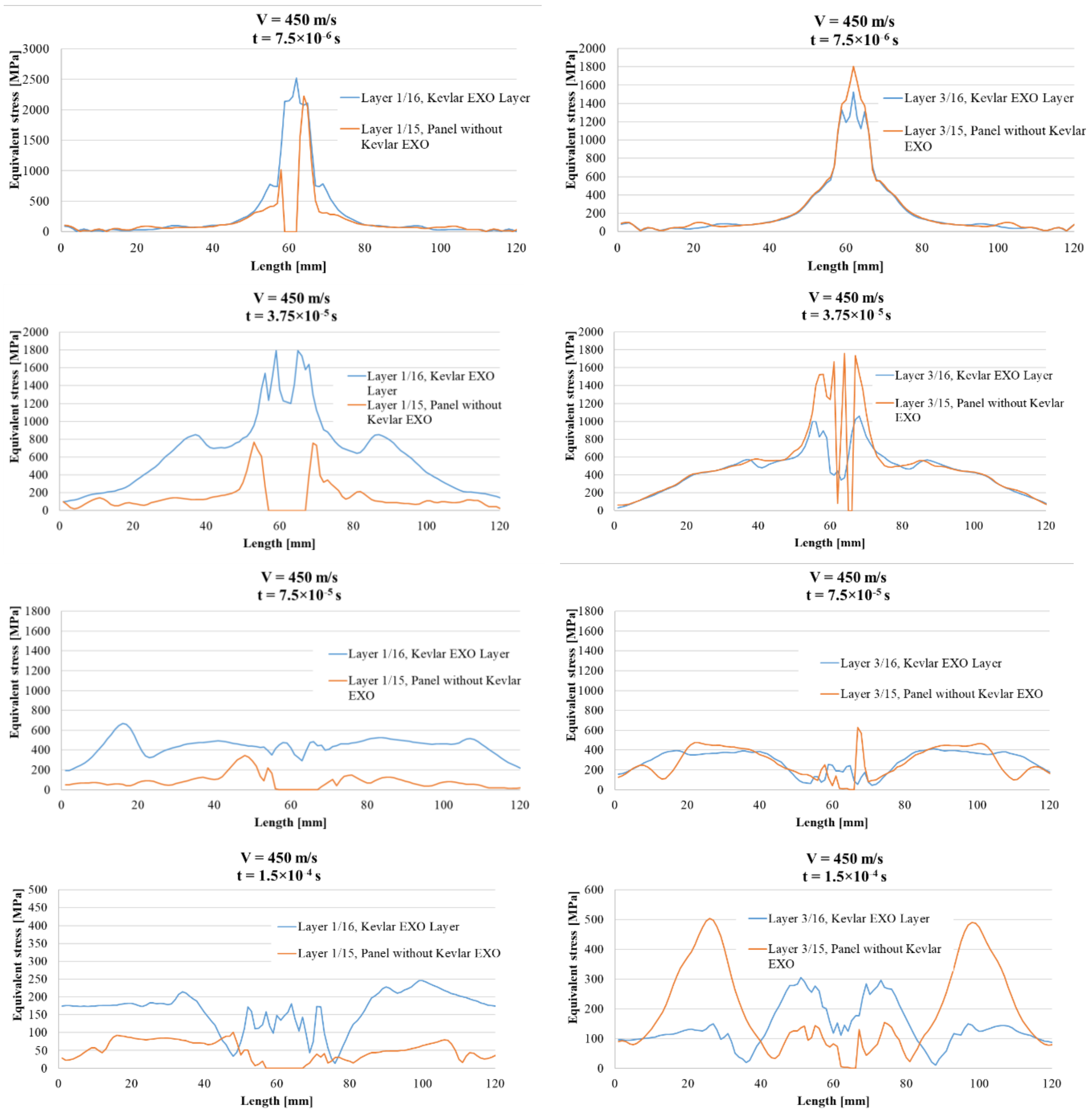

a) equivalent stress analysis for layer 1　　　　b) equivalent stress analysis for layer 3

Fig. 3.13. Comparison of equivalent stresses in layers 1 and 3 for both ballistic configurations (450 m/s)

In contrast, the panel without EXO exhibits lower and less extensive stress levels, suggesting that the energy is transmitted further to the subsequent layers rather than being predominantly absorbed in the front layer. This evolution confirms the role of the Kevlar® EXO layer in the initial concentration of the load and in the progressive attenuation and redistribution of stresses, contributing to stopping the projectile within the first layer, even if localized failures occur.

For layer 3 (Fig. 3.13b), immediately after impact ($t = 7 \times 10^{-6}$ s), a pronounced central stress peak is observed for both configurations; however, the panel without Kevlar® EXO develops slightly higher values, indicating a faster transmission of the shock wave to the inner layers. At intermediate times ($t = 3.75 \times 10^{-5}$ s and 7×10^{-5} s), the difference becomes clearer:

the structure without EXO maintains high and oscillatory concentrations of equivalent stress in the impact zone, whereas the EXO configuration exhibits a more uniform distribution and lower values, indicating that a significant portion of the energy has already been dissipated in the front layers. Toward the end of the analyzed interval ($t = 9.75 \times 10^{-5}$ s and 1.5×10^{-4} s), stresses decrease in the central region for both cases, but the panel without EXO shows larger increases in the lateral zones, suggesting a wider propagation of the load. Overall, the evolution confirms that the presence of the Kevlar® EXO layer limits the transmission of stress peaks to the deeper layers, reducing the stress levels in layer 3.

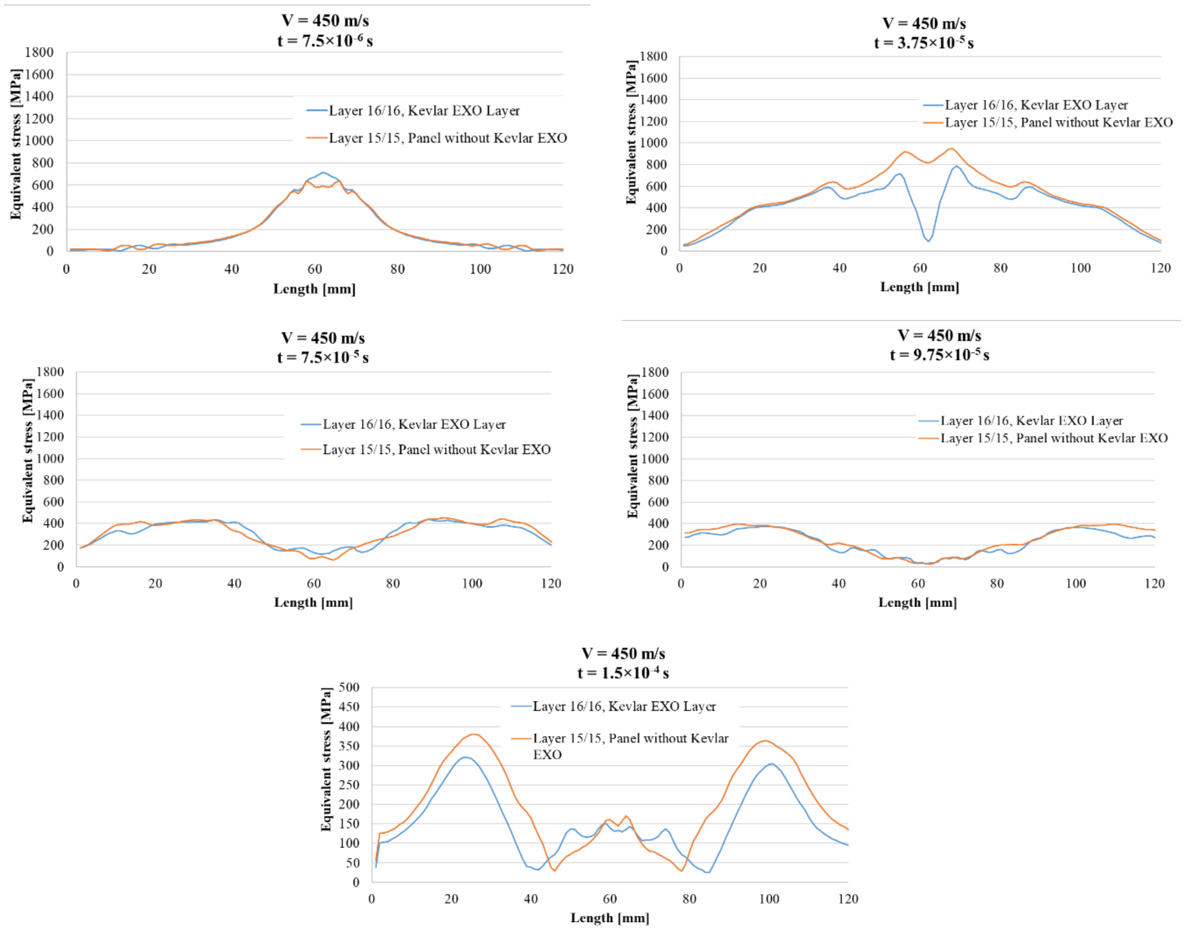

Fig. 3.14. Equivalent stress analysis for the last layer in the ballistic structures at an impact velocity of 450 m/s

For the last layer (Figure 3.14), at the initial time ($t = 7 \times 10^{-6}$ s) the stress level is still low and similar for both configurations, indicating that the shock wave has not yet significantly reached the rear region. At $t = 3.75 \times 10^{-5}$ s, a clear differentiation appears: the structure without Kevlar® EXO develops higher and more extended stresses, whereas the EXO configuration shows a pronounced minimum in the central zone, indicating attenuation of the wave as it traverses the package. As the structural response evolves ($t = 7 \times 10^{-5}$ s and 9.75×10^{-5} s), the distributions become more uniform, but the panel without EXO maintains slightly higher levels, indicating a greater transmission of residual energy. At the final time ($t = 1.5 \times 10^{-4}$ s), lateral differences are evident, with higher stresses in the structure without EXO, confirming that the presence of the Kevlar® EXO front layer significantly reduces the amplitude of the loads reaching the last layer.

3.6. Key conclusions on projectile impact simulation

The effectiveness of such simulations is closely related to the operator's knowledge of material behavior modeling, expertise in the use of the finite element method, and understanding of the processes occurring during impact.

Simulations can be essential for evaluating the safety of personal armor or ballistic plates intended for vehicle armor, highlighting specific details of the bullet failure process and its interaction with the target.

This chapter presented two impact models involving two types of layered panels and a .357 SIG projectile, analyzed at the macro level (the panel being modeled as layers considered homogeneous), highlighting the following aspects.

- All bodies and materials involved were considered within the elasto-plastic domain, applying a failure criterion based on the equivalent plastic strain at failure (EPS). Unlike other bibliographic references, where one of the bodies (usually the projectile) is assumed to be rigid, this model treats all bodies as deformable, providing a more realistic impact response but requiring particular care in the simulation setup.
- The set of graphs highlights that the virtual model, incorporating a Kevlar® EXO front layer, concentrates and absorbs most of the impact energy, significantly reducing the transmission of stress peaks to the inner layers and to the last layer. In its absence, loads propagate more intensely through the panel thickness, with higher values and more extensive stress distributions within the laminated structure. The temporal evolution confirms the role of the EXO layer in attenuating the shock wave and progressively dissipating energy through deformation and localized damage mechanisms.
- Simulations performed on similar panels, also tested experimentally, enabled model validation through comparison of the number of damaged layers.
- The analysis of equivalent stresses at different time steps and across various layers allowed the identification of the impact stages, clearly highlighting the phases associated with partial penetration.

Numerical simulation provides a major advantage by enabling detailed tracking of stress fields in both time and space—information that is difficult or impossible to obtain exclusively through experimental methods. Moreover, modeling allows for virtual testing, reducing the number of panels that must be physically tested during prototype developmen

CHAPTER 4

DEVELOPMENT OF BALLISTIC PROTECTION STRUCTURES

4.1. Semi-finished materials used in the manufacture of ballistic structures

The typical configuration of an individual ballistic protection system includes a ballistic package composed of multiple layers of materials whose primary role is to stop projectiles, enclosed within a protective textile carrier. The number of layers varies depending on the material and the required protection level, and these layers may consist of woven fabrics, unidirectional laminates, or multiaxial structures. Systems may be monomaterial or hybrid, and the order and combination of layers decisively influence performance; the presence of non-ballistic layers for trauma reduction makes comparisons based solely on the number of layers irrelevant. The assembly of flexible panels is achieved either by simple stacking within the carrier or by stitching, using various techniques such as edge stitching, point/corner stitching, parallel or diagonal lines, and quilting (diamond, square patterns, etc.), each influencing impact behavior and layer mobility.

For the manufacture of ballistic protection panels, the following semi-finished materials were used:

- Twaron® T730 (Teijin Aramid AVE) [99], [100],
- Kevlar® EXO™ CoreMatrix™ CM E1100H (DuPont) [109],
- Kevlar® XD S002 (DuPont) [112],
- Dyneema® SB21 (DSM, later Avient Corporation) [113].

Twaron® T730 fabric

Twaron® T730 fabric is a plain weave fabric with a linear density of 168 tex, based on standard tenacity (T), designed for cost-effective ballistic performance solutions that require good resistance to bullets and fragmentation [114].

Table 4.1. Twaron® T730 fabric specifications [99], [100]

Linear Density [dtexnom] Warp/Weft	Twaron Type Warp/Weft	Set [per 10 cm]		Areal Density [g/m^2]	Thickness [mm]	Minimum Breaking Strength [N/5 cm x 1000]*	
		Warp	Weft			Warp	Weft
1680 f1000	1040	78	78	260	0,4	9,4	10

* standardized form for reporting tensile strength of textile materials

Kevlar® EXO™ CoreMatrix™ CM E1100H fabric

Kevlar® EXO is a new copolymeric para-aramid fiber, structurally different from conventional aramid fibers. By incorporating an additional monomer, superior molecular alignment is achieved, resulting in increased strength and up to 30% lower weight compared to earlier versions.

The Kevlar® EXO™ CoreMatrix™ CM E1100H fabric is a 3D textile produced using the patented CoreMatrix technology [110], [111], [121] which combines multiple woven Kevlar layers with a nonwoven layer through a process that infuses discontinuous fibers in the Z-direction (vertical), adding a third dimension of protection. By eliminating traditional stitching, the material enables impact energy to be dispersed in all directions, not only along the X and Y axes.Reinforcement with Z-direction yarns not only stabilizes the layered architecture of the material but also actively contributes to protection mechanisms during impact. Through-thickness yarns keep the textile layers tightly bound, reducing their tendency to separate or slide over one another under ballistic loading. This structural cohesion improves the transfer and dissipation of kinetic energy, as the load is no longer carried solely by in-plane yarns but is distributed three-dimensionally throughout the entire volume of the semi-finished material. Consequently, Z-yarns become an integral part of the energy absorption process, limiting local deformation, delaying crack propagation, and contributing to the overall efficiency of the protection system [Development Product Specification]. At present, the only publicly available characteristics of this fabric are those presented in Table 4.2.

Table 4.2. Specifications of the Kevlar® EXO™ CoreMatrix™ CM E1100H fabric roll [110]

Property	Nominal	Low	High
Areal Density [g/m^2]	1146	1044	1248
Width [cm]	160	160	165
Thickness [mm]	2,26	1,98	2,54

The three-dimensional (3D) orientation of the yarns is illustrated in Figures 4.1 and 4.2, where their spatial distribution can be observed along the longitudinal, transverse, and through-thickness directions of the textile structure.

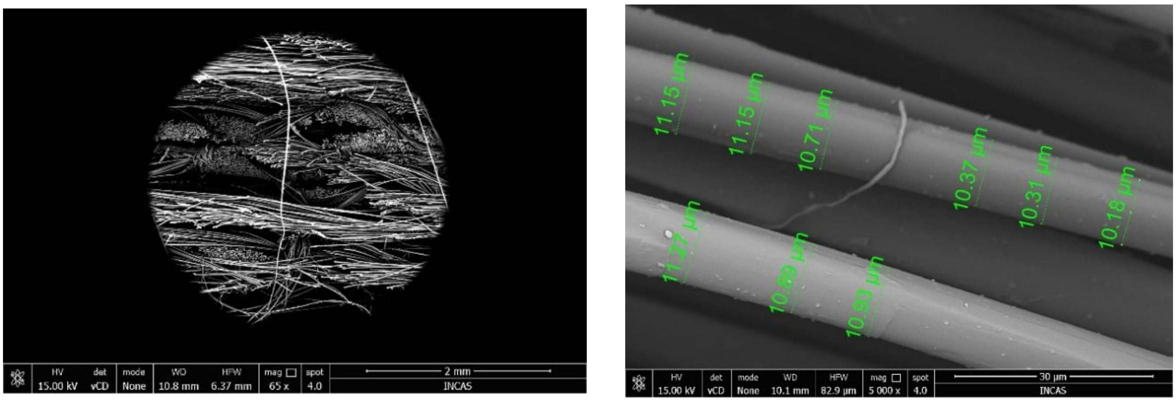

a) ×65 b) ×5000

Fig. 4.1. Crosswise-cut Kevlar® EXO™ CoreMatrix™ CM E1100H fabric images

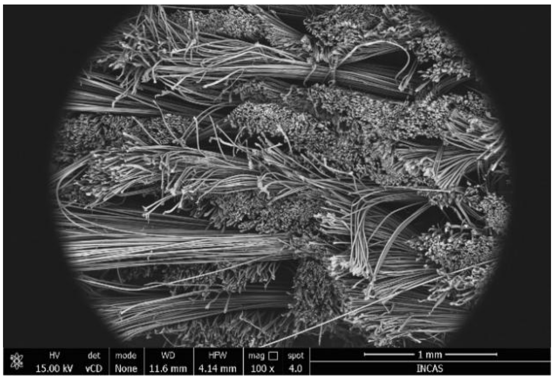

a) ×100

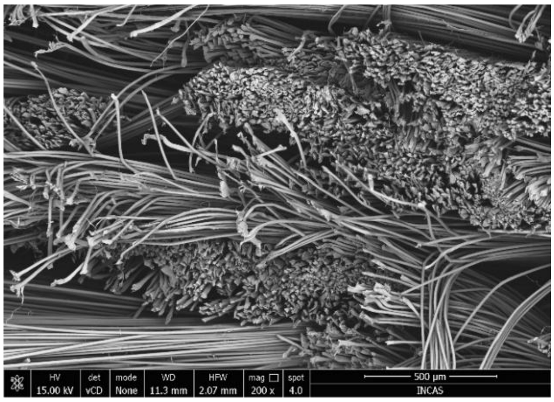

a) ×200

Fig. 4.2. Longitudinal cross-sections of the Kevlar® EXO™ CoreMatrix™ CM E1100H fabric

Kevlar® XD S002 fabric

Kevlar® XD is the result of a technology developed by DuPont™, based on advanced unidirectional (UD) structures. The Kevlar® XD S002 semi-finished product is a bidirectional ballistic material with superior performance compared to standard 4-ply UD aramid fabrics, making it ideal for lighter, more efficient, and cost-effective protective vests.Composed of four layers oriented 0°/90°/0°/90° and supplied in roll form, this product allows combination with other materials to obtain soft ballistic solutions with an excellent balance of reduced weight, advanced protection, and lower costs. Its performance depends on the correct alignment of the layers. To maintain quality, it is essential to avoid storage at temperatures above 60 °C and exposure to UV radiation [112].

Table 4.3. Specifications of the Kevlar® XD S002 fabric roll [112]

Areal Density [g/m^2]	Width [cm]	Length [m]
232	160	150

Dyneema® SB21 prepreg

Dyneema® SB21 is a unidirectional (UD) semi-finished material intended for flexible ballistic structures. The manufacturing process of the semi-finished product (Fig. 4.9) begins with the production of polyethylene fiber. A gel-spinning process is used, in which polyethylene is dissolved in a solvent and extruded into highly aligned filaments. The resulting fibers exhibit high crystallinity and a high elastic modulus, providing excellent tensile strength. The polyethylene filaments are arranged parallel in a single layer, without weaving. A thermoplastic elastomer-based matrix is applied to bind and stabilize the fibers [21].

Table 4.4. Dyneema® SB21 material specifications [16], [113]

Areal Density [g/m^2]	Thickness [mm]
140-150	0,15

4.2. New design configurations for personal ballistic protection structures

The manufacturing process of the structures consisted of measuring and marking the specimens, cutting the material using a specialized cutting machine, and forming ballistic assemblies by stitching the layers with dimensions of 300 mm × 300 mm, corresponding to an area of 0.09 m². This places the assemblies produced for this study within the NIJ-C-1 template type (0.09 m²) for small surfaces, in accordance with NIJ 0101.06/2008 [116]. The assemblies were secured by stitching along all sides at 8–10 mm from the edges to maintain layer integrity and alignment. For this process, a Juki LU-563 sewing machine and Nomex® aramid fiber technical thread, type Nc-tech, with a linear density of 40 tex/70, were used.

- **Stage I of the study**

The first part of the study focused on the fabrication of ballistic structures made of Twaron T730, with variations in the number of layers. Following the cutting process, the layers were arranged into three types of assemblies according to the number of layers. These three configurations create a scalable range for comparison, allowing observation of how additional layers influence energy absorption, impact resistance, and failure modes.

The fabricated structures are presented in Figure 4.3.

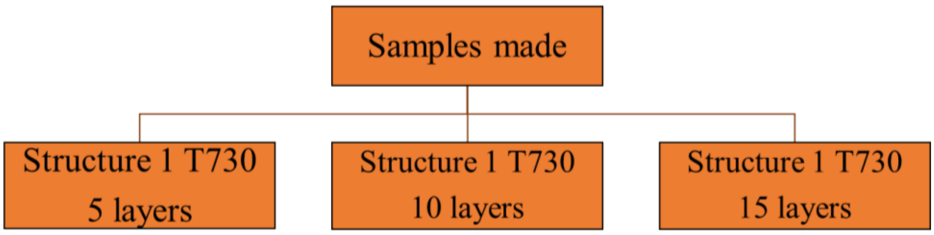

Fig. 4.3. Single-fabric panels

- **Stage II of the study**

Five types of structures were fabricated: four hybrid configurations, with four specimens produced for each architecture, and one reference structure composed solely of 20 layers of Twaron T730.

Since the 15-layer T730 panels from the first stage of the testing campaign exhibited a high backface deformation (BFD), close to the allowable limit (44 mm [116]) for .357 SIG ammunition, the reference panel for Stage II of the study was designed with 20 layers of T730.

4.3. Experimental campaign on the manufactured structures

The single-material panels were manufactured from a single type of fabric/semi-finished material, namely Twaron T730, with the number of layers as the variable parameter. Three types of layered structures were produced to be tested with two calibers, 9 mm and .357 SIG, and one layered structure was produced to be tested with the .357 SIG caliber.

Table 4.5. Developed ballistic structures

Architecture	Orientation	Material	Number of layers	Calculated mass [g]	Areal Density [kg/m^2]	Coding
Architecture 1	impact face ↓ back face	Twaron T730	20	480	5,33	20T
Architecture 2	impact face ↓ back face	Twaron T730	7	440	4,88	7T5D8T
		Dyneema® SB21	5			
		Twaron T730	8			
Architecture 3	impact face ↓ back face	Twaron T730	8	400	4,44	8T2D7T
		Dyneema® SB21	2			
		Twaron T730	7			
Architecture 4	impact face ↓ back face	Twaron T730	15	460	5,11	15T4XD
		Kevlar® XD S002	4			
Architecture 5	impact face ↓ back face	Kevlar® EXO™ CoreMatrix™ CM E1100H	1	440	4,88	1EXO15T
		Twaron T730	15			

The hybrid panels were manufactured from combinations of semi-finished materials arranged in multilayer configurations. Four hybrid multilayer structures were produced for testing with .357 SIG ammunition.

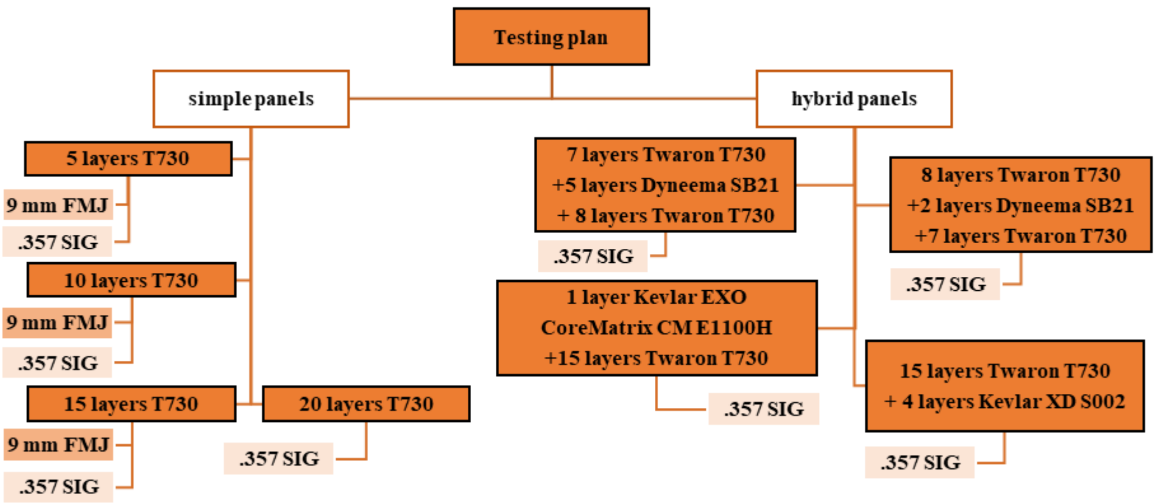

Fig. 4.4. Experimental plan for evaluating the ballistic performance of the developed panels

CHAPTER 5

EXPERIMENTAL EVALUATION OF THE DESIGNED PANELS UNDER BALLISTIC IMPACT

5.1. Standardization in the field of ballistic protection

Through an iterative development process of individual protection systems, the obtained results can be applied by end users, economic organizations, and governmental institutions which, by the nature of their activities, require high-performance, lightweight, and cost-efficient ballistic protection systems [68].

Standards and testing methods are indispensable for validating ballistic protection, as the performance of such equipment cannot be assessed visually. Under real impact conditions, materials are subjected to dynamic loads that differ from static ones; therefore, accurate evaluation is achieved through ballistic or explosive testing conducted under conditions as close to reality as possible [15].

5.2. Ballistic impact testing methodology

The experimental testing program was carried out in two stages.

Stage I aimed to evaluate the behavior of the ballistic protection structures developed in the first part of the study under the action of 9 mm FMJ and .357 SIG FMJ projectiles, through live-fire testing and partial verification of compliance with the Ballistic Resistance of Body Armor, NIJ Standard-0101.06 [116], U.S. Department of Justice, Office of Justice Programs, National Institute of Justice, 2008. The partial nature of compliance arises from the fact that achieving a specific protection level requires testing with two calibers prescribed for that level. In the case of NIJ 0101.06, the ammunition used corresponds to protection Level II (9 mm FMJ) and Level IIIA (.357 SIG FMJ). Under NIJ 0101.07 [117], the ammunition used corresponds to protection level NIJ HG1, with the exception that the standard specifies .357 Magnum JSP ammunition, whereas .357 SIG FMJ was used in the experimental tests.

Stage II aimed to evaluate the behavior of the ballistic protection structures developed through the hybridization of the base structure under the impact of .357 SIG FMJ projectiles, through live-fire testing. The 9 mm FMJ ammunition was excluded because the identified baseline ballistic structure demonstrated favorable performance under impact with 9 mm FMJ projectiles.

Due to financial constraints, the evaluation of ballistic protection system performance is frequently based on statistical approaches, employing a limited number of experimental shots. In the early phases of the study, the research was further affected by the difficulty of procuring domain-specific materials, considered strategic resources in the context of recent tensions and conflicts in the Middle East and Eastern Europe. Consequently, testing was conducted under strictly controlled conditions and with limited resources, reflecting both logistical challenges and the current geopolitical context.

Stage I

The tests were structured into two categories, as follows:

- characterization of the ballistic resistance of structures made entirely of Twaron T730 fabric with a defined number of layers—5 layers, 10 layers, and 15 layers—by testing under the impact of 9 mm FMJ projectiles;
- characterization of the ballistic resistance of structures made entirely of Twaron T730 fabric (5, 10, and 15 layers) by testing under the impact of .357 SIG FMJ projectiles.

The tests were conducted as follows:

- for the 300 mm × 300 mm assemblies, three shots were fired per assembly, centrally arranged in an equilateral triangle with a side length of 120 mm; two assemblies were tested for the thinner panels and eight assemblies for the configuration with the highest number of Twaron T730 fabric layers (15), as follows:
- Twaron T730 structure with 5 layers – 2 assemblies – 2 calibers;
- Twaron T730 structure with 10 layers – 2 assemblies – 2 calibers;
- Twaron T730 structure with 15 layers – 8 assemblies – 2 calibers.

Stage II

For .357 SIG FMJ ammunition, the tests were structured into five categories, as follows:

- characterization of the ballistic resistance of architecture 20T;
- characterization of the ballistic resistance of architecture 7T5D8T;
- characterization of the ballistic resistance of architecture 8T2D7T;
- characterization of the ballistic resistance of architecture 15T4XD;
- characterization of the ballistic resistance of architecture 1EXO15T.,

The tests were conducted as follows:

- for the 300 mm × 300 mm assemblies, three shots were fired per assembly, with four assemblies tested for each configuration; the number of tested assemblies was as follows:
- architecture 20T – 4 assemblies – 1 caliber;
- architecture 7T5D8T – 4 assemblies;
- architecture 8T2D7T – 4 assemblies;
- architecture 15T4XD – 4 assemblies;
- architecture 1EXO15T – 4 assemblies.

The testing campaign was carried out with the support of the " Research and Innovation Center for CBRN Defense and Ecology" Bucharest, within the Individual Ballistic Protection Equipment Laboratory.

Test equipment used in the experimental program

The ballistic testing activities were conducted using the following basic equipment:

- the firing bench, consisting of a support mounted on a metal platform rigidly fixed to the ground, a ballistic barrel of the required caliber, and a laser aiming system,
- the velocity measurement system, a chronograph consisting of two detection zones based on optical sensors, positioned 1 m apart, which measure the time required for the projectile to travel the distance between the sensors, thereby determining the projectile

velocity. A B472 Precision Light Screen chronograph manufactured by HPI GmbH, with a velocity range of 30–3000 m/s, was used [118].

- the specimen mounting fixture with clay backing material. The box intended for the backing material has base dimensions of 610 mm per side and a height of 140 mm. The rear panel shall be removable and constructed of wood or plywood with a thickness of 19.1 mm. In accordance with NIJ specifications, the prescribed clay type is Roma Plastilina No. 1. The material shall be homogeneous, free of internal voids, and the exposed surface shall be smooth and capable of being readily leveled.
- the depth measurement device — a depth gauge (depth caliper) with a measurement accuracy of ± 0.1 mm,
- a climatic chamber for conditioning the specimens at 20 ± 5 °C,
- a drying oven for ammunition conditioning,
- a thermo-hygrometer with a measurement accuracy of ±1 unit.

In addition to the basic equipment, a high-speed camera was also used, positioned diagonally or in front of the specimen. The high-speed camera was a Photron Fastcam SA-Z model. A Tamron AF-S SP 70–200 mm f/2.8 lens was used [119].

For high-speed imaging, the following camera settings were employed: acquisition rate of 20,000 frames per second; exposure time 1/48; resolution 1024 × 1024 pixels.

Backing material/ Clay backing material

For proper use in ballistic testing, the plasticine shall have a smooth, homogeneous, and readily levelable surface, free of voids or defects.

Test range ambient conditions:

- temperature: 21±5˚C;
- relative humidity: within the range of 30-70%;
- atmospheric pressure: 764 ± 15 mm Hg.

The testing conditions observed for the evaluation of the ballistic panels were those specified in NIJ Standard 0101.06 [116]. In preparation for testing protective systems, the equipment and configuration must follow specific instructions to ensure consistent and accurate results (Figure 5.1). The protective panel is mounted at a distance of 5 m from the muzzle of the ballistic barrel, and the barrel must be aligned perpendicular to the specimen surface, both in the vertical and horizontal planes [116].

The weapon system used consisted of a 9 mm caliber ballistic barrel, with a firing distance of 5 m. Measurement of the backface deformation (BFD) of the assembly is performed in ballistic clay backing, in accordance with NIJ 0101.06/2008 [116].

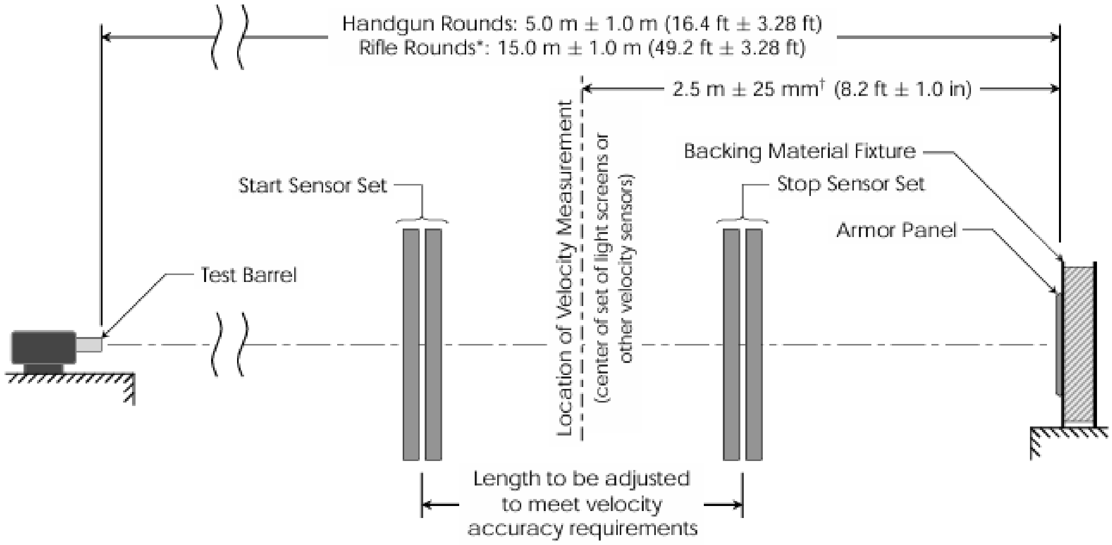

Fig. 5.1. Specimen placement relative to the firing device [116]

5.3. Evaluation of impact performance for Stage I of the study based on experimental results

The first part of the study focused on the fabrication of ballistic structures made of Twaron T730, with the number of layers as the variable parameter. Six structures were produced to be tested with two calibers, 9 mm and .357 SIG [71].

Table 5.1. Calculated mass of Twaron T730 structures

Material	Number of layers	No. of structures	Calculated mass [g]	Areal density [kg/m^2]
Twaron T730	5	2	120	1,33
	10	2	220	2,44
	15	2	360	4,00

Ballistic impact response of a 15-layer Twaron T730 assembly to 9 mm FMJ ammunition

Table 5.2. Ballistic test results for the 15-layer T730 panel [71]

Shot No.	Specimen	Measured velocity (m/s)	Resulting penetration	BFD (mm)
1	15-layer T730 stitched on all four sides (Specimen 1)	370	PP	36
2		376	PP	35
3		372	PP	36

PP – partial penetration

Figure 5.2 presents frames extracted from the high-speed camera recording, highlighting the behavior of the protective structure under impact from a 9 mm projectile.

The impact sequence on the specimen reveals five distinct stages of deformation. Initially, the projectile generates a localized deformation in the contact area. This is followed by the formation of a ballistic cone on the opposite side, as stress waves propagate radially. The affected zone expands, and the fabric exhibits undulations and ridges. During the stage of maximum deformation, energy is dissipated and the projectile is decelerated. Finally, the fabric stabilizes, retaining a significant residual deformation.

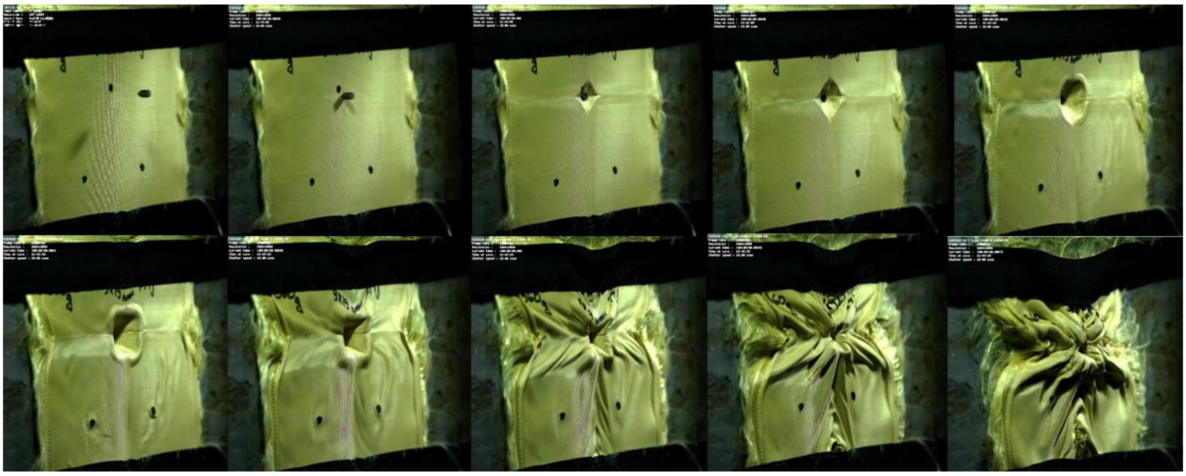

Fig. 5.2. Impact 1 on the 15-layer T730 panel. Moments during the impact of the 9 mm FMJ projectile captured with a high-speed camera at 20,000 frames per second

To determine whether the panel provides sufficient protection, the depth of the indentation in the clay backing, resulting from panel deformation during impact, must be measured and examined (Fig. 5.3a). The standard requirements presented in Section 7.8.8 of NIJ Standard 0101.06/2008 state that all measured backface deformation (BFD) depths shall be 44 mm or less [116].

The structural response of the 15-layer T730 specimen can be considered adequate, as the deformations formed in the ballistic clay backing, illustrated in Figures 5.3b–c, exhibit similar dimensions and morphologies, indicating a uniform distribution of impact energy and a consistent structural response.

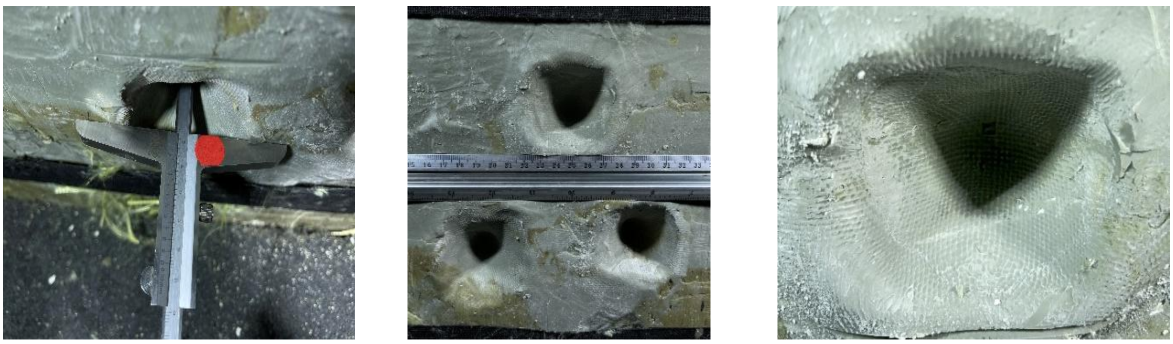

a) b) c)

Fig. 5.3. Front view of the backing material after impact of the 15-layer T730 specimen with a 9 mm projectile: (a) measurement of deformation in ballistic clay backing, in accordance with NIJ 0101.06/2008; (b) view of the three successive impacts; (c) detail of a deformation in the backing material [71]

Figure 5.4 presents the front and rear views of the ballistic protection panel composed of 15 layers of Twaron T730 after testing. The impact zones on the front face and the corresponding deformation imprints on the rear face can be observed, with no complete penetration of the panel.

a) b)

Fig. 5.4. Strike face (a) and back face (b) of the 15-layer Twaron T730 protection system after 9 mm FMJ impact

Figure 5.5 highlights, through local magnifications, the impact zones corresponding to the three shots observed in Figure 5.4 for the panel composed of 15 layers of Twaron T730. Local deformation of the fabric can be observed, along with fiber breakage and elongation in the central impact area, as well as load redistribution to adjacent fibers, without the occurrence of complete penetration. This confirms the predominant energy absorption mechanism through fiber stretching and progressive damage.

a) shot 1 b) shot 2 c) shot 3

Fig. 5.5. mpact detail images for the 15-layer T730 panel tested with 9 mm FMJ ammunition

After completion of the testing campaign, in the case of specimens that retained the projectile, they were disassembled layer by layer to determine the layer at which the projectile was stopped. As shown in Figure 5.6, the protection system composed of 15 layers of aramid fabric T730 successfully stopped the projectile from the first shot in the 4th layer, in the 5th layer for Shot 2, and in the 3rd layer for Shot 3.

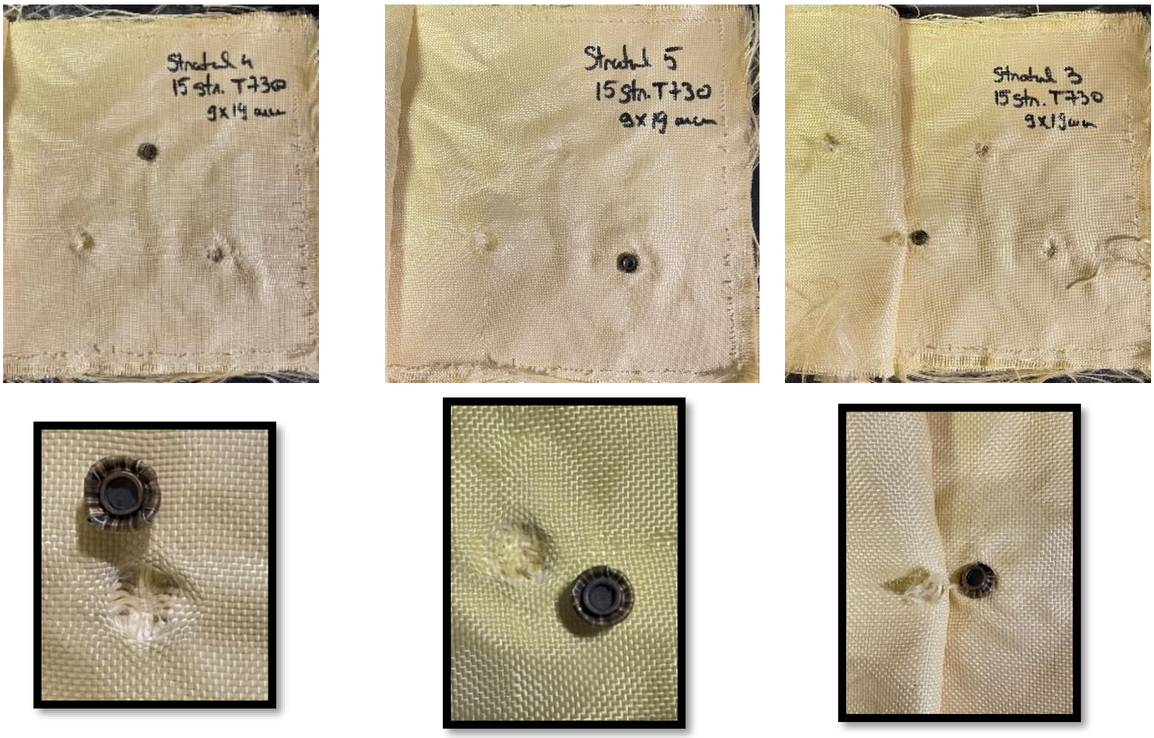

a) shot 1, $V_0 = 370$ m/s b) shot 2, $V_0 = 376$ m/s c) shot 3, $V_0 = 372$ m/s

Fig. 5.6. Layers in which the projectiles were stopped in the 15-layer T730 panel

Determination of resistance to .357 SIG projectile impact for a 15-layer Twaron T730 ballistic assembly

Ammunition: .357 SIG caliber cartridge, FMJ projectile.

Weapon system: .357 SIG caliber test barrel.

Firing distance: 5 m.

Measurement of the backface deformation (BFD) of the assembly is performed in ballistic clay backing, in accordance with NIJ 0101.06/2008 [116].

It can be observed from Table 5.8 that, for the second impact, the BFD was equal to the maximum allowable limit specified in NIJ 0101.06, while the third impact resulted in complete penetration, which is not recommended and effectively precludes the use of the panel when the threats are of the .357 SIG type.

Table 5.3. Ballistic test results for the 15-layer T730 panel

Shot No.	Specimen	Measured velocity (m/s)	Resulting penetration	Backface deformation (mm)
1	15-layer T730 stitched on all four sides (Specimen 1)	445	PP	40
2		447	PP	44
3		447	CP*	-

**CP – complete penetration*

Figure 5.7 presents frames extracted from the high-speed camera recording, highlighting the behavior of the protective structure composed of 15 layers of Twaron T730 under impact from a .357 SIG projectile.

The impact sequence highlights distinct stages of deformation: initial localized deformation, radial propagation of stress waves, and formation of the ballistic cone on the rear face, followed by the expansion of the affected area and the appearance of wrinkles/ridges in the fabric. For impacts 1 and 2, the energy is dissipated through fiber stretching and progressive damage, and the projectile is stopped, leaving a residual deformation. In the case of impact 3, the accumulation of damage reduces the energy absorption capacity, leading to local structural failure and complete perforation.

Fig. 5.7. High-speed image sequence of .357 SIG impact on the 15-layer T730 specimen (20,000 fps) — Shot 1, moment of impact

Figure 5.8 presents the front and rear views of the ballistic protection panel composed of 15 layers of Twaron T730 after testing. The impact zones on the front face, the corresponding deformation imprints on the rear face, and the complete penetration of the panel in Shot 3 can be observed. The lower-right impact is distinguished by total perforation, characterized by the formation of a through-hole in the backing material, while the other two impacts produced only localized plastic deformations, indicating partial but effective absorption of the impact energy.

a) b) c)

Fig. 5.8. Front (a) and rear (b) views of the protection system composed of 15 layers of Twaron T730 after testing with a .357 SIG projectile; (c) deformations in the backing material from the three shots performed on the specimen, highlighting the complete penetration

Figure 5.9 highlights the position of the shot that completely penetrated the assembly, although the velocity variation is very small compared to the other shots (see Table 5.3).

All structures composed of 5 and 10 layers of Twaron T730, tested under impact with 9 mm and .357 SIG ammunition, were completely penetrated by each shot for both calibers.

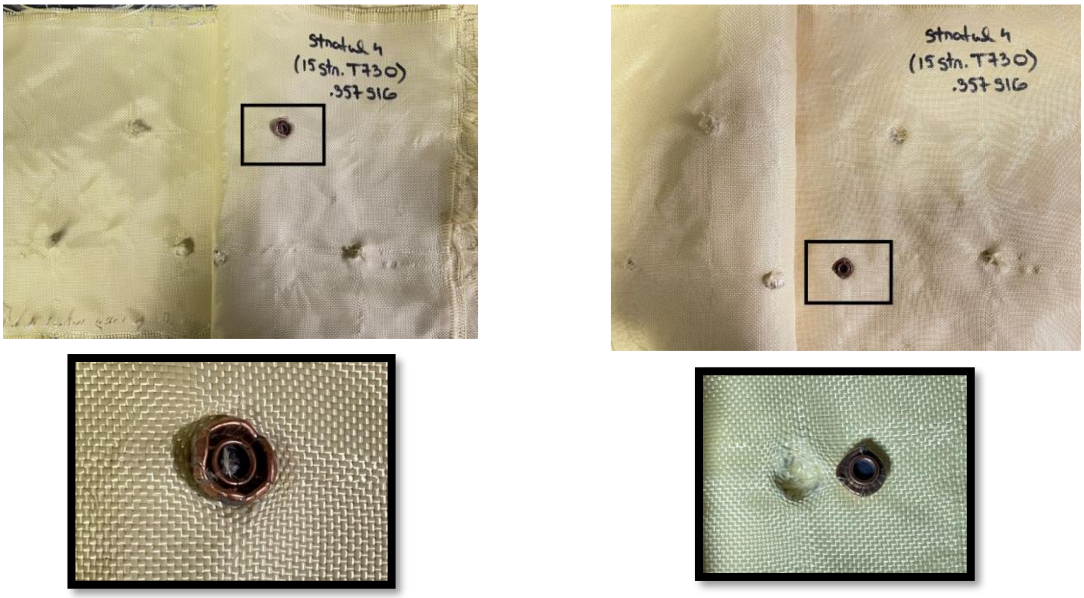

a) shot 1, $V_0 = 445$ m/s   b) shot 2, $V_0 = 447$ m/s

Fig. 5.9. Layers at which the projectiles were arrested in the 15-layer Twaron T730 panel

Stage I conclusions

Following the tests performed on the ballistic panels, in which three shots were fired at each panel, the results show that two of the panels experienced partial penetration:

• the panel composed of 15 layers of T730 fabric tested under 9 mm FMJ impact withstood all three shots;

• the panel composed of 15 layers of T730 fabric tested under .357 SIG impact withstood two shots, while complete penetration occurred on the third shot.

These results indicate that the two panels demonstrated a satisfactory ballistic protection capability against 9 mm FMJ projectiles and were able to stop the projectiles before complete penetration of the panel occurred. These findings highlight the effectiveness of the panels in providing protection against the ballistic impact of 9 mm FMJ projectiles and suggest that they may be suitable for various protective applications.

To obtain statistical confidence regarding the structure's ability to stop both types of projectiles, further validation is required. In this regard, additional testing of the structure is necessary. Thus, in the first phase of Stage II of the study, three structures composed of 15 layers of Twaron T730 will be tested for each caliber: 9 mm and .357 SIG.

5.4. Evaluation of impact performance for the second stage of the study – experimental results

Statistical validation for the 15-layer Twaron T730 structure tested with two calibers

For the statistical validation of the 15-layer Twaron T730 structure, six additional specimens were produced: three for testing with 9 mm ammunition and three for testing with .357 SIG ammunition.

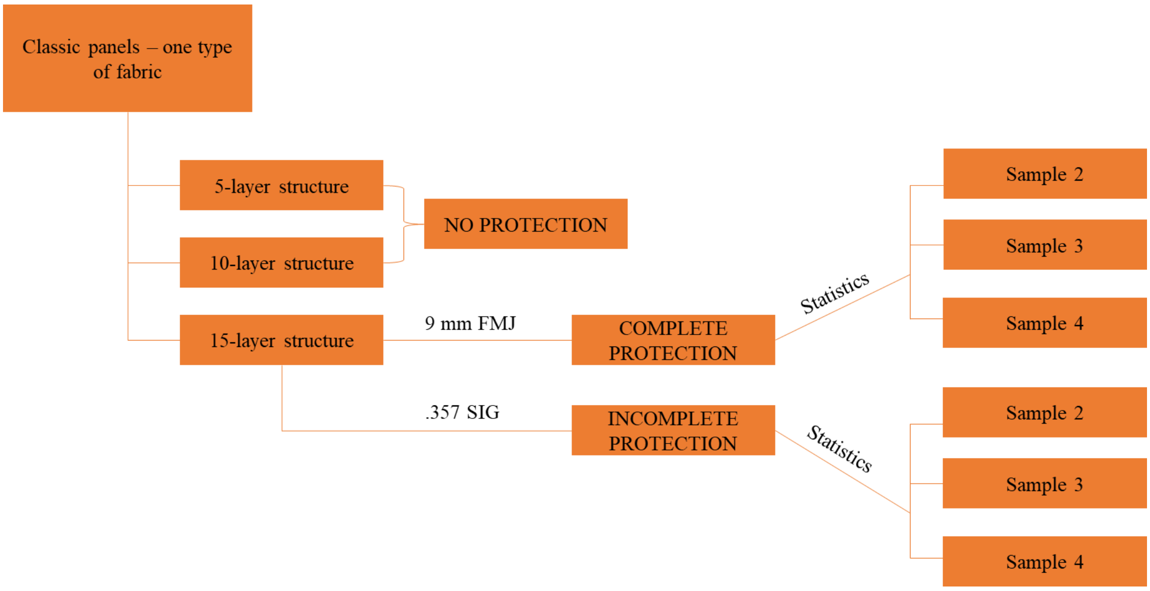

Fig. 5.10. Experimental campaign scheme for validation of Twaron T730 structures

Evaluation of ballistic resistance of the 15-layer Twaron T730 structure under 9 mm FMJ impact

Ammunition: 9×19 mm Luger cartridge, FMJ (full metal jacket) projectile.

Weapon system: 9 mm caliber test barrel.

Firing distance: 5 m.

Measurement of the backface deformation (BFD) of the assembly is performed in ballistic clay backing, in accordance with NIJ 0101.06/2008 [116].

For the 12 projectile velocity measurements presented in Table 5.4, the following were determined: mean velocity – 367.33 m/s; standard deviation – 5.38 m/s, representing only 1.46% of the mean velocity; maximum value – 376 m/s; minimum value – 355 m/s.

The obtained values indicate good repeatability of the ballistic response, with backface signatures in the backing material remaining below the allowable limit specified by NIJ Standard 0101.06 [116] and the NIJ 0101.07 edition [117], confirming the structure’s ability to effectively absorb impact energy.

Table 5.4. Experimental results

Specimen	Shot No.	Measured velocity (m/s)	Resulting penetration	BFD (mm)
15-layer T730 Specimen 1 (Table 5.2)	1	370	PP	36
	2	376	PP	35
	3	372	PP	36
15-layer T730 Specimen 2	1	355	PP	36
	2	371	PP	38
	3	368	PP	37
15-layer T730 Specimen 3	1	366	PP	37
	2	368	PP	41
	3	369	PP	40
15-layer T730 Specimen 4	1	361	PP	37
	2	366	PP	42
	3	366	PP	40

Evaluation of ballistic resistance of the 15-layer Twaron T730 structure under .357 SIG impact

For the 12 projectile velocity measurements presented in Table 5.5, the following were determined: mean velocity – 440 m/s; standard deviation – 4.30 m/s, representing only 0.97% of the mean velocity; maximum value – 447 m/s; minimum value – 435 m/s.

Table 5.5. Experimental results

Specimen	Shot No.	Measured velocity (m/s)	Resulting penetration	BFD (mm)
15-layer T730 Specimen 1 (Table 5.3)	1	445	PP	40
	2	447	PP	44
	3	447	CP	-
15-layer T730 Specimen 2	1	441	PP	**54**
	2	435	PP	**50**
	3	440	PP	**68**
15-layer T730 Specimen 3	1	436	CP	-
	2	437	PP	**55**
	3	440	PP	**47**
15-layer T730 Specimen 4	1	438	CP	-
	2	435	PP	41
	3	439	CP	-

For the .357 SIG caliber, a greater dispersion of BFD values is observed compared to the 9 mm caliber, with some values exceeding the 44 mm threshold that represents the allowable limit specified by NIJ Standard 0101.06, indicating that the structure is operating near its maximum performance limit.

Statistical analysis shows that the 15-layer Twaron T730 panel provides adequate protection against 9 mm FMJ projectiles, with BFD values meeting the standard requirements (≤ 44 mm, with an absolute limit of 50 mm). However, for .357 SIG, the structure does not ensure adequate protection: even the specimen without complete penetration recorded BFD values exceeding 50 mm, indicating insufficient trauma attenuation.

In order to obtain a ballistic structure capable of providing simultaneous protection against both types of threats, the author proposes the development of hybrid architectures, using as a starting point the structure composed of 15 layers of Twaron T730. Considering the demonstrated effectiveness of this configuration against 9 mm FMJ projectiles, the author decided that the testing of hybrid structures would focus exclusively on .357 SIG ammunition, in order to assess the potential for improving ballistic performance in this context within the scope of the present study, while the reference panel was defined as a structure composed of 20 layers of Twaron T730.

Five types of structures were produced, four of which were hybrid, with four specimens fabricated for each architecture. The developed structures are presented in Table 5.6.

Table 5.6. Hybrid ballistic structures for .357 SIG testing

Architecture	Orientation	Material	Number of layers	Calculated mass [g]	Areal Density [kg/m²]	Coding
Architecture 1 (reference)	impact face ↓ back face	Twaron® T730	20	480	5,33	20T
Hybrid arhitecture						
Architecture 2	impact face ↓ back face	Twaron® T730	7	440	4,88	7T5D8T
		Dyneema® SB21	5			
		Twaron® T730	8			
Architecture 3	impact face ↓ back face	Twaron® T730	8	400	4,44	8T2D7T
		Dyneema® SB21	2			
		Twaron T730	7			
Architecture 4	impact face ↓ back face	Twaron® T730	15	460	5,11	15T4XD
		Kevlar® XD S002	4			
Architecture 5	impact face ↓ back face	Kevlar® EXO™ CoreMatrix™ CM E1100H	1	440	4,88	1EXO15T
		Twaron® T730	15			

The hybrid panels exhibit a lower mass compared to the monomaterial panel, relative to the number of additional layers and the total mass. Among the analyzed configurations, Architecture 5 demonstrates the best efficiency-to-mass ratio, while Architecture 3 stands out with the lowest mass.

For each structure, four identical specimens were fabricated and ballistically tested using .357 SIG projectiles, with each specimen subjected to three impacts. Subsequently, the panels were disassembled layer by layer to determine the penetration depth and the layers responsible for stopping the projectiles in cases without complete penetration, while also enabling projectile recovery for further analysis.

This summary highlights and analyzes the structures that demonstrated the highest ballistic performance, selected based on the experimental results and the efficiency criteria established within the study.

Determination of resistance to .357 SIG projectile impact for the 7T5D8T architecture

Ammunition: .357 SIG caliber cartridge, FMJ projectile.

Weapon system: .357 SIG caliber test barrel.

Firing distance: 5 m.

Measurement of the backface deformation (BFD) of the assembly is performed in ballistic clay backing, in accordance with NIJ 0101.06/2008 [116].

Table 5.7. Experimental results for the 7T5D8T architecture

Specimen	Shot No.	Measured velocity (m/s)	Resulting penetration	BFD (mm)	Layer at which the projectile was stopped
7T5D8T Specimen 1	1	442	PP	31	S5
	2	442	PP	35	S5
	3	443	PP	32	S3
7T5D8T Specimen 2	1	449	PP	26	S7/7
	2	448	PP	33	S4/7
	3	451	PP	26	S6/7
7T5D8T Specimen 3	1	453	PP	34	S5/7
	2	452	PP	29	S7/7
	3	452	PP	28	S7/7
7T5D8T Specimen 4	1	450	PP	32	S7/7
	2	449	PP	27	S7/7
	3	450	PP	31	S7/7

The BFD values fall within an approximate range of 26–35 mm, with an arithmetic mean of ~30.3 mm, well below the 44 mm reference limit imposed by NIJ Standard 0101.06 [116], while the impact velocities are consistent (442–453 m/s). These results indicate efficient energy absorption and confirm the superior performance of the hybrid architecture, with the contribution of the Dyneema layers being essential in reducing rear-face deformation.

Detailed images of each layer for a representative specimen are presented in Figures 5.11–5.16. To identify the layer that stopped the projectile, the ballistic package is carefully opened along three sides, and the layers are examined sequentially to determine the point at which they begin to separate easily. This point marks the penetration limit of the projectile: the upper layers are perforated or damaged, while the lower layers remain intact or only deformed. Since separation affects the integrity of the package, photographic documentation is performed in reverse order, from the last layer to the first, following exactly the sequence of analysis.

Figure 5.11 shows that layer 7 of the set of 8 Twaron T730 layers positioned on the rear side of the 7T5D8T architecture is the last layer in which one of the three impacts was stopped, while only impact marks are visible on layer 8/8 (Fig. 5.11a). On the first Dyneema layer, the marks left by the impacts can be observed, but without rupture or damage to the layer.

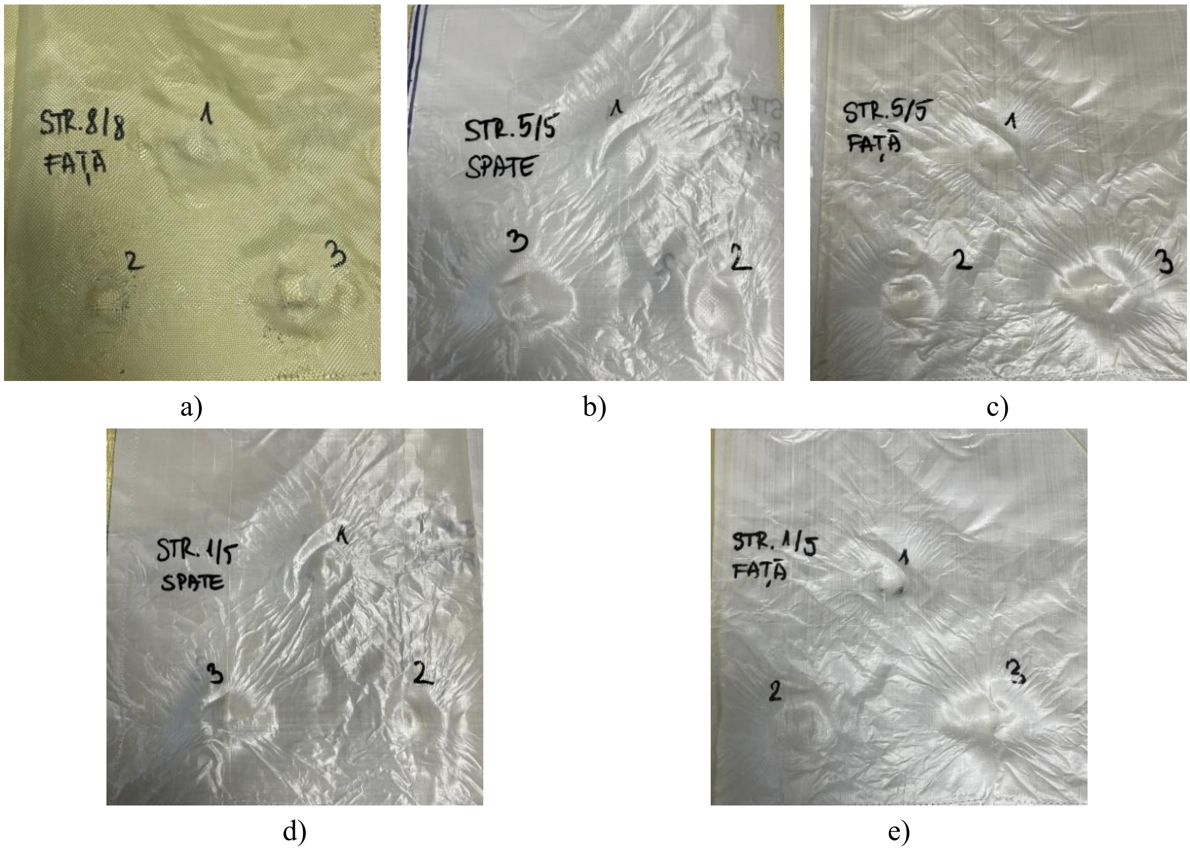

Fig. 5.11. Images of the constituent layers. Layer 8 of the set of 8 Twaron T730 layers positioned on the rear side of the 7T5D8T architecture (a); Layers 5–1 of the set of 5 Dyneema layers positioned within the 7T5D8T architecture (b–e).

Figure 5.12 illustrates the examination of layers 7–6 from the set of 7 Twaron T730 layers positioned on the impact face of the 7T5D8T hybrid architecture. The overview images (front and rear) highlight the positions of the three shots, while the a–c markings enable correlation with the enlarged photographic details in the lower part of the figure. For Shot 1, it can be observed that the projectile was stopped at the surface of layer 7, as confirmed by the corresponding photographic detail (projectile 1 – layer 7, rear), where the projectile is visible at the fabric level, partially embedded and surrounded by deformed fibers. This observation indicates efficient energy absorption in the front layers, without significant propagation of damage to the subsequent layers.

In the case of Shot 3, layer 6 is the layer that captured the projectile; however, the resulting damage is limited. The photographic details show clear signs of localized compression caused by the impact, without rupture or cutting of the Twaron yarns, suggesting that the residual energy of the projectile had already been considerably reduced before reaching this level. Overall, the images confirm the essential role of layers 6–7 in the final stage of projectile arrest and highlight the efficiency of progressive energy dissipation mechanisms within the multilayer structure.

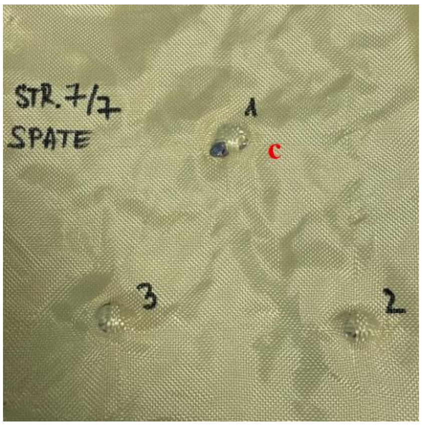

a)

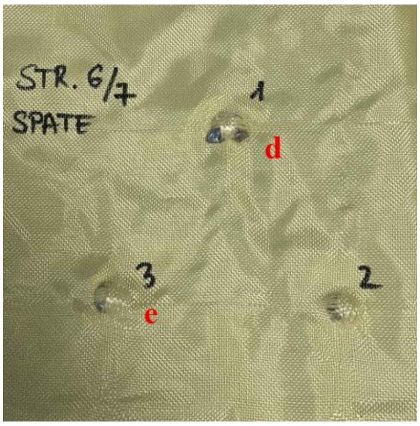

b)

Layers 7–6 of the set of 7 Twaron T730 layers positioned on the impact face of the 7T5D8T architecture

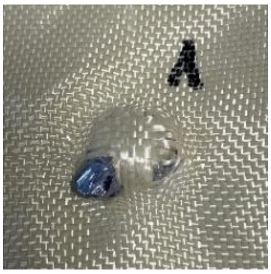

c)

d)

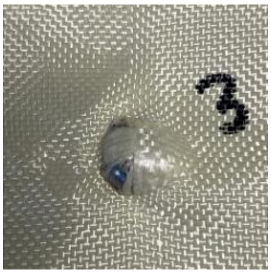

e)

Fig. 5.12. Sequential examination of the constituent layers of the panel tested with a .357 SIG projectile, showing the layers that stopped the projectile: (a) layer 7, rear; (b) layer 6, rear; (c) detail of Shot 1, layer 7, rear; (d) detail of Shot 1, layer 6, rear; (e) detail of Shot 3, layer 6, rear.

Figure 5.13 presents the sequential examination of layers 5–4 of the Twaron T730 fabric package, positioned on the impact face of the analyzed architecture, highlighting the interaction of the three shots with the textile structure.

In the case of Shot 2, it can be observed that layer 4 successfully stopped the projectile (Fig. 5.13e). The fibers in the impact area exhibit significant stretching and compaction beneath the projectile, indicating efficient energy dissipation through plastic deformation of the fabric. At the same time, several broken yarns are visible, associated with the oblique positioning of the projectile within the material, which generated localized shear stresses. This orientation also suggests the probable influence of the first shot, which altered the initial state of the fabric and contributed to the observed failure mechanism.

a) b) c)

Layers 5–4 of the set of 7 Twaron T730 layers positioned on the impact face of the 7T5D8T architecture

d) e) f)

Fig. 5.13. Examination of the constituent layers that retained the projectile for the 7T5D8T panel: (a) layer 5, rear; (b) layer 5, front; (c) layer 4, rear; details of the projectile retention zone on the rear of layer 5: (d) Shot 1; (e) Shot 2; (f) Shot 3.

In images d–f of Figure 5.14, the manner in which the fibers are stretched and compacted over the surface of the projectile can be observed, adopting radial and transverse orientations, which indicates a dominant load-bearing mechanism through tensile loading. The positioning of the fibers on the projectile highlights a partial "wrapping" effect, which contributes to increased friction and efficient dissipation of residual energy.

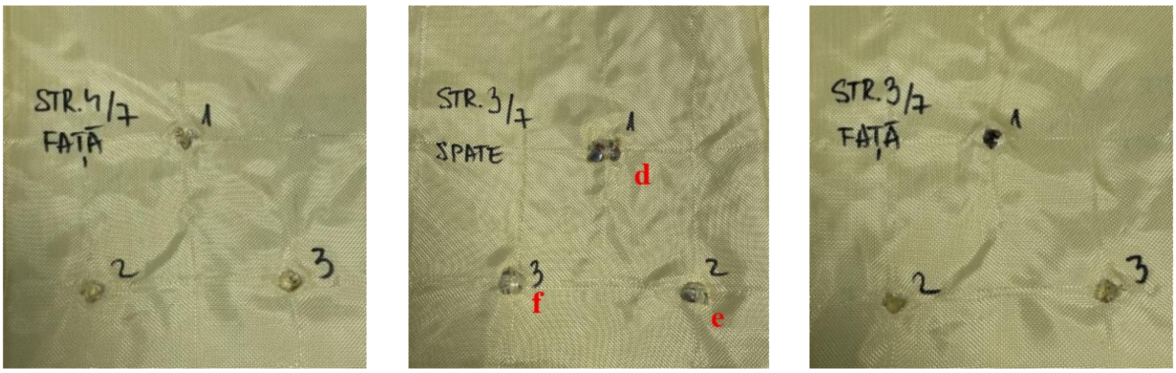

a) b) c)

Layers 4–3 of the set of 7 Twaron T730 layers positioned on the impact face of the 7T5D8T architecture

d) e) f)

Fig. 5.14. Examination of the constituent layers that retained the projectile for the 7T5D8T panel: (a) layer 4, front; (b) layer 3, rear; (c) layer 3, front; details of the projectile retention zone on the rear of layer 3: (d) Shot 1; (e) Shot 2; (f) Shot 3.

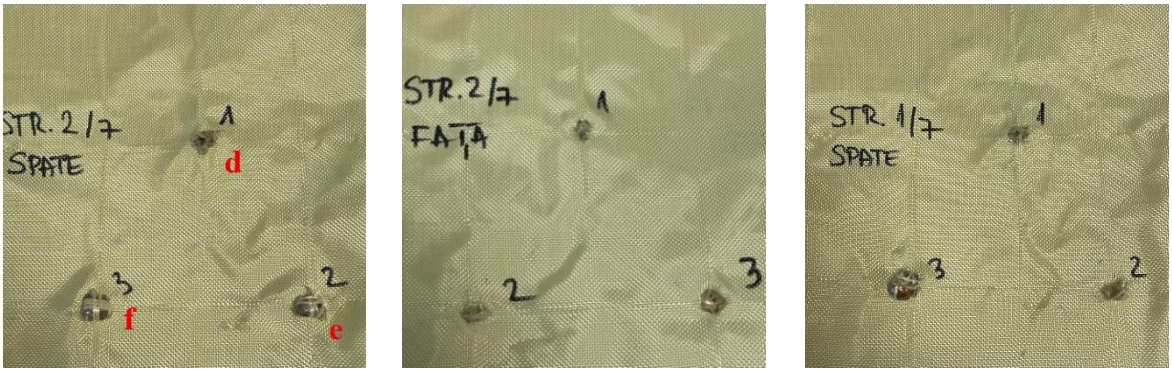

a) b) c)

Layers 2–1 of the set of 7 Twaron T730 layers positioned on the impact face of the 7T5D8T architecture

d) e) f)

Fig. 5.15. Examination of the constituent layers that retained the projectile for the 7T5D8T panel: (a) layer 2, rear; (b) layer 2, front; (c) layer 1, rear; details of the projectile retention zone on the rear of layer 2: (d) Shot 1; (e) Shot 2; (f) Shot 3.

In Figure 5.15, images d–f show the projectile partially visible, while the Twaron fibers exhibit limited local deformation, indicating traversal of the layer with high residual energy.

Figure 5.16 presents details of the impact zones corresponding to layer 1/7 of the Twaron package, positioned on the impact face of the hybrid architecture. In image (a), the positions of the projectiles retained within the structure are highlighted, while image (b) shows the same areas after projectile extraction, revealing well-defined cavities. The enlarged details show fibers strongly compacted and folded around the projectile (e).

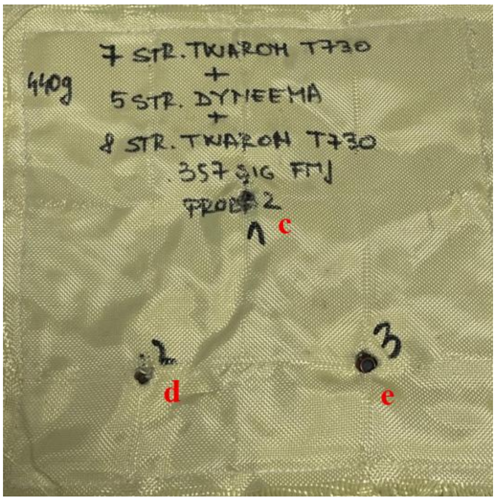

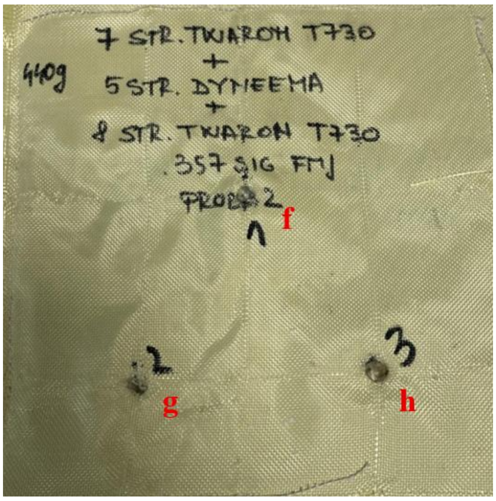

a) b)

Layer 1 of the set of 7 Twaron T730 layers positioned on the impact face of the 7T5D8T architecture, with the projectiles in the package (a) and after projectile extraction (b)

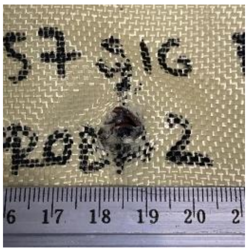

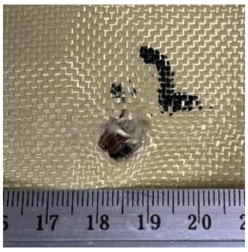

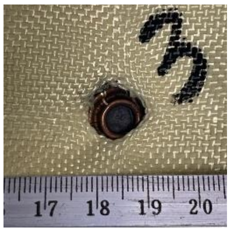

c) d) e)

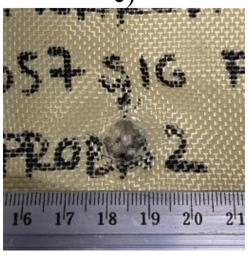

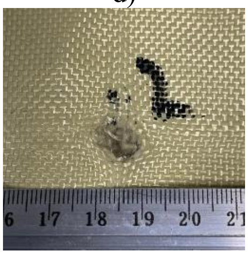

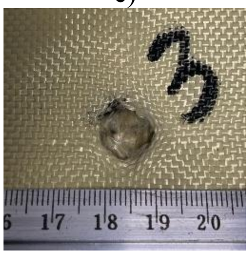

f) g) h)

Fig. 5.16. Examination of the constituent layers that retained the projectile for the 7T5D8T panel: (a) layer 1, front; (b) layer 1, front, after projectile extraction; details of the projectile retention zone on the front face of layer 1: (c) Shot 1; (d) Shot 2; (e) Shot 3; (f) Shot 1 (without projectile); (g) Shot 2 (without projectile); (h) Shot 3 (without projectile).

Figures 5.11–5.16 provide a visual representation of the layers in the package composed of 7 layers of Twaron T730 + 5 layers of Dyneema + 8 layers of Twaron T730 (Specimen 2), shown from both the front and rear perspectives of each layer. Following testing, partial penetration was observed, manifested by damage to the first seven layers of the semi-finished material. The images capture the complete condition of the package after exposure to three projectiles.

In the case of the 7T5D8T structure, the analysis of the experimental results indicates that layer 7 of the set of 7 Twaron T730 layers positioned on the impact face of the 7T5D8T architecture retained 50% of the applied impacts when all 12 shots are considered.

Determination of resistance to .357 SIG projectile impact for the 1EXO15T architecture

Table 5.8 presents the impact characteristics for the 1EXO15T hybrid panel

Tabelul 5.8. Experimental results for the 1EXO15T architecture

Specimen	Shot No.	Measured velocity (m/s)	Resulting penetration	Backface deformation (mm)	Layer at which the projectile was stopped
1EXO15T Specimen 1	1	446	PP	30	S1/1
	2	443	PP	36	S1/1
	3	448	PP	35	S1/1
1EXO15T Specimen 2	1	451	PP	25	S1/1
	2	450	PP	36	S1/1
	3	451	PP	30	S1/1
1EXO15T Specimen 3	1	450	PP	34	S1/1
	2	451	PP	30	S1/1
	3	450	PP	35	S1/1
1EXO15T Specimen 4	1	452	PP	31	S1/1
	2	452	PP	29	S1/1
	3	449	PP	36	S1/1

The BFD values fall within an approximate range of 25–36 mm, with a mean of ~32.3 mm, well below the 44 mm limit imposed by NIJ Standard 0101.06 [116], while the impact velocities vary within a narrow range (443–452 m/s). These results indicate efficient energy absorption and confirm the significant contribution of the Kevlar EXO layer in reducing rear-face deformation without affecting the ballistic stability of the structure.

The images corresponding to each layer of the 1EXO15T structure are presented in Figures 5.17–5.18. The absence of significant damage on the final layer indicates that the projectiles did not traverse a substantial number of layers; the impact energy was dissipated primarily in the upper regions of the architecture. This suggests that the structural integrity of the package remained largely preserved, and the protection provided by the upper layers was effective.

The enlarged details in Figures 5.17a and 5.17b highlight the same entry area in two different states: in the left image (a), the projectile is retained in the fabric, viewed from the front, partially visible and surrounded by strongly stretched and compacted fibers; in the right image (b), the projectile has been extracted, leaving a well-defined cavity that illustrates the redistribution and anchoring of the Twaron fibers during projectile arrest.

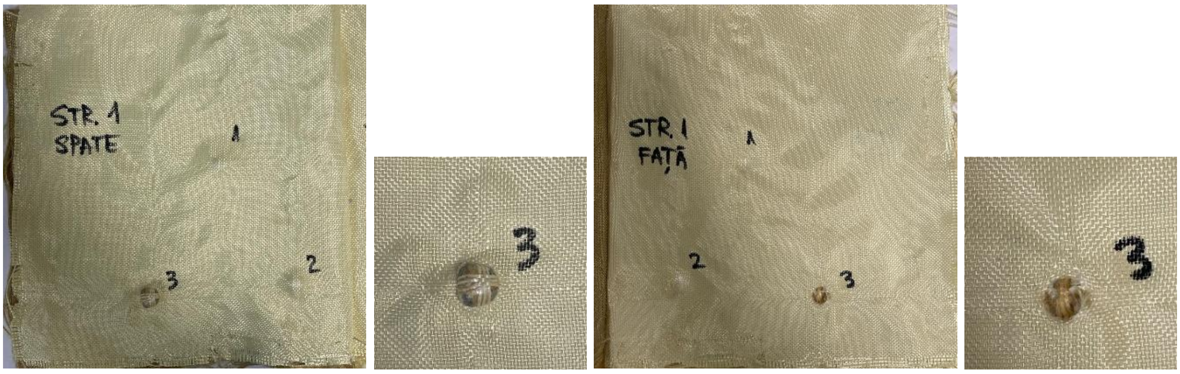

a) b)

Fig. 5.17. Images of layer 1 (EXO fabric) from the 1EXO15T hybrid panel: (a) layer 1, rear, with detail of Shot 3; (b) layer 1, front, with detail of Shot 3.

The images in Figure 5.18 present layer 1 of Kevlar EXO positioned on the impact face of the architecture, tested under .357 SIG ammunition for three distinct shots. For Shots 1 and 2, only local fabric deformations are observed, with no visible penetration, indicating exceptional absorption of residual energy. In the case of Shot 3, the projectile slightly penetrated the layer, as evidenced by the appearance of a well-defined local bulge on the rear face and by the enlarged detail (a), where the projectile is partially visible. The fibers in the impact zone are strongly compacted and stretched around the projectile, suggesting that the Kevlar EXO layer functioned as a final braking layer, limiting penetration and preventing complete perforation despite the cumulative energy of successive impacts.

Figure 5.18b shows a highly efficient projectile capture mechanism, characterized by the “wrapping” of the projectile by Kevlar fibers. The projectile is tightly gripped within the fabric, with visible contact between the fibers and the projectile jacket, while the fibers are strongly compacted and radially folded around the projectile. This anchoring mechanism indicates gradual energy transfer and progressive deceleration, explaining the material’s ability to stop the projectile within a single layer.

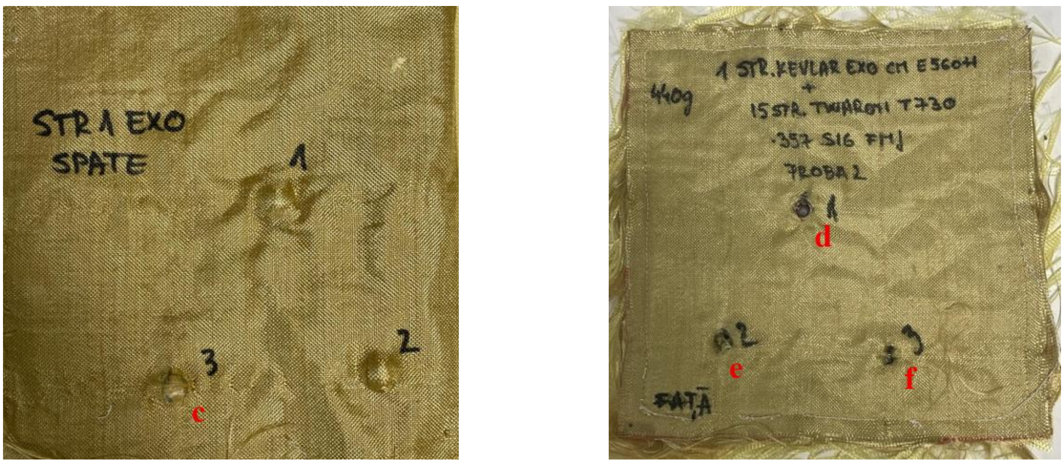

a) b)

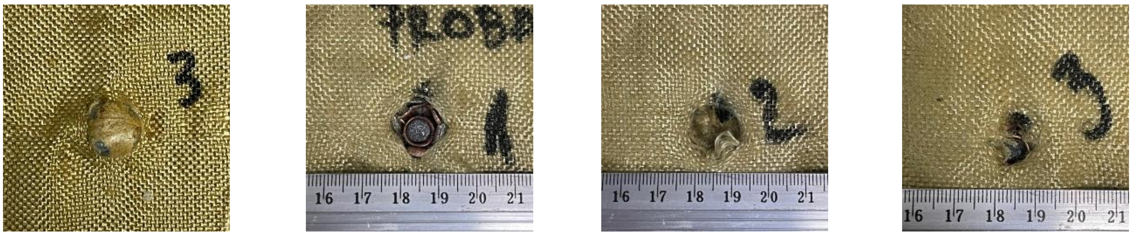

c) d) e) f)

Fig. 5.18. Examination of the EXO layer that retained the projectile for the 1EXO15T730 panel: (a) layer 1, rear; (b) layer 1, front; details of the projectile retention zone on the front face of layer 1: (c) Shot 3, rear; (d) Shot 1; (e) Shot 2; (f) Shot 3, front.

The Kevlar EXO layer demonstrated exceptional ballistic performance, successfully stopping .357 SIG projectiles within a single layer without complete penetration, even under repeated impact conditions. This performance highlights the material's high capacity to absorb and dissipate kinetic energy through efficient mechanisms of fiber deformation and anchoring.

Upper tolerance limit calculation in accordance with NIJ 0101.07

When any BFD measurement exceeds 44.0 mm, there must be 95% confidence that 80% of all BFD depths will be 44.0 mm or less. This requirement may be verified using a statistical tolerance limit. It is expected that a stated proportion of the entire population of BFD measurements will fall at or below the upper statistical tolerance limit. To achieve this, the population of BFD measurements is assumed to be normally distributed, and the upper tolerance limit, BFD_U, must be ≤ 44.0 mm. The upper tolerance limit is defined below [117]:

$$BFD_U = BFD_{ave} + k_1 s \tag{5.2}$$

BFD_{ave} is calculated as follows:

$$BFD_{ave} = \frac{1}{N}\sum_{i=1}^{N} BFD_i \tag{5.3}$$

N represents the number of BFD measurements for a particular model, resulting from valid shots, in which the size, conditioning state, and test threat are identical. BFD_i are the individual BFD measurements. The sample standard deviation, s, is calculated as shown below:

$$s = \sqrt{\frac{1}{N-1}\sum_{i=1}^{N}(BFD_i - BFD_{ave})^2} \tag{5.4}$$

The k_1 factor for the unilateral tolerance interval was computed per NIJ [117] based on the experimental data.

For the analysis of BFD measurements in accordance with the requirements of this NIJ standard, the probability that no BFD measurement exceeds 44.0 mm must be at least 80%. After performing the calculations for the factor k_1, its value is: $k_1 = 1{,}568$

Table 5.9 summarizes the individual BFD values obtained experimentally for each designed ballistic architecture, corresponding to a total of 12 shots for each configuration. The data allow evaluation of result dispersion and repeatability of ballistic behavior, as well as direct comparison of performance among the analyzed architectures. Clear differences between configurations can be observed, with hybrid architectures generally exhibiting lower and more uniform BFD values compared to the structure composed exclusively of Twaron, indicating a superior capacity for absorption and dissipation of impact energy.

Table 5.9. Experimentally obtained datasets for each designed architecture

Architecture code	Individual BFD values (mm) for 12 shots											
20T	35	42	42	28	32	31	44	31	34	43	34	32
7T5D8T	31	35	32	26	33	26	34	29	28	32	27	31
8T2D7T	35	39	40	29	35	32	42	30	38	33	28	31
15T4XD	44	42	34	29	37	34	38	31	32	34	30	34
1EXO15T	30	36	35	25	36	30	34	30	35	31	29	36

Table 5.10 presents the statistical summary of the ballistic results obtained for the analyzed architectures, including the arithmetic mean of BFD, the sample standard deviation, and the upper tolerance limit (BFD_U). The values highlight clear differences between configurations, with hybrid architectures generally exhibiting lower mean BFD values and smaller dispersion, indicating more stable ballistic behavior.

Table 5.10. Characteristics of BFD values for each architecture

Architecture code	Mean BFD (mm)	Standard deviation, s (mm)	Upper tolerance limit, BFD_U (mm)
20T	35,67	5,72	44,63
7T5D8T	30,33	5,19	38,47
8T2D7T	34,33	4,59	41,54
15T4XD	34,92	4,60	42,13
1EXO15T	32,25	4,52	39,35

The upper tolerance limit for BFD_U within NIJ 0101.07 [117] remains an essential criterion for evaluating the risk of deformation-induced trauma under impact; the reference value is 44 mm, and interpretation of the results must be performed within a statistical framework that differentiates between “below the limit,” “slightly above,” and “significantly below the limit,” taking into account dispersion and impact energy.

Table 5.11. Results interpretation

Architecture code	Upper tolerance limit, BFD_U (mm)	Interpretation
20T	44,63	Slightly above the 44 mm limit – greater variation
7T5D8T	38,47	Significantly below the 44 mm limit – uniform deformation due to impact energy and efficient absorption
8T2D7T	41,54	Below the 44 mm limit – low dispersion, stable behavior
15T4XD	42,13	Below the 44 mm limit – low dispersion, stable behavior
1EXO15T	39,35	Significantly below the 44 mm limit – uniform deformation due to impact energy and efficient absorption

The reference structure composed of 20 layers of Twaron T730 exhibits the highest BFD_U value, approaching the maximum allowable limit, indicating a reduced capacity to control rear-face deformation.

The hybrid architectures show significantly lower BFD_U values, confirming the effectiveness of incorporating Dyneema and Kevlar layers. The best performance is achieved by the 1EXO15T architecture, which presents the lowest upper tolerance limit, followed by 7T5D8T, demonstrating a clear reduction in the risk of exceeding the threshold imposed by ballistic standards.

High-speed imaging of the impact behavior of protective materials

Figure 5.19 presents successive images of the impact from Shot 1 for the architectures 20T, 7T5D8T, 8D2D7T, 15T4XD, and 1EXO15T with a .357 SIG projectile, captured with a high-speed camera at 20,000 frames per second. The camera used and its specifications are described in Subsection 5.2.

a) 20T Architecture

b) 7T5D8T Architecture

c) 1EXO15T Architecture

Fig. 5.19. High-speed sequence of Shot 1 impact with a .357 SIG projectile (20,000 fps)

The comparative analysis clearly shows that the material response is governed by how the kinetic energy is absorbed, distributed, and dissipated through stretching, shearing, local compression, and, in some cases, progressive rupture. In all sets (Figures 5.19a and c), the same general sequence is observed: initially, a localized disturbance appears in the contact area (impact), followed by the formation of a deformation "cone" (bulging) and propagation of stresses toward the edges; subsequently, depending on the material architecture, either perforation occurs, or the deformation spreads over a larger area, indicating more efficient energy absorption through plastic deformation and stretching.

20T Architecture. In the first set (Fig. 5.19a), the material exhibits a predominantly local response to impact, with initially relatively small deformation, followed by a progressive increase in both depth and diameter of the deformed area. Subsequently, a radial "flaring" of the material is observed, suggesting that the layers are able to redistribute stresses toward the edges before major rupture occurs. The deformation develops a pattern of radial folds, typical of flexible materials, in which energy is absorbed through fiber stretching and relative sliding between layers. Although the deformation is extensive, no complete arrest of the phenomenon is observed in the final frames, indicating advanced penetration of the layers with gradual energy loss.

7T5D8T Architecture. The second panel (Fig. 5.19b) exhibits a similar response mechanism, but with an important difference: the deformation appears to spread more rapidly and uniformly across the plane, and the deformation "cone" has a more symmetrical geometry. In the initial frames, the impact produces a central compression zone, after which the material stretches radially and the folds organize more coherently. This pattern suggests a structure that allows more efficient transmission of the stress wave toward the edges, meaning that the projectile's energy is dissipated over a larger area. From a mechanical perspective, this is indicative of improved energy absorption through global deformation, reducing stress concentration strictly at the impact point. At the same time, the increasing deformation amplitude indicates that the material primarily fails through fiber stretching.

1EXO15T Architecture. In the fifth set (Fig. 5.19c), the main difference is the very large deformation amplitude and the membrane-like nature of the response: the material behaves as a tensioned surface that absorbs energy through global stretching, with radial folds highly pronounced. Rapid propagation of the deformation toward the edges is observed, suggesting a high capacity for stress distribution and, consequently, more efficient energy dissipation across the entire structure. The extreme deformation indicates that the material does not fail in a brittle manner immediately, allowing energy absorption through plastic and elastic deformation.

Comparative examination of projectiles extracted from the fabricated ballistic structures

Figure 5.20 presents comparative images of .357 SIG FMJ projectiles extracted from the ballistic structures 20T, 7T5D8T, and 1EXO15T. These images highlight the morphological characteristics of the projectiles after impact and identify the changes resulting from interaction with the ballistic structure.

It can be observed that the projectile deformation is quite similar in all three cases for Shot 1. The projectiles recovered from the 20T and 7T5D8T architectures after Shot 1 (Fig. 5.20a, b), as well as from the 1EXO15T architecture after Shot 2 (Fig. 5.20c), exhibit highly irregular deformations. Some are laterally flattened and show pronounced expansion, with widely opened petals and a much more visible frontal cavity. The metal jacket displays numerous cracks, and in certain cases, partial separation between jacket segments and the lead core is observed, suggesting a "peeling" process caused by extreme stresses. In some projectiles, the area around the frontal cavity appears almost "torn," consistent with very rapid deceleration. These features indicate that the energy was dissipated not only through expansion but also through structural collapse and chaotic deformation, leading to a significant loss of the projectile's geometric stability.

The .357 SIG projectiles from Shots 2–3 (Fig. 5.20a, b), as well as Shot 1 in the 1EXO15T architecture (Fig. 5.20c), display similar morphological characteristics.

a) 20T Architecture (Specimen 2)

b) 7T5D8T Architecture (Specimen 2)

c) 1EXO15T Architecture (Specimen 3)

Fig. 5.20. Recovered .357 SIG projectiles from the tested ballistic structures

The deformation is moderate, with a symmetric mushrooming effect and preservation of the projectile's overall shape. The tip appears visibly flattened, and the jacket is rolled into thick petals. Short radial cracks and small openings are observed at the jacket edge, but there are no extensive ruptures or significant material loss. The copper surface remains visible over large areas, suggesting moderate abrasion and good preservation of jacket integrity.

From a materials mechanics perspective, the observed differences can be explained by the ratio between the resistance of the medium and the ductility of the jacket. In environments that induce high and uniform frontal pressure, the jacket undergoes plastic deformation and rolls into relatively symmetrical petals, with cracks occurring primarily due to tensile stresses at the edge of the expansion.

5.5. Micro and macro-scale analysis of aramid fiber degradation in the tested structures

5.5.1. Preparation of aramid fiber-containing specimens for investigation using an electron microscope

Preparation of specimens containing aramid fibers for scanning electron microscopy (SEM) involves several steps to ensure high-quality imaging. This approach can also be applied, with appropriate adjustments, to other polymeric fibers. In this study, the specimens were coated with a 6 nm gold alloy layer using a Sputter Coater, with coating device parameters as follows: vacuum pressure – 6 mbar, plasma current intensity – approximately 18 mA, and working distance – 50 mm. SEM images were obtained using an FEI Quanta 200 scanning electron microscope. Its characteristics include a resolution of 4 nm, magnification up to 1,000,000×, and software for control and analysis, including an EDX spectrometer [19], [102].

5.5.2. Failure mechanisms of aramid fibers under ballistic impact

Filament, yarn, and fabric failure mechanisms can be studied at both microscopic and macroscopic scales.

Localized yarn fracture occurs when the fibers fracture almost simultaneously, typically at the sharpest point of contact with the penetrator, accompanied by a characteristic sound and a sudden drop in load. The main mechanisms are axial stretching and through-thickness shearing, with failure occurring when the deformation exceeds the breaking limit. This limit decreases as the strain rate increases [68].

Multi-point failure occurs when yarn fibers rupture at different locations along their length, beyond the impact zone, potentially between the strike point and clamping edges. This reflects broader deformation distribution due to force direction variability or structural non-uniformities, resulting in more gradual degradation and potentially reduced protective efficiency [68].

Yarn pullout occurs when none of the fibers in a yarn break, but one end of the yarn is pulled out of the fabric network. This type of damage typically occurs only in weakened or unanchored yarns (usually at the edges). The force required to pull the yarn from the network is determined by the friction between the yarn in question and the perpendicular intersecting yarns. As the yarn is pulled, the number of intersecting yarns gradually decreases, resulting in a reduction of the measured load [68].

Fibrillation is a mode of failure in which fibers fragment longitudinally into finer filaments. The process is promoted by abrasion along the fiber, combined with the effects of tension, and in multilayered structures, interlayer friction contributes to transverse abrasion. This phenomenon can lead to fiber splitting, particularly under impact from semi-spherical, ogival, or conical projectiles, and its manifestation is similar to that observed in single-layer systems [28].

Bow, bulging, or misalignment of orthogonal yarns represents another damage mechanism observed in multilayer fabrics, particularly in the rear layers of the material package. Lim et al. [49] emphasized that bowing becomes more pronounced in these layers, where the projectile, having been significantly decelerated by the preceding layers, attempts to penetrate with an edge-first approach. This "bowing" or "bulging" phenomenon occurs when the yarns in the fabric are not perfectly aligned, exhibiting curvature in the direction of projectile penetration.

5.5.3. Scanning electron microscopy (SEM) analysis of Twaron T730 fabric panels after ballistic impact

Figure 5.21 shows the 5-layer Twaron T730 panel

a) b)

Fig. 5.21. Panel composed of 5 layers of Twaron T730: (a) front and rear of the panel (three shots with a .357 SIG projectile); (b) front and rear of the panel (three shots with a .357 SIG projectile).

The results for the .357 SIG FMJ projectile are not acceptable, as complete penetration occurred, and the BFD values from the other two shots are sufficiently high to consider that this panel does not provide adequate protection.

a) b)

Fig. 5.22. Panel composed of 15 layers of Twaron T730: (a) front and rear of the panel (three shots with a .357 SIG projectile); (b) front and rear of the panel (three shots with a .357 SIG FMJ projectile; red circles indicate the shot with complete penetration).

Figure 5.23 presents images of damaged aramid fibers, with the details shown below each image in the first row highlighted in the yellow circle. These details illustrate structures described by Richard et al. [77] for aramid fibers, but damaged under low tensile strain rates.

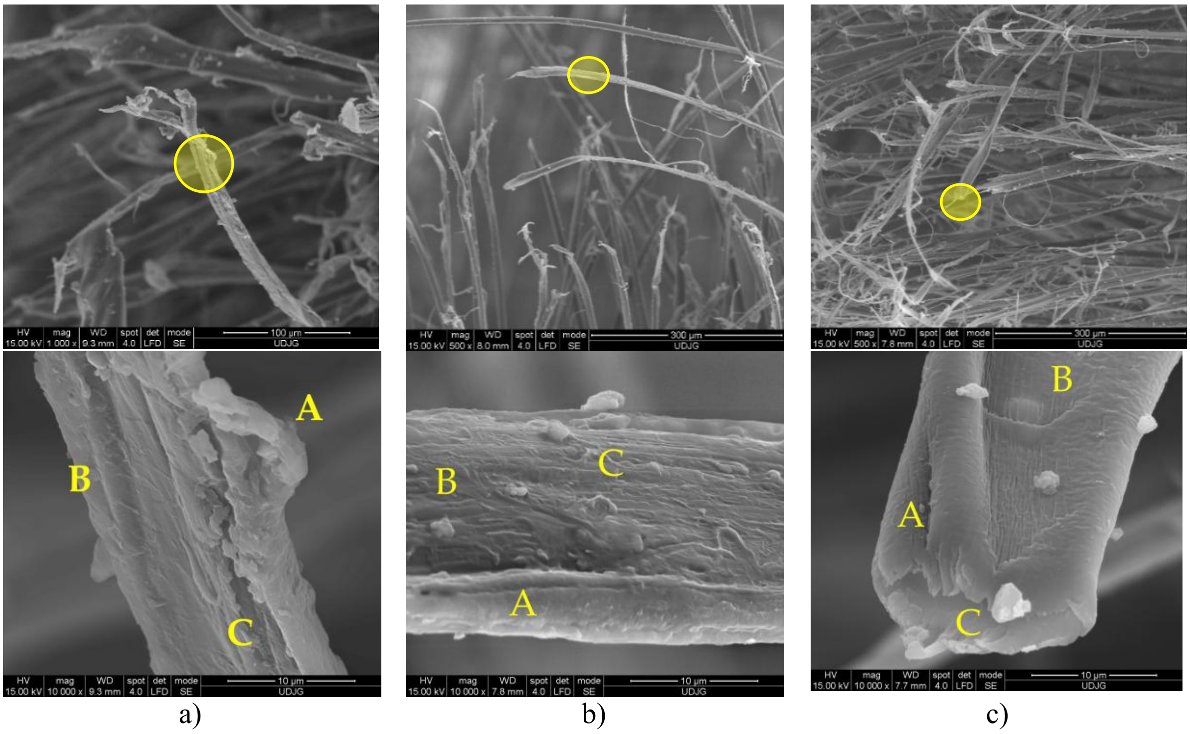

Fig. 5.23. Characteristic microstructures of damaged aramid fibers [19]: (a) fiber from the first layer of a 5-layer Twaron T730 panel, impacted by a 9 mm FMJ projectile (v_0 = 371 m/s); (b) fiber from the first layer of a 5-layer Twaron T730 panel, impacted by a .357 SIG projectile (v_0 = 448 m/s); c) same layer, another fibern [19]

Projectile velocities reported in this study were measured using a chronograph. The target was fixed 5 m from the muzzle of the ballistic barrel.

The failure modes observed in SEM images for a damaged aramid fiber are presented as follows (Fig. 5.23):

a) fiber from the first layer of a 5-layer Twaron T730 panel, impacted by a 9 mm FMJ projectile (V_0 = 371 m/s): A – fragment of the jacket partially detached from the core, exhibiting a visible flake-like structure; B – microfibrils with smaller lateral bonds; C – evident fibrillation.

b) fiber from the first layer of a 5-layer Twaron T730 panel (areal density 260 g/m²), impacted by a .357 SIG projectile (V_0 = 448 m/s): A – jacket exhibiting fibrillation; B – disordered path, with a band of entangled ends visible next to the label; C – fibrils with straight alignment.

c) The same layer, another fiber: at a magnification of ×10,000, the broken end of the fiber reveals the following features: A – fibrillation; B – detachment of a short micro-block in the region of the entangled macromolecular chain ends; C – the fractured surface of the fiber end, which reveals two levels of fibrils. The fracture of this fibril may have occurred through shear, as the broken fibril ends are not elongated.

High-velocity impact generates localized stresses and deformations on aramid fibers, leading to their rupture. The SEM images in Figure 5.24 were taken at low magnification to illustrate how the same fabric behaves under different ballistic conditions. The first layer of each panel shows multiple broken yarns, but it is difficult to associate a specific image with a particular panel type (the 5-layer panels experienced complete penetration for both projectiles, while the 15-layer panels successfully stopped the projectiles).

15-layer

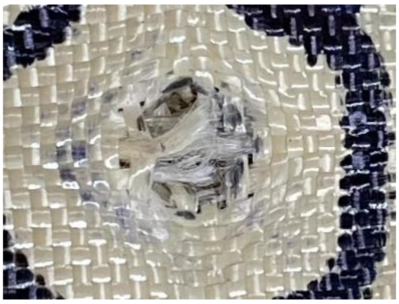

(e) 9 mm FMJ, V_0=371 m/s

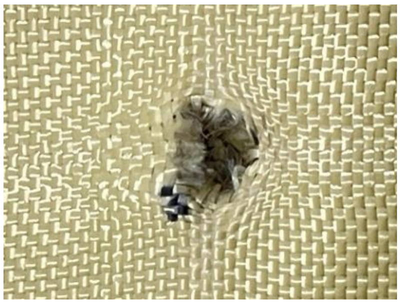

(f) .357 SIG, V_0=448 m/s

15-layer

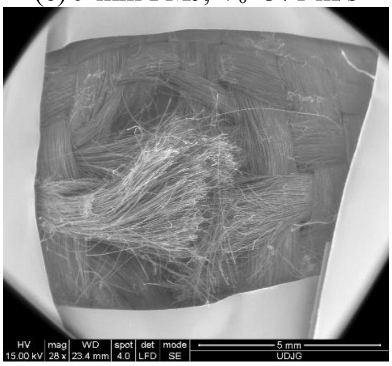

(g) 9 mm FMJ, V_0=371 m/s (mag. x28)

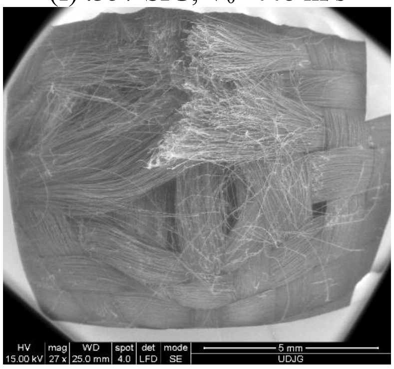

(h) .357 SIG, V_0=448 m/s (mag. x27)

Fig. 5.24. View of the hole produced by projectile impact on the studied panels made of Twaron T730. Testing conditions: air temperature 21 ± 3 °C, relative humidity 47%, atmospheric pressure 760 ± 15 mm Hg [19]

The flattened tip of the .357 SIG projectile compresses the yarns and causes local fiber breakage; a similar effect occurs with the 9 mm FMJ projectile. In thinner panels, the fibers remain more orderly due to higher deformability. After perforation, a whipping effect appears, resulting in pronounced fiber entanglement, which is more significant at higher velocities.

Delamination can be analyzed at different scales:

- at the microscopic scale, it consists of fibers detaching from their matrix,
- at the mezzo or macroscopic scale, layer separation becomes visible.

Multiple layers of aramid fabric are commonly used in ballistic vest construction; however, the forces generated by impact can cause layer separation, thereby reducing their efficiency in energy absorption.

All SEM images in Figure 5.25 were taken from the first layer of a 5-layer Twaron T730 panel after impact by a .357 SIG projectile, with an impact velocity of 448 m/s.

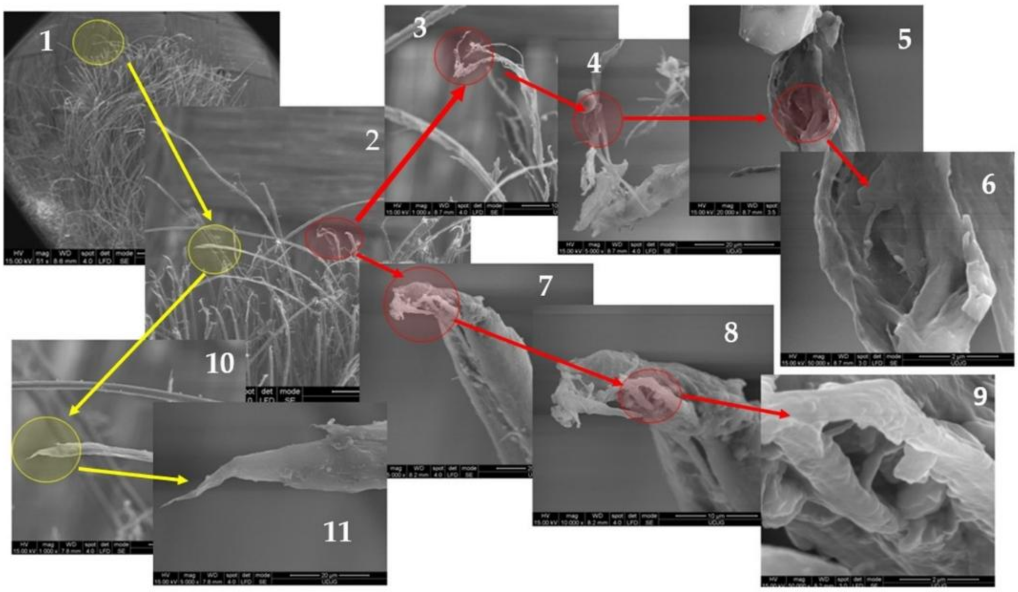

Fig. 5.25. Progressive magnification showing aramid fiber failure mechanisms post-ballistic impact [19]

The red and yellow arrows indicate the next magnification of a region of interest. The SEM images in Figure 5.25 are detailed as follows:

1 - lowest magnification (×50) – shows a main yarn (the yarn carrying the projectile impact and typically exhibiting the greatest damage), but the fiber failure mechanisms are not yet visible;

2 - magnification of image 1 (×200) – two damaged fibers are identified for discussion, marked with a red and a yellow circle; these colors are maintained in subsequent images if the same fiber is depicted;

3 - detail of the broken fiber (×1000) – shows necking at the fiber tip, with broken fibrils of different sizes indicating regions with distinct mechanical properties due to discontinuities in molecular order and size;

4 - next magnification (×5000) – illustrates the action of fibrillation in this fiber, revealing non-uniform fibrillation;

5 - detail of a local split between fibrils (×20000);

6 - detail of the fibrillation zone (×50000);

7 - detail of the red circle from image 2 (×5000) – shows a shear cut with necking at the fiber tip, reflecting the high-speed process (ballistic impact);

8 - detail of the broken fiber tip (×10000);

9 - (×50000) – very thin microfibrils are visible between the fibrils along the fiber axis;

10 - fiber along ~100 μm (×1000) – shows multiple failure mechanisms: tip rupture by tension, fiber necking, and local splitting of fibrils;

11 - the detail of the broken fiber (×5000) suggests a sudden tensile fracture, with a short fibril segment exhibiting a conical shape, indicative of polymer failure.

Figure 5.26 illustrates the different types of fiber deformation, providing examples of necking and flattening described previously. Necking occurs in regions of maximum stress, leading to narrowing and eventual fiber rupture. Flattening is caused by the pressure exerted by the projectile, altering the fiber shape and influencing the material's impact behavior.

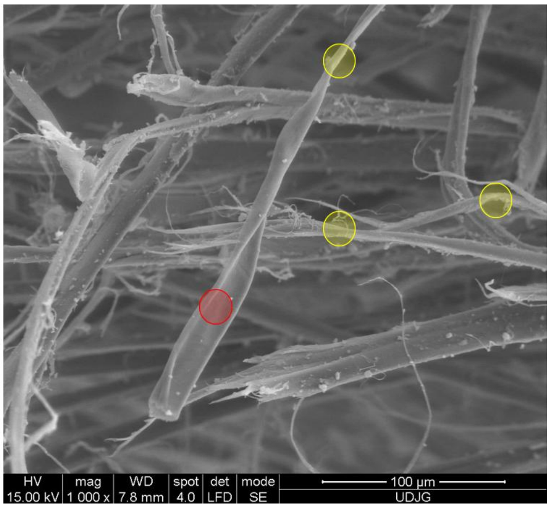

Fig. 5.26. Damaged fibers from the front face of layer 1 in a 15-layer Twaron T730 panel, impacted by a .357 SIG projectile (V_0 = 448 m/s). Fiber deformation: yellow circles – necking; red circles – flattening [19].

Progressive magnification (×27–×10,000) of the 15-layer Twaron T730 structure under 9 mm ballistic testing.

Figure 5.27 illustrates how SEM analyses are performed through successive image magnifications. Based on these images, the following description can be made:

a) at relatively low magnification (×28), which can also be achieved with a high-quality camera lens, the size of the hole remaining in the first layer is highlighted, showing the main yarns (partially or fully broken by the projectile) and secondary yarns (laterally pressed by the projectile passage), both in the weft and warp directions.

b) at ×1,000 magnification, a fiber split at the tip is visible, with fibrils observable but not in detail, bent due to the forced passage of the projectile after fiber rupture.

c) at ×2,000 magnification, the fiber shows areas damaged by fibrillation, flattening, and end-fibril tensile rupture.

d) at ×5,000 magnification, these mechanisms are seen more clearly, with local elongation (necking) at the broken fiber ends.

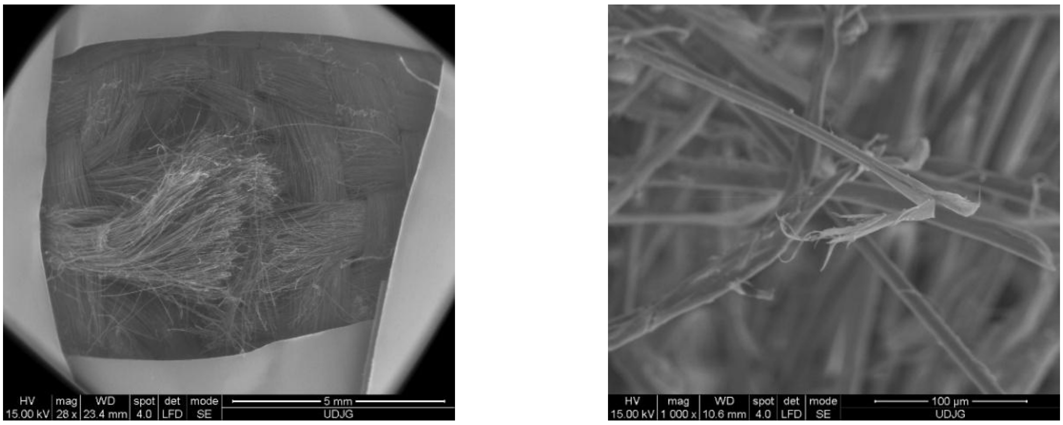

a) ×28 b) ×1000

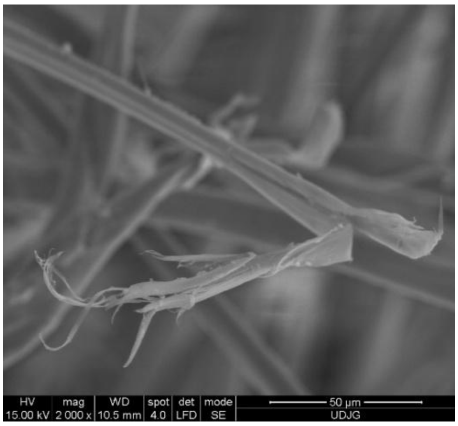

c) ×2000

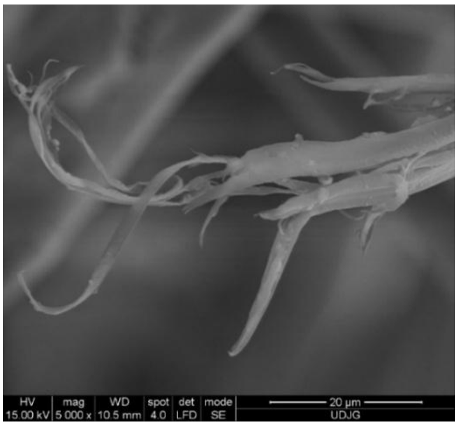

d) ×5000

Fig. 5.27. Progressive magnification (×28–×10,000) of the 15-layer Twaron T730 panel, 9 mm projectile

Progressive magnification (×27–×10,000) of the 15-layer Twaron T730 panel, .357 SIG projectile.

In Figure 5.28, image (f) shows a detail of the space between two microfibrils, with undulated surfaces, likely resulting from mechanical stress, at one of the highest magnifications used in this study (×10,000). In image (e), the measurement of several microfibrils is shown; these actually have nanometer-scale transverse dimensions.

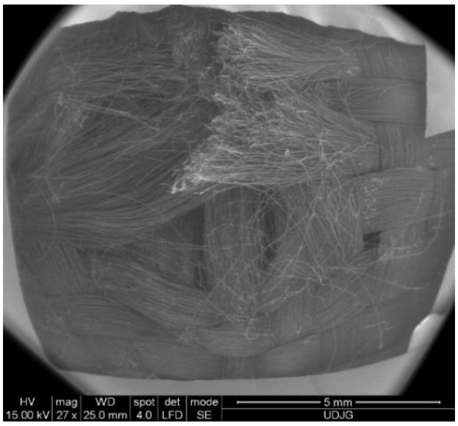

a) ×27

5 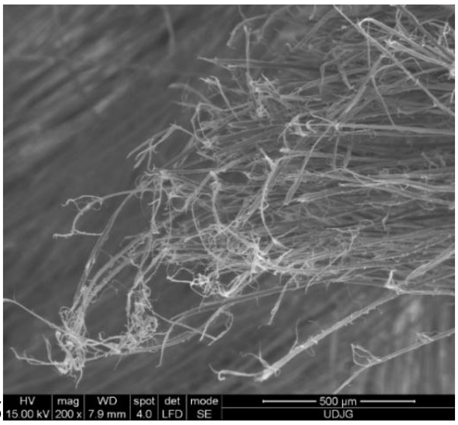

b) ×200

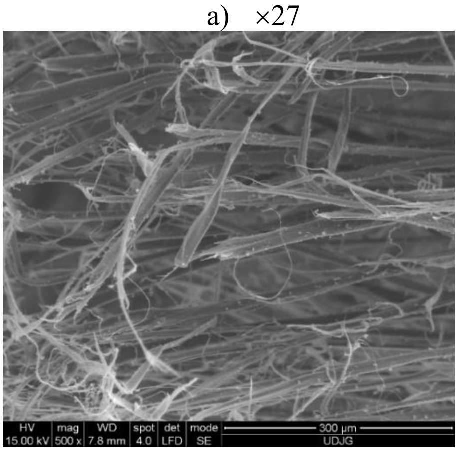

c) ×500

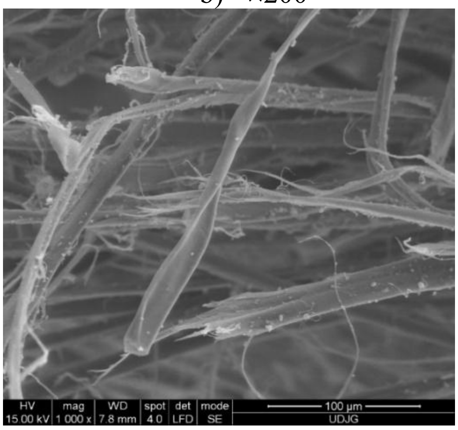

d) ×1000

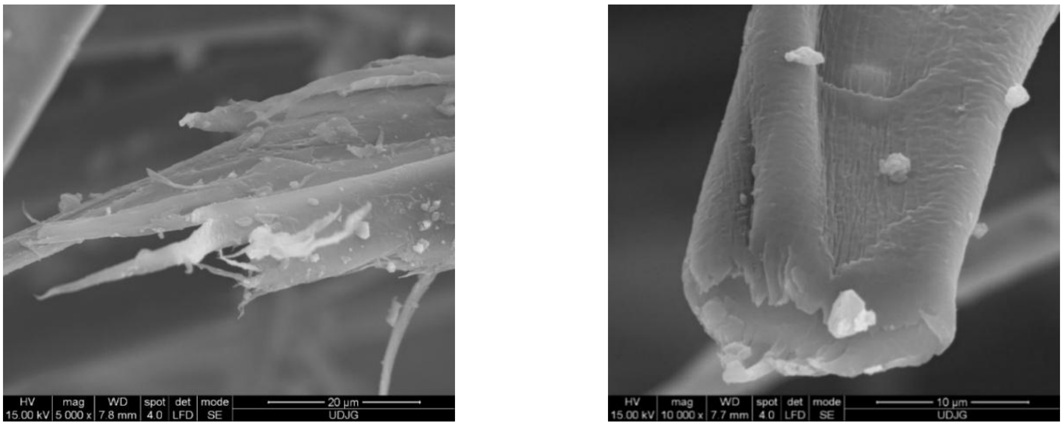

e) ×5000 f) ×10000

Fig. 5.28. Progressive magnification (×27–×10,000) of the 15-layer Twaron T730 panel, .357 SIG projectile

5.5.4. Scanning electron microscopy (SEM) analysis of the 1EXO15T architecture after ballistic impact

Figure 5.29 presents photographs of the tested structure, composed of one layer of Kevlar® EXO™ CoreMatrix™ CM E1100H and 15 layers of Twaron T730, stitched on all sides at 8–10 mm from the edges. The panels measure 300 mm × 300 mm, and the distance between impact points is 120 mm.

a) b)

Fig. 5.29. Panel composed of one Kevlar® EXO™ layer and 15 layers of Twaron T730: after testing with a .357 SIG FMJ projectile (3 shots)

Figure 5.30 presents a comparison between the macroscopic appearance and the scanning electron microscopy (SEM) morphology of impact-induced damage.

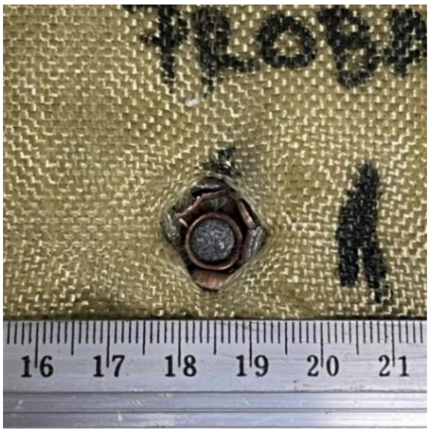

a) shot 1, V_0 = 451 m/s

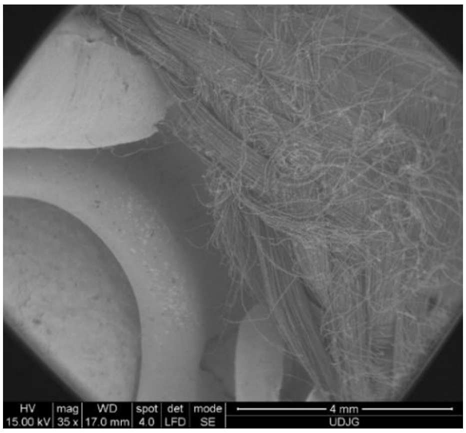

b) shot 1, V_0 = 451 m/s (mag. ×35)

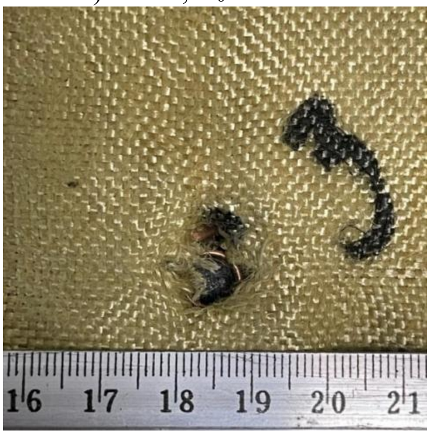

c) shot 3, V_0 = 451 m/s

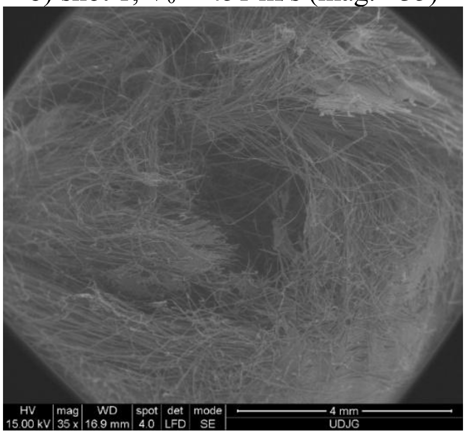

d) shot 3, after projectile extraction, V_0 = 451 m/s (mag. ×35)

Fig. 5.30. View of the hole produced by .357 SIG FMJ projectile impacts on the 1EXO20T structure

The macroscopic images (a, c) highlight the size of the entry hole and the affected area on the material surface. The SEM images (b, d) show microstructural details, such as broken and pulled fibrils and localized delaminations of the structure. A predominant fiber failure mechanism through tension and shear is observed, with extensive fibrillation zones. The macro–micro correlation confirms energy dissipation through progressive deformation and fragmentation of the fiber network.

The SEM image set in Figure 5.31 captures, at successive magnification levels, the evolution of failure mechanisms of Kevlar EXO fibers in the ballistic impact zone (Shot 1), providing a coherent view of how this 3D-type fabric dissipates projectile energy.

At ×1,000 magnification (Fig. 5.31c), severe deformation of the three-dimensional fiber network is evident, with misaligned, stretched, and pulled fibers from the original architecture. The 3D fabric configuration facilitates load redistribution in multiple directions, including through the connecting fibers, reducing localized rupture and contributing to an increased overall energy absorption capacity.

Increasing the magnification to ×2000 (Fig. 5.31d) shows that fiber failure is not brittle but occurs through a progressive process, dominated by longitudinal fiber opening and internal decohesion. Separation of fiber bundles and the appearance of elongated microfibrils are observed, indicating gradual load transfer from the macroscopic structure of the 3D fabric to the microstructural level of the fibers.

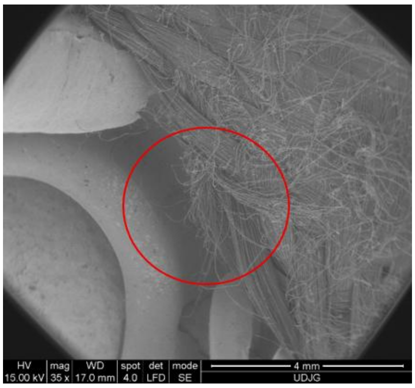

a) ×35

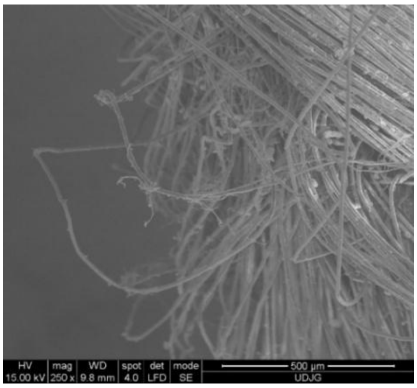

b) ×250

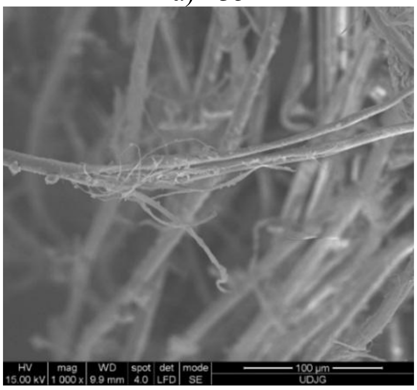

c) ×1000

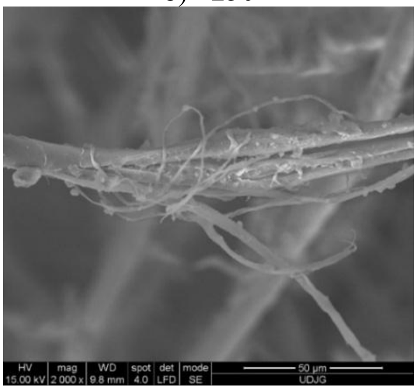

d) ×2000

Fig. 5.31. Magnification from ×35 to ×2000 of the projectile entry area (Shot 1) for the 1EXO15T architecture tested with .357 SIG ammunition

The SEM image set in Figure 5.32 coherently illustrates the damage mechanisms of Kevlar fibers under impact (Shot 2), highlighting the multiscale behavior of the material. At low magnifications (×200), pronounced disorganization of the 3D textile architecture in the impact zone is observed, with fibers significantly displaced, bent, and pulled out, indicating stress redistribution in multiple directions and the involvement of interlaminar fibers in energy absorption. At intermediate magnifications (×1,000), severe plastic deformation of the fibers becomes evident, along with pronounced curvature and longitudinal opening, signaling progressive load transfer from the structural level to individual fibers. The irregular morphology of the failure surfaces confirms the predominantly mechanical nature of the degradation, dominated by tension, shear, and bending.

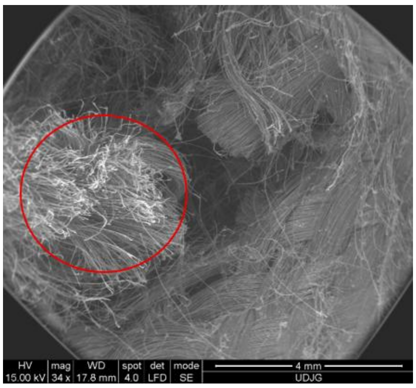

a) ×34

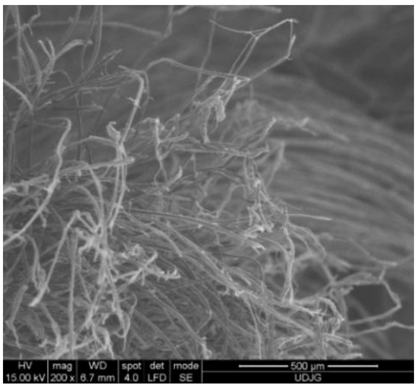

b) ×200

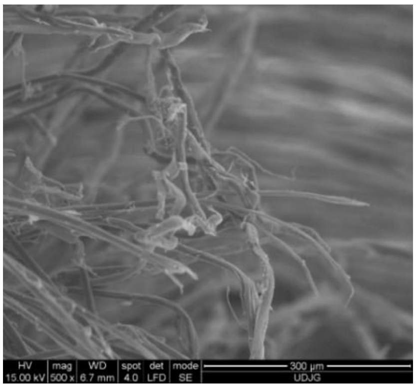

c) ×500

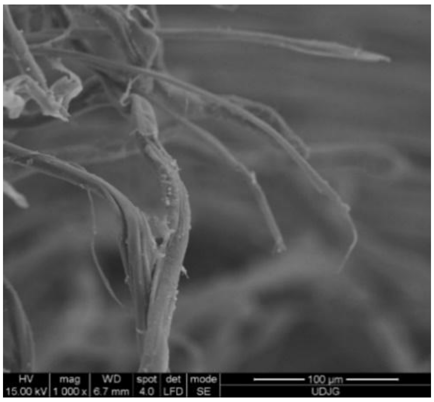

d) ×1000

Fig. 5.32. Magnification from ×34 to ×1000 of the projectile entry zone (Shot 2) for the 1EXO15T architecture tested with .357 SIG ammunition

The SEM image set in Figure 5.33, corresponding to the projectile entry zone (Shot 3), clearly highlights the evolution of fiber damage mechanisms across a wide range of magnifications.

At ×1000 magnification (Fig. 5.33b), different modes of individual fiber failure become evident, marked by regions of severe bending, longitudinal exfoliation, and progressive rupture. The fibers exhibit irregular edges and rough surfaces, indicating controlled, non-brittle failure. The highlighted features suggest initiation of internal decohesion and separation of fibrillar bundles under the combined action of tension and shear.

At ×5000 magnification (Fig. 5.33c, d), fibrillation and internal delamination processes are clearly distinguishable, with thinned, sharp fiber terminations resulting from progressive elongation and separation of microfibrils. The presence of adherent particles on the fiber surfaces is associated with residual material from either intense local abrasion or direct interaction with the projectile during impact.

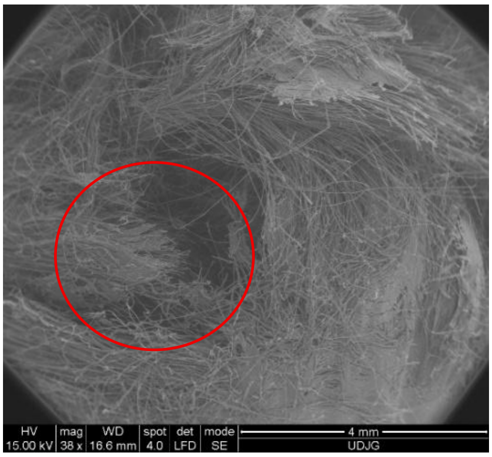

a) ×38

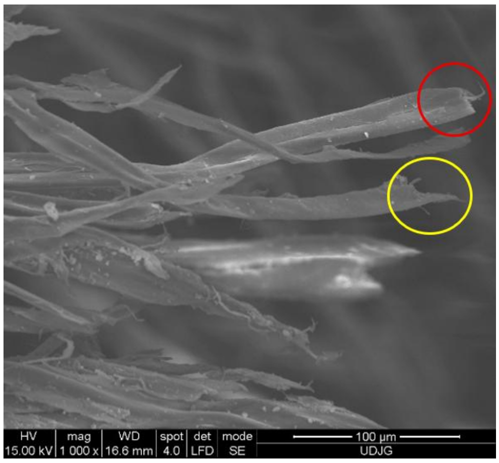

b) ×1000

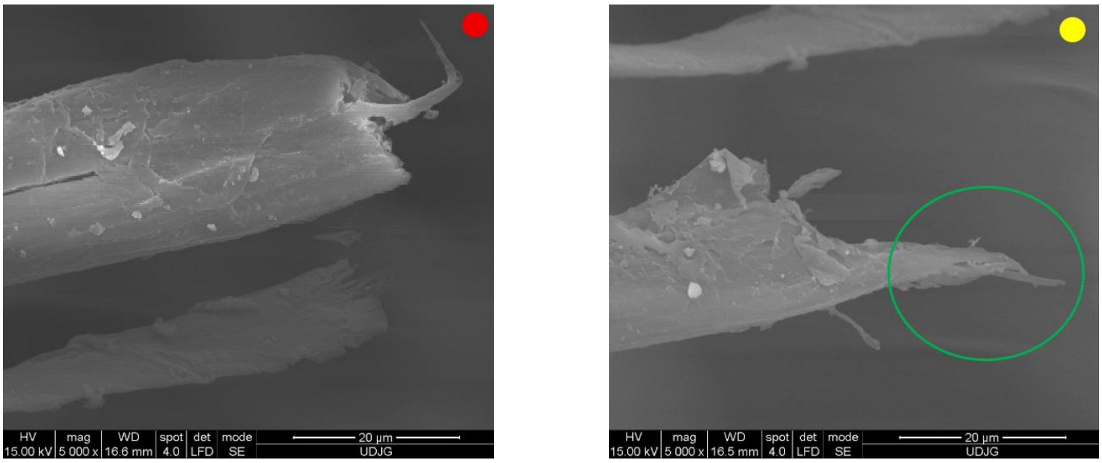

c) ×5000 d) ×5000

Fig. 5.33. Magnification from ×38 to ×5000 of the projectile entry zone (Shot 3) for the 1EXO15T architecture tested with .357 SIG ammunition

5.5.5 Classification of failure mechanisms of aramid fibers

Figure 5.34 provides a classification of the failure mechanisms of aramid fibers observed under ballistic impact and other similar applications. In reference [19], three types of mechanical damage to aramid fibers are analyzed, which may occur under different types of attacks, such as ballistic impacts, knife strikes, and spike threats. Each of these damage types can affect aramid fibers in a distinct manner. There are both similarities and differences among them, which help in understanding how protective materials respond to various types of threats.

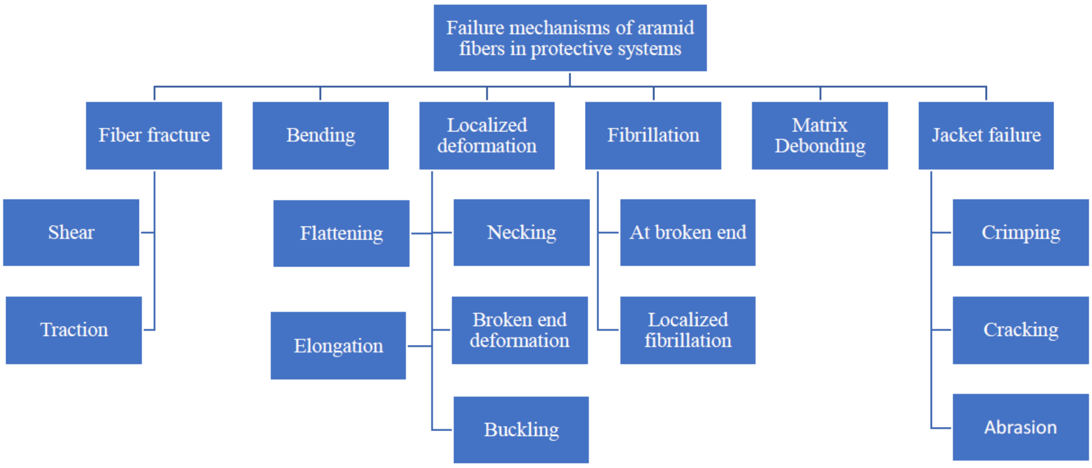

Fig. 5.34. Mechanical failure taxonomy of aramid fibers for protective applications [19]

5.6. Conclusions on the experimental study of hybrid panels for individual protection

The experimental program was structured in two complementary stages. In the first stage, the behavior of monomaterial ballistic panels, made from a single type of semi-finished material, was analyzed under the impact of 9 mm FMJ and .357 SIG FMJ ammunition. The tests were conducted in a specialized laboratory, under controlled conditions, in accordance with the methodology specific to ballistic protection evaluation. Each configuration was subjected to 12 shots, corresponding to the minimum limit specified by the National Institute of Justice standard for determining ballistic performance [116][117].

The obtained results highlighted the performance level of the monomaterial structures and substantiated the need for architectural optimization through hybridization.

The second stage was dedicated to the evaluation of hybrid structures, tested exclusively with .357 SIG FMJ ammunition, considered representative of a higher threat level. This direction was determined by the limited performance observed in the monomaterial panels composed of 15 layers of Twaron T730 fabric. The hybrid configurations incorporated materials relatively recently introduced to the ballistic protection equipment market—Kevlar® EXO™ CoreMatrix™ CM E1100H, Kevlar® XD S002, and Dyneema® SB21—for which the scientific literature still provides a limited number of applied studies. In the national context, the investigation of these solutions remains limited, which confers the research a high degree of timeliness and relevance for the field of ballistic protection in Romania.

For the hybrid structures, BFD parameters were determined, all configurations recording deformation depths below the 44 mm limit imposed by NIJ [116][117]. The statistical analysis included the determination of mean values and upper tolerance limits (BFD_U), in accordance with the NIJ methodology [117], ensuring the robustness of the evaluation.

Compared to the reference panel made of 20 layers of Twaron T730, the hybrid solutions demonstrated superior performance. The 8T2D7T and 15T4XD configurations exhibited similar mean BFD values, while 7T5D8T and 1EXO15T recorded the lowest values, the latter further distinguished by lower statistical variability.

Overall, hybridization led to reductions in the BFD_U parameter of 5.6–13.80% and in BFD_{ave} of up to 14.97%, confirming the efficiency of the proposed configurations compared to the monomaterial reference structure. All hybrid configurations maintained the upper tolerance limit below the 44 mm threshold, unlike the 20T reference panel, which slightly exceeded this value.

The results highlight that hybridization represents not only a technical solution for structural optimization, but also a direction with economic potential, achieved through the strategic use of high-performance materials in the critical areas of the panel while maintaining a controlled areal density. The 7T5D8T configuration exhibited the highest safety margin in terms of backface deformation, whereas 1EXO15T demonstrated a favorable compromise between ballistic performance, statistical stability, and mass.

From a methodological perspective, the research fully leveraged the experimental infrastructure available in Romania, combining instrumented ballistic measurements (velocity determination using a chronograph), high-speed camera recordings, macro- and mesoscopic analyses of the affected areas, as well as microstructural investigations by scanning electron microscopy. The multi-scale approach and the integration of statistical analysis in accordance with the NIJ standard [117] demonstrate the capability to conduct complex experimental research in the field of personal ballistic protection within the existing national infrastructure.

The post-test investigation represented an essential analytical stage in this type of research, rather than merely a descriptive one. The systematic photographic documentation of the impact zones was correlated with mesoscopic analysis and microstructural examination by scanning electron microscopy (SEM), enabling the identification and interpretation of the dominant failure mechanisms: progressive fibrillation, localized fiber rupture, and in-plane stress redistribution within the fabric.

The correlation between microstructural observations and the experimentally determined ballistic parameters provided solid support for the formulated conclusions and strengthened the interpretation of the differences between the analyzed configurations.

The post-test investigations also played an essential role in relation to the numerical model presented in Chapter 3. The experimental determination of the number of failed layers and the analysis of the dominant failure mechanisms provided a direct physical criterion for assessing the adequacy of the modeling assumptions.

The agreement between the numerical results and the experimental observations regarding the extent of damage through the panel thickness confirms the validity of the adopted approach and supports the coherence of the integrated experimental–numerical framework. Thus, the multi-scale analysis conducted in this chapter strengthens the mechanical grounding of the model and reduces the purely theoretical character of its predictions.

CHAPTER 6

CONCLUSIONS AND PERSONAL CONTRIBUTIONS

6.1. Importance and relevance of the study

The doctoral thesis entitled "Experimental and Numerical Study on the Ballistic Behavior of Hybrid Panels for Personal Protection" is part of the scientific efforts aimed at increasing the safety level of individuals exposed to risks generated by individual armed assaults. The work contributes to the development and optimization of modern personal ballistic protection solutions by means of a detailed investigation—through both experimental methods and numerical modeling—of how hybrid panels respond to projectile impact. In this context, the research has a strongly applied purpose, aiming to reduce human vulnerability in critical situations and, implicitly, to save lives by improving the performance of personal protective equipment.

The objective of the study was achieved, as the author designed, tested, and evaluated the behavior of a group of ballistic protection panels, which may be proposed for practical applications. When the results are analyzed from the perspective of Technology Readiness Levels (TRL), this study can be considered to have progressed from TRL 1 to TRL 4[1], with the more high-performing hybrid panel variants, in terms of ballistic protection, expected to advance to the subsequent levels of technological maturity.

During the doctoral program, the author benefited from the support and expertise of specialists experienced in the modeling, analysis, fabrication, and testing of protective panels, from the following institutions:

- Research and Innovation Center for CBRN Defense and Ecology, Bucharest,
- National University of Science and Technology "Politehnica" Bucharest,
- "Dunărea de Jos" University of Galați,
- National Institute for Aerospace Research "Elie Carafoli" – INCAS Bucharest,
- Autonomous Flight Technologies.

The expertise of the personnel and the available infrastructure contributed to extending the individual research capabilities and to the development of an in-depth analysis of the addressed topic.

The experimental program was carried out in two stages. The first stage aimed to evaluate the ballistic behavior of protection structures made from a single type of textile semi-finished material under impact from 9 mm FMJ and .357 SIG FMJ ammunition, through range testing, as well as to partially verify compliance with NIJ Standard 0101.07 [117]. Compliance was considered partial because protection levels require testing with specific caliber

---

[1] ***TRL 1** – Basic principles observed and reported; **TRL 2** – Technology concept formulated; **TRL 3** – Experimental proof of concept; **TRL 4** – Technology validated in laboratory environment; **TRL 5** – Technology validated in relevant environment; **TRL 6** – Technology demonstrated in relevant environment; **TRL 7** – System prototype demonstrated in operational environment; **TRL 8** – System complete and qualified; **TRL 9** – Actual system proven in operational environment [120]*

combinations, and the ammunition used covered only part of those requirements, while the number of tests per panel type was lower than the requirements specified in the U.S. standard.

The second stage focused on evaluating hybrid structures tested exclusively with .357 SIG FMJ ammunition, as the author considered this threat to be more severe, and given that the initially tested monomaterial panels made of 15 layers of Twaron T730 fabric exhibited unfavorable characteristics. The hybrid panels designed by the author incorporated materials relatively recently introduced to the specialized market—Kevlar® EXO™ CoreMatrix™ CM E1100H (manufactured by DuPont) [110], Kevlar® XD S002 (manufactured by DuPont) [112], and Dyneema® SB21 (manufactured by DSM, later Avient Corporation) [113]—for which very few studies have been reported in the scientific literature, or none at all.

6.2. Overall conclusions

The present research study constitutes a coherent work, integrating a synthetic analysis of relevant contributions reported in the specialized scientific literature, a systematic presentation of advanced materials used in the field of ballistic protection, and a critical evaluation of experimental investigations concerning the ballistic performance of materials and protective panels developed from specialized technical fabrics.

From a structural perspective, the work is organized into six interdependent chapters, whose logical sequence facilitates the interpretation of the behavior of hybrid layered materials based on semi-finished products made from special fibers, grounded in data obtained through numerical simulations and experimental testing conducted by the author.

Ballistic protection systems are characterized by a significant diversity of structural configurations, constituent materials, and their combinations. The complexity of impact interactions, the variety of failure mechanisms, and the behavioral changes of the involved materials require a systematic approach to ballistic protection design, as well as a detailed analysis of damage mechanisms. Analytical, empirical, and semi-empirical models aim to describe the behavior of protection systems under specific conditions; however, they generally exhibit limited applicability to narrow ranges of influencing parameters and often to a particular type of ballistic threat.

The modeling of projectile–layered package impact, performed for both simple and hybrid configurations, highlighted the essential role of the Kevlar EXO layer positioned as the first layer over the Twaron T730 package. The experimental results presented in Chapter 5 indicate that the structure composed exclusively of Twaron T730 exhibited both partial and complete penetrations under the impact of the modeled projectile, whereas the hybrid structure showed only partial penetrations, with the projectile being stopped within the first layer. It should be noted that the properties of the Twaron T730 layers were taken from the technical catalog of Teijin, while the properties of the Kevlar EXO layer were not experimentally validated within the present study; the results associated with this layer are based on numerical modeling used for hybrid structure optimization.

The author validated the numerical model by comparing the number of affected layers with the experimental results obtained for similar structures. In the case of the simple layered structure, composed of 15 layers of Twaron T730, partial penetration events resulted experimentally in four destroyed layers, whereas the numerical model predicted the failure of three layers. For the hybrid layered structure, consisting of one Kevlar EXO layer and 15 layers of Twaron T730, the projectile was stopped in the Kevlar EXO layer in both the experiments and the simulations. The projectile fragmentation pattern observed in the simulations is similar to that recorded experimentally; however, real tests revealed more pronounced projectile deformation and damage compared to the simulation results.

The use of numerical simulations in impact studies provides a major advantage by rapidly delivering relevant data in the product development process for impact protection applications, whether experimental models or prototypes are considered. The application of the finite element method (FEM) in impact simulations represents an important stage in the design of protective systems, facilitating the evaluation of the influence of key parameters on the impact resistance of the structure, even though the accuracy of the results is not always complete. Correlating numerical results with experimental data enables the optimization of structural configurations, significantly reducing the time, costs, and human resources required for extensive experimental campaigns.

Materials such as Twaron T730 were used, along with more recent materials that have only recently entered this field: Kevlar EXO CoreMatrix CM E1100H, Kevlar XD S002, and Dyneema SB21. The technological workflow for manufacturing the layered structures included a sequence of well-defined stages: material sampling, cutting using specialized equipment, configuration of the established architectures, assembly of the layered packages by stitching, and, in the final stage, determination of the mass of the resulting structures.

The results of the experimental campaign, including the description of the measurement and monitoring equipment used, the testing procedure, and the applicable standards employed during the tests, are presented. The analysis of the ballistic test results, based on photographic documentation, high-speed video recordings, and scanning electron microscopy (SEM) investigations, demonstrates that the hybrid ballistic protection structures designed by the author achieve performance levels that support their recommendation for use in prototype development. The correlation of SEM images, macroscopic photographs, and high-speed video sequences enabled the identification and description of failure mechanisms specific to these ballistic structure configurations, as well as the analysis of the dynamics of the impact process.

6.3. Summary of experimental data on the performance of the author-developed hybrid panels

For the hybrid structures, the author determined the characteristic BFD parameters, presented in Table 6.1. Based on the calculated upper tolerance limits, it was found that, for all tested packages, the deformation depth remained below 44 mm, the limit imposed by the National Institute of Justice standard [116] for the evaluation of body armor, which is maintained in the updated version of the standard. It can be observed that the hybridization studied in this thesis yielded better results compared to the monomaterial panel composed of 20 layers of T730. Two panel types, 8T2D7T and 15T4XD, recorded mean BFD values of 41.54 mm and 42.13 mm, respectively, lower yet close to the value for the monomaterial panel. The other two hybrid panel types, 7T5D8T and 1EXO15T, exhibited the lowest BFD values. The

1EXO15T panel also showed the greatest reduction in standard deviation, reflecting more uniform behavior under both multiple impacts and across the four tested panels.

The percentage differences for the analyzed characteristics show that the hybrid panels exhibited BFDU values that were 5.6% to 13.80% lower, while BFDav was also lower than that of the simple reference panel, but only by 2.10% for the 15T4XD panel and by up to 14.97% for the 7T5D8T panel. Despite a smaller percentage difference of 9.58% in BFDav, the 1EXO15T panel also demonstrated improved performance compared to the reference structure.

Table 6.1. Comparative analysis of the statistical parameters resulting from the testing of hybrid structures

Symbol, unit of measurement	Simple archi-tecture	Hybrid architectures							
	20T	**7T5D8T**	**Δ față de 20T**	**8T2D7T**	**Δ față de 20T**	**15T4XD**	**Δ față de 20T**	**1EXO15T**	**Δ față de 20T**
N	12	12		12		12		12	
BFD_U [mm]	44.63	38.47	-13.80	41.54	-6.92	42.13	-5.60	39.35	-11.83
BFDav [mm]	35.67	30.33	-14.97	34.33	-3.76	34.92	-2.10	32.25	-9.587
S_d [mm]	5.72	5,19	-9.27	4.59	-19.76	4.60	-19.58	4.52	-20.97
m_c [g]	480.00	440.00	-8.33	400.00	-16.67	460.00	-4.17	440.00	-8.33
ρ_{arie} [kg/m^2]	5.33	4.88	-8.44	4.44	-16.70	5.11	-4.13	4.88	-8.44

N – number of shots; BFD_U – upper tolerance limit; BFD_{av} – arithmetic mean of BFD values
S_d – standard deviation of BFD values; m_c – calculated mass; ρ_{arie} [kg/m^2] – areal density
Δ realitve to 20T represents the percentage difference in the variation of parameter Xi of panel i relative to the reference panel 20T; Δ relative to 20T $= \frac{X_i - X_{20T}}{X_{20T}} \times 100$ [%]
where *i* denotes one of the hybrid panels
7T5D8T – 7 layers of Twaron T730 + 5 layers of Dyneema SB21 + 8 layers of Twaron T730
8T2D7T - 8 layers of Twaron T730 + 2 layers of Dyneema SB21 + 7 layers of Twaron T730
15T4XD – 15 layers of Twaron T730 + 4 layers of Kevlar® XD S002
1EXO15T – 1 layer of Kevlar EXO CoreMatrix CM E1100H + 15 layers of Twaron T730

A graphical representation of the characteristics of the tested panels (Fig. 6.1) enables the formulation of useful conclusions for selecting one or another of these panels.

- The monomaterial panel exhibits less favorable characteristics compared to the hybrid panels designed by the author.
- The 7T5D8T and 1EXO15T panels show the lowest values of BFDU and BFDav, at the same mass and areal density.

  The reference panel, 20T, has BFDU = 44.63 mm, which is slightly above the NIJ limit (44 mm).

The hybrid panel 7T5D8T exhibits the best performance in terms of BFD (both mean value and upper tolerance limit) and provides the largest safety margin relative to the NIJ threshold:

- BFD_U = 38.47 mm (−13.8%) → greatest reduction
- BFDav = 30.33 mm (−15.0%) → lowest mean value
- Sd = 5.19 (−9.3%)
- Mass −8.3%

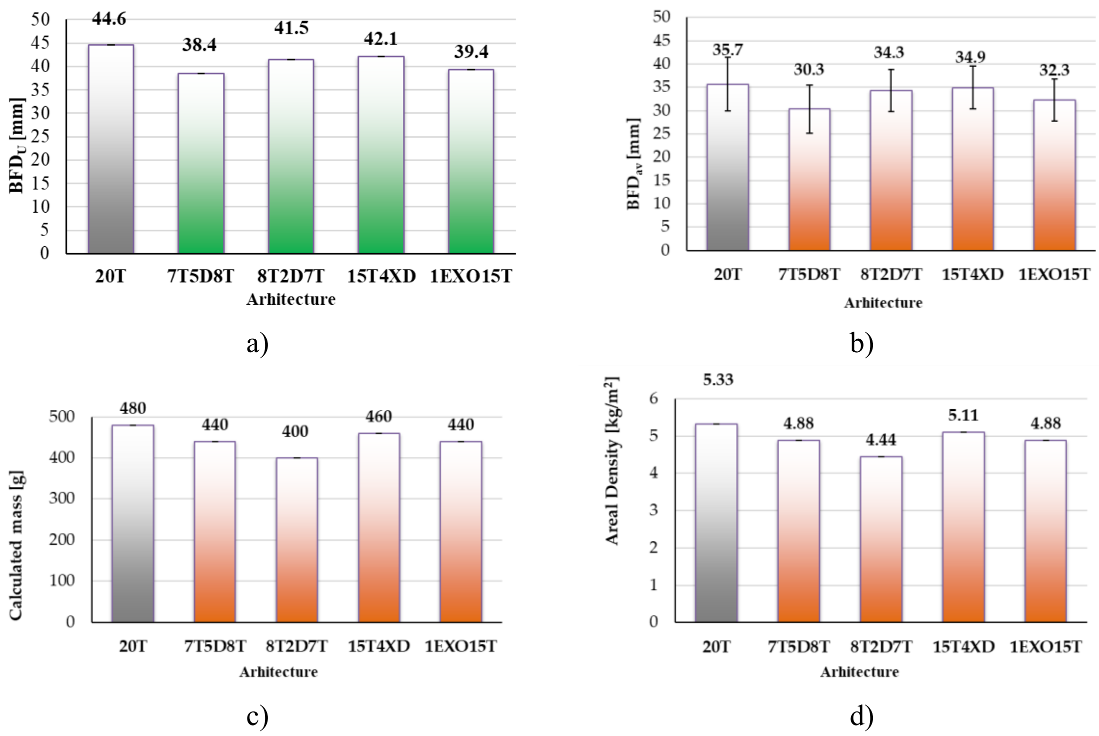

Fig. 6.1. Characteristics of the tested panels

The hybrid panel 8T2D7T is the most efficient in terms of mass; however, its ballistic performance shows a moderate improvement, characterized by a high degree of stability:

- BFD_U = 41.54 mm (−6.9%)
- BFDav = 34.33 mm (−3.8%)
- Sd = 4.59 (−19.8%)
- Mass −16.7% → greatest reduction

The 15T4XD panel exhibits a modest improvement in BFD, good stability, but limited gains compared to the reference panel:

- BFD_U = 42.13 mm (−5.6%)
- BFDav = 34.92 mm (−2.1%)
- Sd = 4.60 (−19.6%)
- Mass −4.2%

The 1EXO15T panel provides an excellent compromise between performance and stability, demonstrates the best statistical consistency, remains below the NIJ threshold, and has a reduced mass:

- BFD_U = 39.35 mm (−11.8%)
- BFDav = 32.25 mm (−9.6%)
- Sd = 4.52 (−21.0%) → lowest dispersion
- Mass −8.3%

In conclusion, the comparative analysis revealed that all hybrid configurations resulted in upper tolerance limit (BFD_U) values below the NIJ threshold of 44 mm, unlike the reference 20T panel, which slightly exceeded this limit. The 7T5D8T configuration recorded the lowest backface deformation values, both in terms of mean and upper tolerance limit, providing the largest safety margin relative to the NIJ criterion. The 1EXO15T configuration demonstrated the best compromise between performance and statistical stability, showing a significant reduction in BFD, the lowest dispersion of results, and a reduced areal density compared to the reference panel. The results confirm the importance of structural architecture optimization in improving ballistic performance without increasing the system mass.

6.4. Author's contributions

The results obtained within the study, through an integrated approach that correlates experimental investigations with numerical simulations, led to the identification of the following original contributions in the field of the design and testing of materials intended for ballistic protection:

- the systematic analysis of relevant documentation to support the theoretical and experimental framework of the study, as well as the structuring of an extensive bibliographic corpus concerning the characteristics and performance of ballistic materials used over time in the development of individual ballistic protection equipment based on aramid fibers and ultra-high-molecular-weight polyethylene (UHMWPE);
- the identification and substantiation of the trend toward the use of hybridization strategies applied to optimize the configurations of individual ballistic protection packages;
- the development of a mesoscale numerical model of projectile–layered panel impact, used to compare, through simulation, the impact resistance of two distinct structural configurations. The model was implemented to evaluate the influence of introducing a Kevlar EXO layer into the baseline configuration composed of 15 layers of Twaron T730. The numerical results were validated through correlation with experimental data obtained in the laboratory, the validation criterion being the number of affected layers. Based on the simulations performed, structural optimization is proposed through the gradual reduction of the number of Twaron T730 layers while maintaining the ballistic performance of the assembly;
- the analysis of the testing campaign results aimed at validating the advantages of hybridizing the initial monomaterial layered structure;
- the determination and analysis of parameters associated with the backface deformation (BFD) in the backing material, as well as the investigation of the failure mechanisms developed within the tested ballistic packages. The obtained results are relevant

for comparing the impact response with that of other configurations reported in the literature and for optimizing the performance of protective structures.

- the testing campaign aimed at the systematic evaluation of hybrid architectures within a clear statistical framework in accordance with NIJ 0101.07, focusing on tolerance limits rather than mean values alone. A correlation between structure, result dispersion, and compliance was established; the findings highlight structural optimization rather than mere characterization;
- the analysis of failure mechanisms of the materials involved in impact, using macrophotography, high-speed video recordings, and SEM images;
- the dissemination of research results was achieved by valorizing part of the author's original contributions through scientific papers presented at international specialized conferences, as well as through the publication of articles in peer-reviewed journals.
- within the research, a dedicated testing methodology for the ballistic packages developed by the author was conceived together with specialists from the Research and Innovation Center for CBRN Defense – Individual Ballistic Protection Equipment Laboratory, Bucharest. In addition, the experimental program was fully organized and comprehensively documented, including the definition of the test articles, their manufacturing approach, the establishment of testing conditions and location, the selection and use of measurement instrumentation, and the typology of the performed tests. The execution of the test campaigns for individual ballistic protection equipment was carried out using the high-performance experimental infrastructure available within the Individual Ballistic Protection Equipment Laboratory.

6.5. Future research directions

The directions for continuing this research are focused on the development of lightweight individual protection equipment capable of providing high resistance to multiple threats:

- the development and characterization of new hybrid materials based on high-performance fibers (aramid fibers, glass fibers, carbon fibers, and polyethylene) at the level of hybrid ballistic structures;
- ballistic impact testing of the developed structures;
- ranking and selection of structural variants that provide effective ballistic protection;
- numerical modeling of impact phenomena at different scales of analysis, from the micro level (fiber), to the meso level (yarns), and to the macroscopic level (layers), aimed at the rapid optimization of structural architecture solutions, followed by the testing of improved solutions through simulation;
- the design and testing of ballistic protection vest prototypes developed based on the 1EXO15T and 7T5D8T architectures, in compliance with current standards, as these were identified as the best-performing configurations in the analyses conducted.

Author’s scientific work

Eng. Christian Popescu

ORCID 0009-0006-2275-7532

Articles indexed in the Web of Science Core Collection and Scopus

1. Deleanu, L., Totolici Rusu, V., Ojoc, G. G., Cristea, G. C., Boțan, M., Vasiliu, A. V., & **Popescu, C**. (2024). The behaviour of stratified fabrics of aramid fibres under stabbing conditions. Polymers, 16(7), 882., DOI: 10.3390/polym16070882 **WOS:001200973600001**
2. Ceoromila, A. C., Deleanu, L., **Popescu, C**., Lom, I., Vasiliu, A. V., **Seiciu, P. L**., ... & Sandu, S. M. (2025). SEM Investigation of Failure Mechanisms in Twaron® Aramid Fibers Used for Personal Armors. Polymers, 17(8), 1058. https://doi.org/10.3390/polym17081058, **WOS:001474511000001**
3. Ojoc G.-G., Rusu V. T., **Popescu C.,** Pirvu C., Deleanu L., Influence of friction in a case of impact simulation, INCAS Bulletin, Volume 12, Issue 4, 2020, pp. 145-154, DOI: 10.13111/2066-8201.2020.12.4.13

Other publications indexed in the Web of Science database
(https://www.webofscience.com/wos/author/record/72420841)

4. Pîrvu, C., **Popescu, C**., Deleanu, L., Vasiliu, A.V. & Ojoc, G.G. (2025). Aspects of Ballistic Panels Made of Unidirectional Aramid Fabrics, Tested Against 9 mm FMJ Projectile. *International conference KNOWLEDGE-BASED ORGANIZATION*, *31*(3), 2025. 120-128. https://doi.org/10.2478/kbo-2025-0087

   Accession Number RC:157974615_S24; eISSN 2451-3113
5. Călinescu, D., Sandu, M. D., Dumitrescu, R., **Popescu, C.,** Alexe, F., & Margin, C. (2024). Approaches to handling major incidents involving chemical, biological, radiological, and nuclear hazards. In International Conference Knowledge-Based Organization (Vol. 30, No. 3). Pp. 43-48, DOI: 10.2478/kbo-2024-0083

   Accession Number RC:146871840_S24; eISSN 2451-3113
6. Deleanu, L., Rusu, V. T., Ojoc, G. G., Cristea, G. C., Boțan, M., Vasiliu, A. V., & **Popescu, C**. (2024). Panels made of composite coated aramid fabrics, under spike weapon attack. In *International Conference KNOWLEDGE-BASED ORGANIZATION* (Vol. 30, No. 3). https://doi.org/10.2478/kbo-2024-0085

   Accession Number RC:141806652_S24; eISSN 2451-3113

7. **Popescu, C.,** Sandu, S., Deleanu, L., Șeiciu, L., & Călinescu, D. (2024). Experimental Study of Twaron T730 For Two Threats. In International Conference KNOWLEDGE-BASED ORGANIZATION, Vol. 30, No. 3, pp. 121-128, DOI10.2478/kbo-2024-0093

   Accession Number RC:147085397_S24; eISSN 2451-3113

8. Titire, L. C., Ojoc, G. G., **Popescu, C.,** & Deleanu, L. (2023). Simulation of an impact on an aramid fabric panel by a. 357 projectile. In International Conference KNOWLEDGE-BASED ORGANIZATION, Vol. 29, No. 3, pp. 1-9, https://doi.org/10.2478/kbo-2023-0068

   Accession Number RC:141277410_S24; eISSN 2451-3113

9. Ojoc, G. G., Titire, L. C., Pirvu, C., & **Popescu, C.** (2022, October). A ballistic impact model for evaluating a preliminary higher level from simulation and tests on a glass fibber composite. In IOP Conference Series: Materials Science and Engineering (Vol. 1262, No. 1, p. 012057). IOP Publishing. DOI 10.1088/1757-899X/1262/1/012057 (Prezentată și la 10th International Conference on Advanced Concepts in Mechanical Engineering (ACME 2022)

Papers presented at international conferences

10. **Popescu, C**., Vasiliu, A.V., Călinescu, D., Cristea, G.C., Sandu, S.M. & Deleanu, L. (2025). Aspects of Ballistic Panels Made of Endumax XF33, Tested Against Different Projectiles. *International conference KNOWLEDGE-BASED ORGANIZATION*, *31*(3), 2025. 134-141. https://doi.org/10.2478/kbo-2025-0089
11. Pîrvu, C., **Popescu, C**., Deleanu, L., Vasiliu, A.V. & Ojoc, G.G. (2025). Aspects of Ballistic Panels Made of Unidirectional Aramid Fabrics, Tested Against 9 mm FMJ Projectile. *International conference KNOWLEDGE-BASED ORGANIZATION*, *31*(3), 2025. 120-128. https://doi.org/10.2478/kbo-2025-0087

Scientific papers published in Romanian journals

12. Avasiloaiei C., Lăzăroaie C., **Popescu C.,** Cercetări experimentale pentru obținerea spumelor ceramice cu aplicații militare, Revista Tehnica Militară, numărul 1/2020, pp. 3-7. https://www.acttm.ro/rtm/2020/nr1_2020.pdf
13. **Popescu C.,** Alexe F., Bugean I., Evaluarea mediului de lucru în condiții de tragere cu armamentul de infanterie, armamentul de artilerie și activitățile de distrugere, Revista Tehnica Militară, numărul 1/2022, pp. 77-92. https://www.acttm.ro/wp-content/uploads/2023/03/TEHNICA-MILITARA-nr-1_2022_TIPAR.pdf

14. **Popescu C.,** Călinescu D., Sandu S., Bugean A., Noi materiale și structuri de protecție la efectele exploziilor, Revista Tehnica Militară, numărul 1/2023, pp. 13-27. https://www.acttm.ro/wp-content/uploads/2024/07/TEHNICA-MILITARA-nr-1_2023_TIPAR.pdf

Awards

15. Vasiliu, A. V., **Popescu, C**., Boțan, M., Pîrvu, C., Azamfirei, V., Badea, S. M., & Deleanu, L. (2025, November 21–23). *Could an Endumax Plate Replace Ceramics in Ballistic Protection?* **Gold Medal and Certificate of Excellence**, EURO POLITEHNICUS 2025 – International Innovation and Invention Show, 2nd edition, Bucharest, Romania. „Constantin Brâncuși" University of Târgu Jiu.
16. Ojoc, G. G., **Popescu, C**., Constandache, M., Azamfirei, V., Badea, S. M., & Deleanu, L. (2025, November 21–23). *Quadraxial Glass Fiber Composite for Ballistic Protection.* **Gold Medal and Special Award**, EURO POLITEHNICUS 2025 – International Innovation and Invention Show, 2nd edition, Bucharest, Romania. „Constantin Brâncuși" University of Târgu Jiu

REFERENCES

1. Abdulghaffar, H. (2015). Study on the arrangement of fabric materials for multi-layer soft body armor based on their mechanical properties. *Journal of Fashion Technology and Textile Engineering*, *3*(3), 1-5. https://doi.org/10.4172/2329-9568.1000126

2. Abtew, M. A., Boussu, F., & Bruniaux, P. (2021). Dynamic impact protective body armour: A comprehensive appraisal on panel engineering design and its prospective materials. *Defence Technology*, *17*(6), 2027-2049. https://doi.org/10.1016/j.dt.2021.03.016

3. Abtew, M. A., Boussu, F., Bruniaux, P., & Hong, Y. (2021). Dynamic impact surface damage analysis of 3D woven para-aramid armour panels using NDI technique. *Polymers*, *13*(6), 877. https://doi.org/10.3390/polym13060877

4. Abtew, M. A., Boussu, F., Bruniaux, P., Loghin, C., & Cristian, I. (2019). Ballistic impact mechanisms–a review on textiles and fibre-reinforced composites impact responses. *Composite structures*, *223*, 110966. https://doi.org/10.1016/j.compstruct.2019.110966

5. Abtew, M. A., Boussu, F., Bruniaux, P., Loghin, C., & Cristian, I. (2020). Effect of structural parameters on the deformational behaviors of multiply 3D layer-by-layer angle-interlock para-aramid fabric for fiber-reinforcement composite. *Journal of Composites Science*, *4*(4), 145. https://doi.org/10.3390/jcs4040145

6. Abtew, M. A., Loghin, C., Cristian, I., Boussu, F., Bruniaux, P., Chen, Y., & Wang, L. (2019). Mouldability and its recovery properties of 2D plain woven para-aramid fabric for soft body armour applications. *Fibres & Textiles in Eastern Europe*, *27*(6 (138)). https://doi.org/10.5604/01.3001.0013.4468

7. Ahmad, M. R., Ahmad, W. Y. W., Salleh, J., & Samsuri, A. (2008). Effect of fabric stitching on ballistic impact resistance of natural rubber coated fabric systems. *Materials & Design*, *29*(7), 1353-1358. https://doi.org/10.1016/J.MATDES.2007.06.007

8. Alexe, G. G., Carp, G. B., Tiganescu, T. V., & Buruiana, D. L. (2025). Enhancing the Performance of Materials in Ballistic Protection Using Coatings—A Review. *Technologies*, *14*(1), 13. https://doi.org/10.3390/technologies14010013

9. Alonso, L., Martínez-Hergueta, F., Garcia-Gonzalez, D., Navarro, C., García-Castillo, S. K., & Teixeira-Dias, F. (2020). A finite element approach to model high-velocity impact on thin woven GFRP plates. *International Journal of Impact Engineering*, *142*, 103593. https://doi.org/10.1016/j.ijimpeng.2020.103593

10. Bajya, M., Majumdar, A., Butola, B. S., Arora, S., & Bhattacharjee, D. (2021). Ballistic performance and failure modes of woven and unidirectional fabric based soft armour panels. *Composite Structures*, *255*, 112941. https://doi.org/10.1016/j.compstruct.2020.112941

11. Bao, Y., & Wierzbicki, T. (2004). On fracture locus in the equivalent strain and stress triaxiality space. *International journal of mechanical sciences*, *46*(1), 81-98. https://doi.org/10.1016/j.ijmecsci.2004.02.006

12. Bilisik, K., Karaduman, N. S., Bilisik, N. E., & Bilisik, H. E. (2013). Three-dimensional fully interlaced woven preforms for composites. *Textile Research Journal*, *83*(19), 2060-2084. https://doi.org/10.1177/00405175134877.

13. Bilisik, K., & Korkmaz, M. A. H. M. U. T. (2010). Multilayered and multidirectionally-stitched aramid woven fabric structures: experimental characterization of ballistic performance by considering the yarn pull-out test. *Textile research journal*, *80*(16), 1697-1720. https://doi.org/10.1177/004051751036595.

14. Bilisik Kadir, A., & Turhan, Y. (2009). Multidirectional stitched layered aramid woven fabric structures and their experimental characterization of ballistic performance. Textile Research Journal, 79(14), 1331-1343. https://doi.org/10.1177/0040517509104275

15. Bhatnagar, A. (Ed.). (2016). *Lightweight ballistic composites: military and law-enforcement applications*. Woodhead Publishing.

16. Bogajczyk, M., Cegla, M., Habaj, W., & Podgã, P. (2017). Selected Issues of Lightweight Bulletproof Vests Design and Testing. In *30th International Symposium on Ballistics*. DOI 10.12783/ballistics2017/16900.

17. Boussu, F., Cristian, I., & Nauman, S. (2015). General definition of 3D warp interlock fabric architecture. *Composites Part B: Engineering*, *81*, 171-188. https://doi.org/10.1016/j.compositesb.2015.07.013.

18. Brünig, M., Gerke, S., & Zistl, M. (2019). Experiments on damage and fracture mechanisms in ductile metals under non-proportional loading paths. In *Plasticity, Damage and Fracture in Advanced Materials* (pp. 19-33). Cham: Springer International Publishing. **DOI** 10.1088/1757-899X/651/1/012009

19. Ceoromila, A. C., Deleanu, L., Popescu, C., Lom, I., Vasiliu, A. V., Seiciu, P. L., ... & Sandu, S. M. (2025). SEM Investigation of Failure Mechanisms in Twaron® Aramid Fibers Used for Personal Armors. *Polymers*, *17*(8), 1058. https://doi.org/10.3390/polym17081058

20. Chang, C. P., Shih, C. H., You, J. L., Youh, M. J., Liu, Y. M., & Ger, M. D. (2021). Preparation and ballistic performance of a multi-layer armor system composed of kevlar/polyurea composites and shear thickening fluid (Stf)-filled paper honeycomb panels. *Polymers*, *13*(18), 3080. https://doi.org/10.3390/polym13183080

21. Chen, X. (Ed.). (2016). Advanced fibrous composite materials for ballistic protection. Woodhead Publishing. DOI: 10.1016/C2014-0-01733-9

22. Chen, X., Zhou, Y., & Wells, G. (2014). Numerical and experimental investigations into ballistic performance of hybrid fabric panels. *Composites Part B: Engineering*, *58*, 35-42. https://doi.org/10.1016/j.compositesb.2013.10.019

23. Chitrangad. (1993). Hybrid ballistic fabric (U.S. Patent No. 5,187,003). U.S. Patent and Trademark Office.

24. Chu, Y. (2015). *Surface modification to aramid and UHMWPE fabrics to increase interyarn friction for improved ballistic performance* (Master's thesis). University of Manchester, UK

25. Chu, Y., Chen, X., Sheel, D. W., & Hodgkinson, J. L. (2014). Surface modification of aramid fibers by atmospheric pressure plasma-enhanced vapor deposition. *Textile research journal*, *84*(12), 1288-1297. https://doi.org/10.1177/0040517513515311

26. Crouch, I. G. (2019). Body armour–New materials, new systems. *Defence Technology*, *15*(3), 241-253. https://doi.org/10.1016/j.dt.2019.02.002.

27. Cunniff, P. M. (1992). An analysis of the system effects in woven fabrics under ballistic impact. *Textile Research Journal*, *62*(9), 495-509, https://doi.org/10.1177/004051759206200902.

28. De Koning, C. A. M., & Van Dreumel, W. H. M. (1983). Mechanical Joining of Aramid Fibre Composites: An Experimental Study. *Journal of Reinforced Plastics and Composites*, *2*(2), 130-137. https://doi.org/10.1177/073168448300200206.

29. Dewangan, M. K., & Panigrahi, S. K. (2021). Factors influencing the ballistic impact mechanisms of textile composite materials: A review. *Polymers for Advanced Technologies*, *32*(5), 1901-1923. https://doi.org/10.1002/pat.5236

30. Dufour, C., Wang, P., Boussu, F., & Soulat, D. (2014). Experimental investigation about stamping behaviour of 3D warp interlock composite preforms. *Applied Composite Materials*, *21*(5), 725-738. DOI: 10.1007/s10443-013-9369-9

31. Elgohary, D. H. (2025). Technological aspects of body armour textiles for ballistic protection application. *The Journal of The Textile Institute*, *116*(4), 535-549. DOI: 10.1080/00405000.2024.2343162

32. Fejdyś, M., Kośla, K., Kucharska-Jastrząbek, A., & Łandwijt, M. (2021). Influence of ceramic properties on the ballistic performance of the hybrid ceramic–multi-layered UHMWPE composite armour. *Journal of the Australian Ceramic Society*, *57*(1), 149-161. https://doi.org/10. 1007/s41779-020-00516-7

33. Finckenor, M. M. (2017). *Comparison of high-performance fiber materials properties in simulated and actual space environments* (No. NASA/TM-2017-219634).

34. G Ganor, J. (2021). *Body Armor: And Light Ballistic Armor Materials and Systems*. Adept Press. ISBN-13: 9798985020205

35. Ghid ANSYS Explicit Dynamics Analysis (2024). ANSYS, Inc., USA

36. Grujicic, M., Pandurangan, B., Koudela, K. L., & Cheeseman, B. A. (2006). A computational analysis of the ballistic performance of light-weight hybrid composite armors. *Applied Surface Science*, *253*(2), 730-745. https://doi.org/10.1016/j.apsusc.2006.01.016

37. Grujicic, M., Snipes, J., Ramaswami, S., Avuthu, V., Yen, C. F., & Cheeseman, B. (2016). Unit-cell-based derivation of the material models for armor-grade composites with different architectures of ultra-high molecular-weight polyethylene fibers. *International Journal of Structural Integrity*, *7*(4), 458-489, doi: 10.1108/IJSI-06-2015-0015

38. Jantharat, P., McCuiston, R. C., Gamonpilas, C., & Kochawattana, S. (2014). Influence of the laminate configurations of transparent armor on its ballistic protection. *Key Engineering Materials*, *608*, 253-258. DOI: 10.4028/www.scientific.net/KEM.608.253

39. Jeyasri, J., Ajith, M., Darshan, N. C., ManiBharathi, K., & Sivasankar, C. (2019). *Design and fabrication of bulletproof vest*. *Journal of Emerging Technologies and Innovative Research, 6*(5), 87–90. ISSN-2349-5162

40. John, J., & Chen, X. (2012, September). 2D/3D woven fabrics for ballistic protection. In *4th world conference on 3D fabrics and their applications*.

41. Johnson, G. R., & Cook, W. H. (1985). Fracture characteristics of three metals subjected to various strains, strain rates, temperatures and pressures. *Engineering fracture mechanics*, *21*(1), 31-48.

42. Karahan, M., Kuş, A., & Eren, R. (2008). An investigation into ballistic performance and energy absorption capabilities of woven aramid fabrics. *International Journal of Impact Engineering*, *35*(6), 499-510. https://doi.org/10.1016/j.ijimpeng.2007.04.003

43. Kondor, I. P., Líska, J., & Kovács, Z. F. (2025). Ballistic performance of lightweight armor aramid fabric with different bounding technologies. *Fibers*, *13*(8), 106. https://doi.org/10.3390/fib13080106

44. Kukle, S., Valisevskis, A., Briedis, U., Balgale, I., & Bake, I. (2024). Hybrid Soft Ballistic Panel Packages with Integrated Graphene-Modified Para-Aramid Fabric Layers in Combinations with the Different Ballistic Kevlar Textiles. *Polymers*, *16*(15), 2106. https://doi.org/10.3390/polym16152106

45. Lee, Y. S., Wetzel, E. D., & Wagner, N. J. (2003). The ballistic impact characteristics of Kevlar® woven fabrics impregnated with a colloidal shear thickening fluid. *Journal of materials science*, *38*(13), 2825-2833. DOI: 10.1023/A:1024424200221

46. Lefebvre, M., Boussu, F., Coutellier, D., & Vallee, D. (2012). Influence of the vacuum resin process, on the ballistic behaviour of lightweight armouring solutions. In *EPJ Web of Conferences* (Vol. 26, p. 01051). EDP Sciences. DOI https://doi.org/10.1051/epjconf/20122601051

47. Leiva Palomera, D. F., Fernández Abreu, M. E., Valín Rivera, J. L., Valin Fernández, M., Ferreira de Amorim Júnior, W., Valenzuela Diaz, F. R., ... & Ketterer, C. I. G. (2025). Analysis of the Ballistic Effectiveness of the Hybrid Composite of Polyurethane and Kevlar 29 with Different Grammages. *Polymers*, *17*(3), 372. https://doi.org/10.3390/polym17030372

48. Liang, Y., Chen, X., & Soutis, C. (2022). Review on manufacture of military composite helmet. *Applied Composite Materials*, *29*(1), 305-323. https://doi.org/10.1007/s10443-021-09944-5

49. Lim, J. S., Lee, B. H., Lee, C. B., & Han, I. S. (2012). Effect of the weaving density of aramid fabrics on their resistance to ballistic impacts. 10.4236/eng.2012.412A119

50. Lim, J. S. (2013). Ballistic behavior of heracron®-based composites: Effect of the number multifilaments on high-speed projectiles. https://doi.org/10.4236/mnsms.2013.33011

51. Ma, D., Manes, A., Amico, S. C., & Giglio, M. (2019). Ballistic strain-rate-dependent material modelling of glass-fibre woven composite based on the prediction of a meso-heterogeneous approach. *Composite Structures*, *216*, 187-200. https://doi.org/10.1016/j.compstruct.2019.02.102

52. Martinez-Hergueta, F., Ridruejo, A., González, C., & LLorca, J. (2018). Ballistic performance of hybrid nonwoven/woven polyethylene fabric shields. *International Journal of Impact Engineering*, *111*, 55-65. https://doi.org/10.1016/j.ijimpeng.2017.08.011

53. Mawkhlieng, U., & Majumdar, A. (2019). Soft body armour. *Textile Progress*, *51*(2), 139-224. https://doi.org/10.1080/00405167.2019. 1692583

54. Medvedovski, E. (2010). Ballistic performance of armour ceramics: Influence of design and structure. Part 1. *Ceramics International*, *36*(7), 2103-2115. https://doi.org/10.1016/j.ceramint.2010.05.021

55. Min, S., Chu, Y., & Chen, X. (2016). Numerical study on mechanisms of angle-plied panels for ballistic protection. *Materials & Design*, *90*, 896-905. https://doi.org/10.1016/j.matdes.2015.11.019

56. Min, S., Chai, Y., Chu, Y., & Chen, X. (2019). Effect of panel construction on the ballistic performance of multiply 3D through-the-thickness angle-interlock fabric reinforced composites. *Polymers*, *11*(2), 198. https://doi.org/10.3390/polym11020198.

57. Mudzi, P., Wu, R., Firouzi, D., Ching, C. Y., Farncombe, T. H., & Selvaganapathy, P. R. (2022). Use of patterned thermoplastic hot film to create flexible ballistic composite laminates from UHMWPE fabric. *Materials & Design*, *214*, 110403.. 110403. https://doi.org/10.1016/j.matdes.2022.110403

58. Naveen, J., Jayakrishna, K., Hameed Sultan, M. T. B., & Amir, S. M. M. (2020). Ballistic performance of natural fiber based soft and hard body armour-a mini review. *Frontiers in Materials*, *7*, 608139. https://doi.org/10.3389/fmats.2020.608139

59. Nikky, A., & Rao, D. P. S. (2018). A review on materials & ballistic energy absorption of body armour. *IJRSI V*, 93-99. ISSN 2321-2705

60. Nurazzi, N. M., Asyraf, M. R. M., Khalina, A., Abdullah, N., Aisyah, H. A., Rafiqah, S. A., ... & Sapuan, S. M. (2021). A review on natural fiber reinforced polymer composite for bullet proof and ballistic applications. *Polymers*, *13*(4), 646. DOI: 10.3390/polym13040646

61. Öberg, E. K., Dean, J., & Clyne, T. W. (2015). Effect of inter-layer toughness in ballistic protection systems on absorption of projectile energy. *International Journal of Impact Engineering*, *76*, 75-82. https://doi.org/10.1016/j.ijimpeng.2014.09.006.

62. Ojoc, G. G., Rus, V. T., Popescu, C., Pirvu, C., & Deleanu, L. (2020). Influence of friction in a case of impact simulation. *INCAS Bulletin*, *12*(4), 145-154. 10.13111/2066-8201.2020.12.4.13

63. Ojoc, G. G. (2022). *Un studiu teoretic și experimental al pachetelor de protecție balistică pentru blindaje pe bază de fibre de sticlă* (Doctoral dissertation, Universitatea „Dunărea de Jos” din Galați).

64. Othman, A. R., & Hassan, M. H. (2013). Effect of different construction designs of aramid fabric on the ballistic performances. *Materials & Design*, *44*, 407-413. https://doi.org/10.1016/j.matdes.2012.07.061.

65. Park, J. L., Chi, Y. S., & Kang, T. J. (2013). Ballistic performance of hybrid panels composed of unidirectional/woven fabrics. *Textile Research Journal*, *83*(5), 471-486. https://doi.org/10.1177/0040517512444337.

66. Perry, A. (2018). Ballistic-resistant body armor: Problems and coping strategies. *Journal of Textile and Apparel, Technology and Management*, *10*(4).

67. Pinkos, J., & Stempien, Z. (2020). Numerical and experimental comparative analysis of ballistic performance of packages made of biaxial and triaxial Kevlar 29 fabrics. *Autex Research Journal*, *20*(2), 203-219. DOI 10.2478/aut-2020-0015

68. Pîrvu, C. (2015). *Contribuții la studiul experimental și numeric al pachetelor de protecție balistică cu fibre aramidice* (Doctoral dissertation, Universitatea" Dunărea de Jos" din Galați).

69. Pîrvu, C., Popescu, C., Deleanu, L., Vasiliu, A.V. & Ojoc, G.G. (2025). Aspects of Ballistic Panels Made of Unidirectional Aramid Fabrics, Tested Against 9 mm FMJ Projectile. *International conference KNOWLEDGE-BASED ORGANIZATION*, *31*(3), 2025. 120-128. https://doi.org/10.2478/kbo-2025-0087

70. Pol, M. H., Liaghat, G. H., & Hajiarazi, F. (2013). Effect of nanoclay on ballistic behavior of woven fabric composites: Experimental investigation. *Journal of Composite Materials*, *47*(13), 1563-1573. https://doi.org/10.1177/0021998312449768.

71. Popescu, C., Sandu, S., Deleanu, L., Șeiciu, L. & Călinescu, D. (2024). Experimental Study of Twaron T730 for Two Threats. *International conference KNOWLEDGE-BASED ORGANIZATION*, *30*(3), 2024. 121-128. https://doi.org/10.2478/kbo-2024-0093

72. Popescu, C., Vasiliu, A.V., Călinescu, D., Cristea, G.C., Sandu, S.M. & Deleanu, L. (2025). Aspects of Ballistic Panels Made of Endumax XF33, Tested Against Different Projectiles. *International conference KNOWLEDGE-BASED ORGANIZATION*, *31*(3), 2025. 134-141. https://doi.org/10.2478/kbo-2025-0089

73. Porwal, P., & Phoenix, S. (2008). Effects of layer stacking order on the V 50 velocity of a two-layered hybrid armor system. *Journal of Mechanics of Materials and Structures*, *3*(4), 627-639. https://doi.org/10.2140/jomms.2008.3.627.

74. Regassa, Y., Likeleh, G., & Uppala, R. (2014). Modeling and simulation of bullet resistant composite body armor. *International Journal of Research Studies in Science, Engineering and Technology*, *1*(3), 39.

75. Resapu, R. R., & Perumahanthi, L. R. (2021). Numerical study of bilinear isotropic & kinematic elastic–plastic response under cyclic loading. *Materials Today: Proceedings*, *39*, 1647-1654. https://doi.org/10.1016/j.matpr.2020.05.812

76. Ribeiro, M. P., da Silveira, P. H. P. M., de Oliveira Braga, F., & Monteiro, S. N. (2022). Fabric impregnation with shear thickening fluid for ballistic armor polymer composites: an updated overview. *Polymers*, *14*(20), 4357. https://doi.org/10.3390/polym14204357

77. Richard, C., Bresson, B., Bès, M., Schittecatte, L., Le Roux, S., Didane, N., ... & Marcellan, A. (2023). Mechanisms of damage and fracture of aramid fibers: Focus on the role of microfibril cooperativity in fracture toughness. *Journal of Polymer Science*, *61*(20), 2549-2558. DOI: 10.1002/pol.20230400

78. Rotariu, A. N. (2017). *Balistică terminală: formarea şi accelerarea impactorilor*. Editura Academiei Tehnice Militare.

79. Sava, M., Hadăr, A., Părăuşanu, I., Petrescu, H. A., Baciu, F., & Marinel, S. M. (2016, June). Validation of the numerical model of single-layer composites reinforced with carbon fiber and aramid. In *AIP Conference Proceedings* (Vol. 1738, No. 1). AIP Publishing. https://doi.org/10.1063/1.4952316

80. Schwer, L. E. (2007). An overview of the LS-DYNA material models. *Proceedings of the 7th European LS-DYNA Conference*, Salzburg, Austria.

81. Shanazari, H., Liaghat, G. H., Hadavinia, H., & Aboutorabi, A. (2017). Analytical investigation of high-velocity impact on hybrid unidirectional/woven composite panels. *Journal of Thermoplastic Composite Materials*, *30*(4), 545-563. https://doi.org/10.1177/ 0892705715604680 .

82. Shbool, M., Al-Abdallat, Y., Abdul Jawwad, A. K., Alsharairi, S., Abu Ghannam, L., Abu-Khajil, E. E., & Badwan, A. (2021). Examining the effect of nano-additions of rare earth elements on the hardness of body armor ceramic. *Indian Journal of Engineering and Materials Sciences (IJEMS)*, *28*(1), 64-72. DOI: 10.56042/ijems.v28i1.28158

83. Shih, C. H., You, J. L., Lee, Y. L., Cheng, A. Y., Chang, C. P., Liu, Y. M., & Ger, M. D. (2022). Design and ballistic performance of hybrid plates manufactured from aramid composites for developing multilayered armor systems. *Polymers*, *14*(22), 5026. https://doi.org/10.3390/polym14225026

84. Shimek, M., & Fahrenthold, E. (2012). Effects of weave type on ballistic performance for aramid, UHMWPE, and hybrid fabrics. In *53rd AIAA/ASME/ASCE/AHS/ASC Structures, Structural Dynamics and Materials Conference 20th AIAA/ASME/AHS Adaptive Structures Conference 14th AIAA* (p. 1508). https://doi. org/10.2514/6.2012-1508

85. Simons, J. W., Erlich, D. C., & Shockey, D. A. (2001). Finite element design model for ballistic response of woven fabrics. *SRI International*, *9*.

86. Sun, D., Chen, X., & Wells, G. (2014). Engineering and analysis of gripping fabrics for improved ballistic performance. *Journal of Composite Materials*, *48*(11), 1355-1364. https://doi.org/10.1177/002199831348599

87. Tam, D. K. Y., Ruan, S., Gao, P., & Yu, T. (2012). High-performance ballistic protection using polymer nanocomposites. In *Advances in military textiles and personal equipment* (pp. 213-237). Woodhead Publishing. DOI: 10.1016/B978-1-84569-699-3.50010-4

88. Vasiliu, A. V., Popescu, C., Boțan, M., Pîrvu, C., Azamfirei, V., Badea, S. M., & Deleanu, L. (2025). *Endumax plate could replace ceramics in ballistic protection* [Conference presentation]. EURO Politehnicus.

89. Wang, H., Hazell, P. J., Shankar, K., Morozov, E. V., Escobedo, J. P., & Wang, C. (2017). Effects of fabric folding and thickness on the impact behaviour of multi-ply UHMWPE woven fabrics. *Journal of materials science*, *52*(24), 13977-13991.

90. Wanger, L. (2006). Military and law enforcement applications. *Lightweight ballistic composites. Abington Hall, Abington, Cambridge CB1 6AH, England: Woodhead Publishing*, 1e25.

91. Xue, L. (2007). Damage accumulation and fracture initiation in uncracked ductile solids subject to triaxial loading. *International journal of solids and structures*, *44*(16), 5163-5181.

92. Yang, H. H. (1993). *Kevlar aramid fiber*. John Wiley & Sons.

93. Yang, Y., & Chen, X. (2018). Determination of materials for hybrid design of 3D soft body armour panels. *Applied Composite Materials*, *25*(4), 861-875. https://doi.org/ 10.1007/s10443-018-9716-y

94. Yang, Y., & Chen, X. (2017). Investigation of failure modes and influence on ballistic performance of Ultra-High Molecular Weight Polyethylene (UHMWPE) uni-directional laminate for hybrid design. *Composite Structures*, *174*, 233-243. https://doi.org/10.1016/j.compstruct.2017.04.033.

95. Yang, Y., Ling, T., Liu, Y., & Xue, S. (2021). Synergistic effect of hybrid ballistic soft armour panels. *Composite Structures*, *272*, 114211. https://doi.org/10.1016/j. compstruct.2021.114211

96. Yilmazcoban, I., & Doner, S. (2016). Ballistic protection evaluation of sequencing the composite material sandwich panels for the reliable combination of armor layers. *Acta Physica Polonica A*, *130*(1), 342-346. https://doi.org/10.12693/APhysPolA.130.342

97. Zeng, H., Yuan, Z., Qiu, J., & Chen, X. (2018). Finite element study on the influence of structural parameters on the ballistic performance of 3D networked fabrics. *Applied Composite Materials*, *25*(4), 891-903. https://doi.org/10.1007/s10443-018-9721-1

98. Zhu, L., Gao, W., Dikin, D. A., Percec, S., & Ren, F. (2023). Anti-ballistic performance of PPTA/UHMWPE laminates. *Polymers*, *15*(10), 2281. https://doi.org/10.3390/polym15102281

Brochures

99. Twaron- a versatile high-performance fiber, Twaron Product Brochure - https://pdf.directindustry.com/pdf/teijin-aramid/twaron-product-brochure/18087-309129.html

100. A true all-around para-aramid performe – Twaron, Aramid by Teijin Brochure

101. ***ANSYS, Inc. LS-DYNA User's Guide – Failure: Plastic Strain Failure. Documentație tehnică ANSYS Help (2025).

102. FEI Quanta 200 Scanning Electron Microscope Technical Brochure, https://www.dental.umaryland.edu/media/sod/core-imaging facility/information_about_FEI_Quanta_SEM.pdf (accessed 4.12.2024).

103. Dyneema Composites Brochure

104. Honeywell Spectra® Fiber Brochure

Documents/Reports/Standards

105. NATO 2022 Strategic Concept Adopted by Heads of State and Gouvernment at the NATO Summit in Madrid, 2022.

106. A Strategic Compass for Security and Defence, 2022.

107. National Defense Strategy for the Period 2025-2030, Presidential Administration, Romania.

108. Technical Guide Kevlar Aramid Fibers

109. Tech Data Sheet - Kevlar® EXO™ CoreMatrix™ CM E1100H

110. Development Product Specification Kevlar® EXO™ CoreMatrix™ CM E1100H

111. Dupont CoreMatrix Tehnology Brochure

112. Dupont Kevlar XD S002 Technical Data Sheet

113. DSM Dyneema SB21

114. Teijin – Ballistic materials handbook. Aramids by Teijin

115. Cordura Classic Fabric Technical Data Sheet

116. NIJ Standard – 0101.06, Ballistic Resistance of Body Armor, 2008

117. NIJ Standard – 0101.07, Ballistic Resistance of Body Armor, 2023

118. Technical data sheet B472 Precision Light Screen (Proposed Training Schedule for B251 System The proposed training schedule is as follows)

119. Technical data sheet SA-Z FASTCAM series by Photron

120. Technology readiness level definitions and descriptions (TRL Explanations_1.pdf)

121. European Patent Office. (2023). EP 3974174 B1: Ballistic material made from woven ballistic fabric layer(s) and hydro-entangled non-woven fibers

Websites

122. www.stimpex.ro, accesat la 17.06.2025